Photoelectron Spectra with Quantum Trajectories beyond the plain Strong-Field Approximation

Dissertation
zur
Erlangung des akademischen Grades
doctor rerum naturalium (Dr. rer. nat.)
der Mathematisch-Naturwissenschaftlichen Fakultät
der Universität Rostock

vorgelegt von
Keil, Thomas
geb. am 27.01.1988 in Rostock

Rostock, 24. Januar 2018

urn:nbn:de:gbv:28-diss2018-0022-8

Betreuer:
Prof. Dr. Dieter Bauer (Universität Rostock, Institut für Physik)

Gutachter:
Prof. Dr. Dieter Bauer (Universität Rostock, Institut für Physik)
Prof. Dr. Olga Smirnova (Max-Born-Institut, Berlin)

eingereicht am
20. September 2017

verteidigt am
21. Dezember 2017

Für meine Frau Christine,
die meine dauernde Abwesenheit mit Fassung getragen hat,
und meine Töchter Rahel und Sophia,
die ihren Papa immer wieder mit einem Lächeln aufmuntern.

Abstract

English

The calculation of photoelectron spectra (PES) in the field of strong laser-matter interaction is a great challenge for theoretical physics. For several decades now the strong field approximation (SFA) has proven to be quite successful in that respect. Additionally, thanks to its formulation in terms of quantum trajectories, it provides deep insight into the dynamics of the ionization process. However, in the plain SFA the influence of the Coulomb potential on the emitted electron is neglected. With more and more sophisticated experimental techniques this approximation leads to more and more features being missed by the SFA even on a qualitative level.

In this work we investigate different extensions of that theory to analyze spectral features beyond the scope of the plain SFA. We consider different systems where additional forces influence the emitted electron. The collective field of a laser-driven metal cluster is observed to cause strong acceleration of emitted electrons near resonance. The Coulomb potential of the parent ion can for certain parameters lead to unexpectedly high yield around the cutoff energy for direct ionization. And finally the magnetic Lorentz force which appears when dropping the dipole approximation can cause asymmetries with respect to the laser propagation direction even for non-relativistic laser parameters.

Appropriate methods are derived for each of these systems and used to calculate PES. The results are compared on a qualitative level to the time-dependent Schrödinger equation (TDSE) or reference results from the literature and analyzed in terms of quantum trajectories which allow us to understand the underlying physical mechanisms leading to the effects under consideration.

Deutsch

Die Berechnung von Photoelektronenspektren (PES) im Bereich der starken Laser-Materie-Wechselwirkung ist eine große Herausforderung für die theoretische Physik. Bereits seit einigen Jahrzehnten ist die Starkfeldnäherung (SFA) in dieser Hinsicht sehr erfolgreich. Zudem vermittelt diese dank der Formulierung mittels Quantentrajektorien tiefe Einblicke in die Dynamik des Ionisationsprozesses. Allerdings wird in der reinen SFA der Einfluss des Coulomb-Potentials auf das emittierte Elektron vernachlässigt. Im Rahmen der fortschreitenden Entwicklung experimenteller Techniken führt diese Näherung dazu, dass immer mehr Phänomene entdeckt werden, die sich selbst auf qualitativer Ebene einer Beschreibung durch die SFA entziehen.

In dieser Arbeit untersuchen wir verschiedene Erweiterungen dieser Theorie, um Merkmale von Spektren zu analysieren, deren Nachbildung jenseits der Möglichkeiten der reinen SFA liegt. Wir befassen uns mit verschiedenen Systemen, in denen zusätzliche Kräfte die emittierten Elektronen beeinflussen. Zuerst das kollektive Feld eines lasergetriebenen Metallclusters, welches bei resonanter Anregung zu unerwartet starker Beschleunigung der emittierten Elektronen führen kann. Dann das Coulomb-Potential des zurückbleibenden Ions, aufgrund dessen bei bestimmten Parametern die Elektronenausbeute im Bereich der cutoff-Energie für die direkte Ionisation weit höher ausfällt als erwartet. Zuletzt die magnetische Lorentzkraft, die erst dann überhaupt in Erscheinung tritt, wenn die Dipolnäherung aufgegeben wird. Diese kann selbst bei nichtrelativistischen Parametern in den PES zu Asymmetrieeffekten in Bezug auf die Propagationsrichtung des Laserpulses führen.

Für die verschiedenen Systeme werden passende Methoden von der trajektorienbasierten SFA abgeleitet und verwendet, um PES zu berechnen. Die Resultate werden auf qualitativer Ebene mit der Lösung der zeitabhängigen Schrödingergleichung (TDSE) oder Referenzresultaten aus der Literatur verglichen. Die Analyse der Probleme mit Hilfe von Quantentrajektorien ermöglicht uns, die den betrachteten Effekten zugrundeliegenden physikalischen Mechanismen besser zu verstehen.

Vorwort

Im folgenden präsentiere ich das Resultat meiner wissenschaftlichen Arbeit während der letzten fast sechs Jahre. An dieser Stelle möchte ich einen kurzen Abriss über die Entstehungsgeschichte dieser Arbeit liefern und mich anschließend bei denen bedanken, die mir in dieser Zeit beigestanden haben.

Begonnen hat das ganze im September 2010 mit der Entscheidung, meine Diplomarbeit in der Arbeitsgruppe 'Quantentheorie & Vielteilchensysteme' von Professor Bauer anzufertigen. Nach dem erfolgreichen Abschluss derselben (erstaunlicherweise innerhalb der Regelstudienzeit, was vor allem dadurch motiviert worden war, dass wir bei der Übergabe der Vordiplom-Zeugnisse von dem damaligen Dekan Professor Schick darum gebeten worden waren, 'für die Statistik' rechtzeitig fertig zu werden) bot sich mir die Möglichkeit einer Stelle als wissenschaftlicher Mitarbeiter in ebenjener Arbeitsgruppe zum Zwecke der Promotion. Da ich von der Arbeit sehr angetan war, schon lange mit dem Gedanken an eine Doktorarbeit gespielt und darüber hinaus keine attraktive Alternative hatte, nahm ich die Stelle an.

Ab Mitte November 2011 war ich dann also offiziell Wissenschaftler. Zuerst versuchte ich, das Thema meiner Diplomarbeit (Freeman-Resonanzen) aufzugreifen und etwas daraus zu destillieren, was man veröffentlichen könnte. Leider ohne Erfolg, also ging ich im Sommer 2012 dazu über, mich mit der Simulation von Natrium-Clustern zu befassen, unter Verwendung von zeitabhängiger Dichtefunktionaltheorie (DFT). Im Rahmen dessen durfte ich auch eine Masterarbeit betreuen. Die Einladung an Professor Bauer, einen Artikel für eine Special Issue des 'Journal of Physics B: Atomic, Molecular and Optical Physics' zu schreiben, führte mich dann letztendlich zum Thema meiner Arbeit, den Quantentrajektorien. Die Erkenntnisse, die ich bis dahin mittels der DFT gesammelt hatte, gingen ein in die Legitimation eines verwendeten Modell-Potentials (das Rigid-Sphere Model), wurden darüber hinaus aber weitestgehend zu den Akten gelegt. Die Simulationen habe ich mit einem bereits vorhanden Trajektoriencode (von Professor Bauer) durchgeführt, den ich auf das Problem angeregter Metall-Cluster anpassen konnte.

Nachdem der Artikel fertig und eingereicht war, konnte ich mich ab Anfang 2014 eingehender mit der Trajektorienmethode befassen, um zu sehen, welches Potential diese hat. Da mein Kollege Volker sich mit der Simulation von Molekülen (auf Basis der zeitabhängigen Schrödingergleichung (TDSE)) befasste, lag es nahe, mich dem gleichen Thema mittels der Quantentrajektorien zu nähern. Die Resultate waren jedoch nicht interessant genug, um auch veröffentlicht zu werden. Allerdings fiel schon dabei auf, dass gewisse Merkmale der TDSE-Resultate in den Trajektorienrechnungen viel schwächer ausgeprägt waren. Um das genauer zu untersuchen, habe ich mich dann auf den einfachsten Fall konzentriert, nämlich das einzelne Wasserstoffatom.

Da der verwendete Code durch das viele ausprobieren, modifizieren und erweitern mittlerweile zu einem unübersichtlichen Monstrum angewachsen war, habe ich ihn Ende 2014 kurzerhand komplett neu geschrieben. Zuerst in Python wegen der angenehmen Lesbarkeit, aber da diese Version etwa um einen Faktor 20 langsamer war als mein vorheriger Code, habe ich alles nochmal in C++ implementiert, wie zuvor.

Nach intensiver theoretischer Vorarbeit in Kooperation mit Sergey Popruzhenko und Professor Bauer hatte ich dann endlich eine Grundlage, mit deren Hilfe ich das scheinbar seltsame Verhalten meiner Trajektorien erklären konnte. Zu diesem Zweck musste ich allerdings auch noch einen eigenen Runge-Kutta-Solver implementieren, da weder der Vorhandene noch die Varianten aus der GSL entlang beliebiger Pfade in der komplexen Ebene integrieren konnten. Weitere theoretische Untersuchungen, ein Haufen Literaturrecherche, viele Beispielrechnungen mit der TDSE und einiges Herumprobieren mit den Trajektorien führten dann letztendlich zu einem weiteren Artikel, der dann im Dezember 2016 veröffentlicht wurde. Nicht zuletzt verantwortlich dafür, dass das ganze so lange gedauert hat, waren die Geburt meiner Tochter Rahel im September 2014 und die Tatsache, dass die Familie auf der Liste meiner Prioritäten sehr weit oben steht.

Als letztes Projekt habe ich mich dann mit der Dipolnäherung beschäftigt und damit, wie sich das weglassen derselben auf die Spektren auswirkt. Dazu musste ich zuerst ein wenig meine Kenntnisse bezüglich der speziellen Relativitätstheorie auffrischen, da der magnetische Anteil der Lorentzkraft proportional zu $\frac{v}{c}$ ist und damit relativistische Effekte nicht von vornherein vernachlässigt werden sollten. Als Referenz für meine Untersuchungen dienten die Resultate aus einem 2014 veröffentlichten Artikel, die ich mittels meiner Quantentrajektorien reproduzieren und anhand eines einfachen Modells erklären konnte. Der daraus hervorgegangene Artikel wurde bereits eingereicht und zur Veröffentlichung akzeptiert (Stand: 14. September 2017).

Danksagungen Niedergeschrieben habe ich diese Arbeit dann im Zeitraum von März bis August 2017. Da dies das Resultat der oben beschriebenen letzten sechs Jahre ist, möchte ich an dieser Stelle denen danken, die mich in dieser Zeit begleitet und unterstützt haben.

Allen voran danke ich meinem Chef und Betreuer Dieter Bauer, für die zahllosen beantworteten Fragen, die vielen hilfreichen Ideen und Vorschläge, und immer wieder die Toleranz gegenüber meinen so völlig anderen Prioritäten. Einen besseren Betreuer hätte ich mir nicht vorstellen können. Außerdem möchte ich meinem Kollegen und langjährigen Schreibtischnachbarn Volker Mosert dafür danken, dass er mich zum einen so lange geduldig ertragen hat, und mir zum anderen als unser Gruppenadministrator schon nach wenigen Monaten Admin-Rechte in unserem Netzwerk eingeräumt hat. Dadurch hatte ich die Gelegenheit und auch die Motivation, neben der Physik sehr viel praktisches über Linux und Linux-Netzwerke zu lernen.

In diesem Zusammenhang möchte ich auch all den anderen Kollegen (derzeitigen und ehemaligen) danken, für viele anregende Gespräche, über physikalische und auch nicht-physikalische Themen aller Art. Besonders hervorheben möchte ich dabei

Tanja, mit der ich mir gern auch noch länger ein Büro geteilt hätte, und Adrian, meinen Lehrling und Nachfolger als Administrator der Arbeitsgruppe. Darüber hinaus geht mein Dank an Yaroslav, Julius, Martins und meine gesamte Arbeitsgruppe, für viele fachliche Diskussionen im Rahmen unserer group meetings und auch darüber hinaus; Sonja, Niels, Clemens, Andreas, Mandy und die ganze AG Redmer, für viele gemeinsam verbrachte Mittagspausen und viel dabei gegessenes Eis; und nicht zuletzt Frau Hertzfeldt, unsere Sekretärin, für viel Hilfe bei sämtlichen anstehenden Formalitäten.

Desweiteren möchte ich hier Sergey Popruzhenko nennen, der mir eine große Hilfe war beim Verstehen der SFA im Allgemeinen und der Herleitung der Coulomb-Korrektur im Besonderen, und Emilio Pisanty, aufgrund dessen Arbeit ich die Konsequenzen ebenjener Coulomb-Korrektur überhaupt erst einschätzen konnte.

Nicht zuletzt, und ganz besonders, möchte ich meiner Familie danken. Vor allem meiner Frau Christine und meinen Töchtern Rahel und Sophia, für viel Geduld und Unterstützung in den letzten Jahren, und meinen Eltern und Schwiegereltern, die immer zur Stelle waren, wenn wir es alleine nicht geschafft hätten.

Und zum Schluss möchte ich außer der Reihe all jenen Menschen danken, die sich im Bereich der freien Software engagieren. Für die Entstehung dieser Arbeit relevant waren dabei beispielsweise die folgenden Projekte: Debian, Ubuntu, Emacs, LaTeX und gnuplot, um nur einige zu nennen.

Contents

List of Abbreviations

ARM analytical R-matrix

CCSFA Coulomb-corrected strong field approximation

CTMC classical trajectory Monte Carlo

DFT density functional theory

EOM equation of motion

LES low-energy structures

PES photoelectron spectra

RSM rigid-sphere model

SAE single active electron

SFA strong field approximation

SMT simple man's theory

SPA saddle-point approximation

SPARC surface-plasmon assisted rescattering in clusters

SPE saddle-point equation

TCSFA trajectory-based Coulomb-corrected strong field approximation

TD-DFT time-dependent density functional theory

TDSE time-dependent Schrödinger equation

List of Publications & Talks

List of publications:

- T. Keil and D. Bauer, "Collective-field-corrected strong field approximation for laser-irradiated metal clusters", J. Phys. B: At., Mol. Opt. Phys. **47**, 124029 (2014) 10.1088/0953-4075/47/12/124029
- T. Keil, S. V. Popruzhenko, and D. Bauer, "Laser-driven recollisions under the Coulomb barrier", Phys. Rev. Lett. **117**, 243003 (2016) 10.1103/PhysRevLett.117.243003
- T. Keil and D. Bauer, "Coulomb-corrected strong-field quantum trajectories beyond dipole approximation", J. Phys. B: At., Mol. Opt. Phys. (2017) 10.1088/1361-6455/aa8ab1

List of public talks:

- December 6, 2012, *Dynamics of Sodium Clusters in Strong Laser Fields - DFT-Simulations within the Jellium Model*, Universität Rostock, Institut für Physik, Graduiertenkolleg
- November 19, 2013, *Intense laser-cluster interaction simulations with TDDFT and strong-field quantum trajectories*, Universität Rostock, Institut für Physik, Theorieseminar
- March 18, 2014, *Quantum trajectory analysis of clusters and molecules in strong laser fields*, DPG Frühjahrstagung Berlin
- May 22, 2014, *Quantum trajectory analysis of systems in strong laser fields*, Universität Rostock, Institut für Physik, Graduiertenkolleg
- March 23, 2015, *Strong-field ionization with semi-classical trajectories - the role of the initial conditions*, DPG Frühjahrstagung Heidelberg
- June 6, 2017, *Photoelectron Spectra with Quantum Trajectories beyond the Strong-Field Approximation*, Universität Rostock, Institut für Physik, Graduiertenkolleg

1. Introduction

The topic of strong-field physics has attracted quite some attention in recent years, which can be attributed both to the development of faster computers, which leads to more and more precise numerical predictions of what happens at high intensities, and to the development of more and more sophisticated experimental techniques, which allows to test these predictions. In turn, this leads to more and more new strong-field phenomena being found, examples being the low [1–3], very-low [4, 5] and zero [6, 7] energy structures where surprisingly high yield was observed for particular electron momenta, or measurable non-dipole effects [8, 9] at rather non-relativistic intensities. All these effects call for the theorists to reproduce and, as far as possible, explain them to expand our understanding of the underlying physics.

One of the most promising theories in this respect is the strong field approximation (SFA). It dates back to the 1960s when Reiss applied the Volkov solution of the Dirac equation for the description of free electrons in a field [10]. Using the same approach a method to describe strong-field ionization was developed by Keldysh [11], Faisal [12] and Reiss [13], hence being sometimes also called KFR theory. It is based on the idea that the ionization process can be split into two parts separated by a singular ionization event, where the first part describes a bound electron unaffected by the laser field, and the second part describes a free electron in a laser field neglecting the binding potential. While this is accurate for potentials with very small range (e.g., in the case of ionization of singly charged negative ions), it turns out to be a good approximation in case of the long-range Coulomb potential as well. Furthermore, the plain SFA is not limited to direct ionization but can by construction be extended in a straightforward way towards hard rescattering [13–15]. This is quite fortunate in so far as conventional perturbation theory is not applicable anymore once non-linear (multiphoton) processes become important at higher intensities. However, in recent years several phenomena have been found (e.g. the ones mentioned in the first paragraph) that are beyond the scope of the plain SFA. Accordingly there are many different approaches to extend the SFA to overcome its shortcomings, some of which will be discussed in this work.

The literature provides us with several reviews, e.g. on the topics of tunneling and multiphoton ionization [16], above-threshold ionization [17] and the Keldysh theory in general [18], all of which elaborate on the further development of the SFA in the last years. Therefore we will only highlight some aspects being of particular importance for this work. The most prominent part is the application of the saddle-point approximation (or the method of steepest descent) to the transition amplitude which is the basic quantity resulting from the SFA. This method allows to view the transition amplitude as a coherent sum over contributions of individual quantum

trajectories, which in turn can be treated in analogy to classical electron trajectories. The major difference to classical trajectories, apart from the acquired complex phase allowing for interference effects, is that the initial (ionization) times are complex. However, for calculating the plain SFA transition amplitude this does not pose a problem. The great advantage of the trajectory picture is the possibility to take it seriously, and modify the laser-driven free electron propagation to include additional influences like external potentials, where the Coulomb potential is the most obvious example. Probably the very first application of this approach was the calculation of ionization rates, i.e., the PPT rate named after Perelomov, Popov and Terent'ev (henceforth referred to as PPT) [19, 20] and especially its Coulomb-corrected variant [21], demonstrating the potential that lies within the SFA and its extensions. Another much more recent take on the topic is the trajectory-based Coulomb-corrected strong field approximation (TCSFA) [22–25], which is discussed in detail in [26]. The latter was successfully used for example to reproduce the recently discovered low-energy structures [24], and to analyze them in terms of trajectories. The TCSFA differs from the PPT approach to a Coulomb-corrected strong field approximation (CCSFA) mainly in the initial conditions used for the trajectory propagation. It turns out that both variants have their advantages and disadvantages, hence they are both discussed in more detail in the following chapters.

Another method that must be mentioned in this context is the analytical R-matrix (ARM) theory [27–29] which is also outlined in [18], section 6.3, and compared to the CCSFA. The ARM theory and its applications are discussed in great detail in [30]. It is based on the idea that space can be partitioned into an inner and an outer region, in analogy to the partitioning in time done in the SFA. While the inner part describes the bound motion of the electron, for the outer part the eikonal Volkov approximation [31] is used to incorporate the influence of the Coulomb potential on the laser-driven electron motion. The results are similar to those from the CCSFA, but not identical. It is readily extended towards rescattering, whereas the CCSFA is limited to direct ionization (but the plain SFA is not, as mentioned above). This limitation is overcome by the TCSFA where rescattering is included in the numerical propagation of the electron trajectories. Additionally the ARM theory can by construction be applied to many-electron systems in a straightforward way [28]. However, here we restrict ourselves to problems that can be described in single active electron (SAE) approximation, and thus consider only methods derived from the trajectory-based SFA.

This work consists of four parts. Chapter 2 contains some theoretical basics which build the foundation of the methods used here. Chapter 3 demonstrates the application of a method derived from the TCSFA to collective fields in laser-driven metal clusters where we analyze the emission of high energy electrons. In chapter 4 the unexpectedly high yield around the cutoff momentum for direct ionization in photoelectron spectra (PES) obtained experimentally and from the time-dependent Schrödinger equation (TDSE) is investigated using a method based on the same ideas as the PPT approach. We first show how the behavior of the TDSE PES can be described using two dimensionless parameters by scaling appropriately. Then the

observed effect is qualitatively reproduced and analyzed in detail using the CCSFA. The last part (chapter 5) addresses non-dipole effects observed in experimental PES for non-relativistic laser parameters. Using the TCSFA extended towards non-dipole effects we reproduce asymmetric momentum shifts in and against the laser propagation direction which are obvious signs of non-dipole effects. To explain these we construct a simplified semi-analytical model where Coulomb and magnetic Lorentz force are included perturbatively, showing that these can indeed be disentangled.

It is followed by some concluding remarks and the appendices where some lengthy but instructive derivations as well as technical details are presented.

2. Theoretical Basics

2.1. Atomic Units

In most parts of this thesis Hartree atomic units are used unless noted otherwise. This greatly simplifies calculations as $\hbar$, m_e, e and $4\pi\varepsilon_0$ are set to unity. Additionally numbers in atomic units usually give a feeling whether the specified quantity can be considered large or small on the atomic scale. For instance, the length of 1 a.u. equals the Bohr radius, i.e., the radius of a hydrogen atom in the ground state, and the energy of 0.5 a.u. is the respective ground state energy. This has the pleasant side effect that most numbers can be written without having to use decimal powers or prefixes like *kilo* or *nano*.

A broad, formal introduction to atomic units can be found in [32], section 7.1.

2.2. Strong Field Approximation

The strong field approximation (SFA) is a method to approximate the transition matrix element of a single electron from a bound state into a continuum state under the influence of a strong electromagnetic field. It is *the* theoretical workhorse for strong-field ionization of atoms where conventional perturbation theory is not applicable. To simplify things where neither the laser field nor the binding potential can be neglected at all times, the emission process is split into two parts. In the first part the binding potential governs the electron motion and the laser field is neglected, until after an ionization event the laser field takes over and the binding potential is neglected.

The following derivation closely follows [32], section 7.3.4, but is presented here nevertheless as it is considered essential for the understanding of this thesis.

The initial state is an eigenstate $|\Psi_0\rangle$ of the field-free Hamiltonian $\hat{H}_0$ with binding energy $\mathcal{E}_0 < 0$. The transition from $|\Psi_0\rangle$ (assuming the laser is not yet switched on at the initial time t_i) to the final state $|\Psi_{\boldsymbol{p}}\rangle$ (which is a continuum state with asymptotic momentum $\boldsymbol{p}$) is described by the matrix element

$$M_{\boldsymbol{p}}(t) = \langle \Psi_{\boldsymbol{p}} | \hat{U}(t, t_i) | \Psi_0 \rangle \tag{2.1}$$

where $\hat{U}(t, t_i)$ is the time-evolution operator corresponding to the full time-dependent Hamiltonian

$$\hat{H}(t) = \frac{\hat{\boldsymbol{p}}^2}{2} + \hat{V}(\boldsymbol{r}) + \hat{W}(t)\,. \tag{2.2}$$

Here $\hat{V}(\boldsymbol{r})$ represents the binding potential and $\hat{W}(t)$ is the coupling to the laser

field. The Hamiltonian can be split in two different ways,

$$\hat{H}(t) = \hat{H}_0 + \hat{W}(t) = \hat{H}^{(\mathrm{V})}(t) + \hat{V}(\boldsymbol{r}) \tag{2.3}$$

with

$$\hat{H}_0 = \frac{\hat{\boldsymbol{p}}^2}{2} + \hat{V}(\boldsymbol{r}) \tag{2.4}$$

$$\hat{H}^{(\mathrm{V})}(t) = \frac{\hat{\boldsymbol{p}}^2}{2} + \hat{W}(t)\,. \tag{2.5}$$

$\hat{H}_0$ is the Hamiltonian describing the unperturbed atom and $\hat{H}^{(\mathrm{V})}(t)$ is the so-called Gordon-Volkov-Hamiltonian [33, 34] which describes the free motion of an electron in a laser field. These can be used to rewrite the time-evolution operator $\hat{U}(t, t_i)$. The latter obeys the Schrödinger equation

$$\mathrm{i}\frac{\mathrm{d}}{\mathrm{d}t}\hat{U}(t, t') = \hat{H}(t)\hat{U}(t, t') = [\hat{H}_0 + \hat{W}(t)]\hat{U}(t, t') \tag{2.6}$$

and thus the differential equations

$$\hat{U}(t, t') = \hat{U}_0(t, t') - \mathrm{i}\int_{t'}^{t} \mathrm{d}t''\, \hat{U}(t, t'')\hat{W}(t'')\hat{U}_0(t'', t') \tag{2.7}$$

$$= \hat{U}_0(t, t') - \mathrm{i}\int_{t'}^{t} \mathrm{d}t''\, \hat{U}_0(t, t'')\hat{W}(t'')\hat{U}(t'', t') \tag{2.8}$$

which is readily confirmed via equation (2.6). $\hat{U}_0(t, t')$ is the time-evolution operator corresponding to $\hat{H}_0$. The expression (2.7) is now inserted into the matrix element (2.1) to find

$$M_{\boldsymbol{p}}(t) = -\mathrm{i}\int_{t_i}^{t} \mathrm{d}t'\, \langle \Psi_{\boldsymbol{p}}|\hat{U}(t, t')\hat{W}(t')|\Psi_0(t')\rangle \tag{2.9}$$

where $|\Psi_0(t)\rangle = \hat{U}_0(t, t_i)|\Psi_0\rangle$ and $\langle \Psi_{\boldsymbol{p}}|\Psi_0(t)\rangle = 0$ are used. The latter comes from $|\Psi_{\boldsymbol{p}}\rangle$ being a scattering state corresponding to a free electron whereas $|\Psi_0(t)\rangle$ is a time-evolved bound state orthogonal to $|\Psi_{\boldsymbol{p}}\rangle$.

Similar to the splitting of the evolution operator in equation (2.7) one can use $\hat{H}(t) = \hat{H}^{(\mathrm{V})}(t) + \hat{V}(\boldsymbol{r})$ to arrive at the following equations:

$$\hat{U}(t, t') = \hat{U}^{(\mathrm{V})}(t, t') - \mathrm{i}\int_{t'}^{t} \mathrm{d}t''\, \hat{U}(t, t'')\hat{V}(\boldsymbol{r})\hat{U}^{(\mathrm{V})}(t'', t') \tag{2.10}$$

$$= \hat{U}^{(\mathrm{V})}(t, t') - \mathrm{i}\int_{t'}^{t} \mathrm{d}t''\, \hat{U}^{(\mathrm{V})}(t, t'')\hat{V}(\boldsymbol{r})\hat{U}(t'', t')\,. \tag{2.11}$$

Here $\hat{U}^{(\mathrm{V})}(t, t')$ is the evolution operator corresponding to the Gordon-Volkov-Hamiltonian $\hat{H}^{(\mathrm{V})}(t)$. Equation (2.10) is now plugged into the matrix element (2.9) which

yields [14]

$$M_{\boldsymbol{p}}(t) = -\mathrm{i}\int_{t_i}^{t} \mathrm{d}t' \, \langle \Psi_{\boldsymbol{p}}| \left[\hat{U}^{(\mathrm{V})}(t,t') - \mathrm{i}\int_{t'}^{t} \mathrm{d}t'' \, \hat{U}^{(\mathrm{V})}(t,t'')\hat{V}(\boldsymbol{r})\hat{U}(t'',t')\right] \hat{W}(t')|\Psi_0(t')\rangle \,. \tag{2.12}$$

Using the identity

$$\int_{t_i}^{t} \mathrm{d}t' \int_{t'}^{t} \mathrm{d}t'' = \int_{t_i}^{t} \mathrm{d}t'' \int_{t_i}^{t} \mathrm{d}t' \, \Theta(t''-t') = \int_{t_i}^{t} \mathrm{d}t'' \int_{t_i}^{t''} \mathrm{d}t' \tag{2.13}$$

and renaming the integration variables in the second term appropriately leads to

$$\begin{aligned} M_{\boldsymbol{p}}(t) = -\mathrm{i}\int_{t_i}^{t} \mathrm{d}t' \, \langle \Psi_{\boldsymbol{p}}|\hat{U}^{(\mathrm{V})}(t,t') \Bigg[& \hat{W}(t')|\Psi_0(t')\rangle \\ & -\mathrm{i}\int_{t_i}^{t'} \mathrm{d}t'' \, \hat{V}(\boldsymbol{r})\hat{U}(t',t'')\hat{W}(t'')|\Psi_0(t'')\rangle \Bigg] \end{aligned} \tag{2.14}$$

which is still exact and gauge invariant (the problem of gauges is discussed in [35], or [32], section 7.3.4). This equation is already quite interesting in terms of the physical interpretation it allows. The first term describes a bound state, a single interaction with the laser field and a free propagation in the latter. The second term additionally contains a propagation under the influence of both Coulomb potential and laser field and another interaction with the atomic potential. This second term can be (and indeed is) interpreted as the rescattering part of the transition amplitude. It contains the full time-evolution operator which remains unknown. The first term includes the part of the transition amplitude corresponding to direct ionization and shall be the one of interest here.

A necessary ingredient for the approximations applied to equation (2.14) is the expansion of $\hat{U}^{(\mathrm{V})}(t,t')$ in so-called Gordon-Volkov waves $|\Psi_{\boldsymbol{p}}^{(\mathrm{V})}(t)\rangle$ which obey the Schrödinger equation

$$\mathrm{i}\frac{\mathrm{d}}{\mathrm{d}t}|\Psi_{\boldsymbol{p}}^{(\mathrm{V})}(t)\rangle = \hat{H}^{(\mathrm{V})}(t)|\Psi_{\boldsymbol{p}}^{(\mathrm{V})}(t)\rangle \,. \tag{2.15}$$

This equation can be solved for $|\Psi_{\boldsymbol{p}}^{(\mathrm{V})}(t)\rangle$ using a specific notation for $\hat{H}^{(\mathrm{V})}(t)$. This is equivalent to the choice of a specific gauge, here the velocity gauge where $\hat{H}^{(\mathrm{V})}(t) = \frac{1}{2}[\hat{\boldsymbol{p}} + \boldsymbol{A}(t)]^2$. A solution to equation (2.15) can easily be found considering that the Gordon-Volkov-Hamiltonian is diagonal in momentum space:

$$|\Psi_{\boldsymbol{p}}^{(\mathrm{V})}(t,t_i)\rangle = \mathrm{e}^{-\mathrm{i}S_{\boldsymbol{p}}(t,t_i)}|\boldsymbol{p}\rangle \tag{2.16}$$

with momentum eigenstates $|\boldsymbol{p}\rangle$ (plane waves), $\langle \boldsymbol{r}|\boldsymbol{p}\rangle = \mathrm{e}^{\mathrm{i}\boldsymbol{p}\cdot\boldsymbol{r}}/(2\pi)^{3/2}$, and the action

$$S_{\boldsymbol{p}}(t,t_i) = \frac{1}{2}\int_{t_i}^{t} \mathrm{d}t' \left[\boldsymbol{p} + \boldsymbol{A}(t')\right]^2 . \tag{2.17}$$

The expansion for the time-evolution operator is now

$$\hat{U}^{(\mathrm{V})}(t,t') = \int \mathrm{d}^3k \, |\Psi_{\boldsymbol{k}}^{(\mathrm{V})}(t,t_i)\rangle\langle\Psi_{\boldsymbol{k}}^{(\mathrm{V})}(t',t_i)| \tag{2.18}$$

where t_i is arbitrary since it cancels out.

The next step is to apply approximations to the matrix element (2.14). The final momentum state $|\Psi_{\boldsymbol{p}}\rangle$ is replaced by a momentum eigenstate $|\boldsymbol{p}\rangle$. The second term containing the rescattering part is simply neglected. This leads to the well-known SFA or Keldysh amplitude

$$M_{\boldsymbol{p}}^{(\mathrm{SFA})}(t) = -\mathrm{i}\int_{t_i}^{t} \mathrm{d}t' \, \langle\Psi_{\boldsymbol{p}}^{(\mathrm{V})}(t',t)|\hat{W}(t')|\Psi_0(t')\rangle . \tag{2.19}$$

We could now continue with this equation and insert $\hat{W}(t) = \hat{\boldsymbol{p}}\cdot\boldsymbol{A}(t) + \frac{1}{2}\boldsymbol{A}^2(t)$ (in velocity gauge) to find the asymptotic ionization rate as in [13]. However, another possibility is to recast equation (2.19) in length gauge. Then the interaction operator $\hat{W}(t)$ and the Gordon-Volkov waves $|\Psi_{\boldsymbol{p}}^{(\mathrm{V})}(t,t_i)\rangle$ read

$$\hat{W}(t) = \hat{\boldsymbol{r}}\cdot\boldsymbol{E}(t) \tag{2.20}$$

and

$$|\Psi_{\boldsymbol{p}}^{(\mathrm{V})}(t,t_i)\rangle = \mathrm{e}^{-\mathrm{i}S_{\boldsymbol{p}}(t,t_i)}|\boldsymbol{p} + \boldsymbol{A}(t)\rangle , \tag{2.21}$$

respectively. The time evolution of the bound state $|\Psi_0\rangle$ is known as well,

$$|\Psi_0(t)\rangle = \mathrm{e}^{-\mathrm{i}\mathcal{E}_0(t-t_i)}|\Psi_0\rangle , \tag{2.22}$$

which is inserted into the matrix element (2.19), leading to

$$M_{\boldsymbol{p}}^{(\mathrm{SFA})}(t) = -\mathrm{i}\int_{t_i}^{t} \mathrm{d}t' \, \mathrm{e}^{-\mathrm{i}S_{\boldsymbol{p}}(t,t')}\mathrm{e}^{-\mathrm{i}\mathcal{E}_0(t'-t_i)}\langle\boldsymbol{p} + \boldsymbol{A}(t')|\hat{\boldsymbol{r}}\cdot\boldsymbol{E}(t')|\Psi_0\rangle . \tag{2.23}$$

Here, special care has to be taken of the choice of the time variable in $\langle\boldsymbol{p} + \boldsymbol{A}(t)|$ as this is not immediately clear from the notation. Closer inspection shows that it must be the integration variable t'. Multiplying this equation with a constant phase factor $\mathrm{e}^{\mathrm{i}\mathcal{E}_0(t-t_i)}$ (which vanishes when calculating the absolute square, i.e., the transition probability) and considering that the laser field is present only between

$t_i = 0$ and $t = T_\mathrm{p}$ yields the total transition matrix element

$$M_{\boldsymbol{p}}^{(\mathrm{SFA})} = -\mathrm{i}\int_0^{T_\mathrm{p}} \mathrm{d}t\, \langle \boldsymbol{p} + \boldsymbol{A}(t)|\hat{\boldsymbol{r}}\cdot\boldsymbol{E}(t)|\Psi_0\rangle \mathrm{e}^{-\mathrm{i}S_{\boldsymbol{p},I_\mathrm{p}}(T_\mathrm{p},t)} \tag{2.24}$$

with the action

$$S_{\boldsymbol{p},I_\mathrm{p}}(t,t') = \int_{t'}^{t} \mathrm{d}t'' \left(\frac{1}{2}[\boldsymbol{p} + \boldsymbol{A}(t'')]^2 + I_\mathrm{p}\right). \tag{2.25}$$

Here $I_\mathrm{p} = |\mathcal{E}_0|$ is the ionization potential of the bound state. The remaining matrix element can be evaluated assuming a hydrogen-like bound state $|\Psi_0\rangle$ (see [17] or [32], section 7.3.5),

$$\begin{aligned}\langle \boldsymbol{k}|\hat{\boldsymbol{r}}\cdot\boldsymbol{E}(t)|\Psi_0\rangle &= \mathrm{i}\boldsymbol{\nabla}_{\boldsymbol{k}}\langle \boldsymbol{k}|\Psi_0\rangle\cdot\boldsymbol{E}(t)\\ &= -\mathrm{i}2^{7/2}(2I_\mathrm{p})^{5/4}\frac{\boldsymbol{k}\cdot\boldsymbol{E}(t)}{\pi(k^2+2I_\mathrm{p})^3},\end{aligned} \tag{2.26}$$

where we used that in momentum space $\hat{\boldsymbol{r}} = \mathrm{i}\boldsymbol{\nabla}_{\boldsymbol{k}}$ and $\langle \boldsymbol{k}|\Psi_0\rangle$ being the projection of $|\Psi_0\rangle$ into momentum space. The full derivation of equation (2.26) is given in appendix A.2. This result is plugged into equation (2.24) to find the final result for the transition matrix element of direct ionization

$$\begin{aligned}M_{\boldsymbol{p}}^{(\mathrm{SFA})} &= -2^{7/2}(2I_\mathrm{p})^{5/4}\int_0^{T_\mathrm{p}} \mathrm{d}t\, \frac{[\boldsymbol{p}+\boldsymbol{A}(t)]\cdot\boldsymbol{E}(t)}{\pi([\boldsymbol{p}+\boldsymbol{A}(t)]^2+2I_\mathrm{p})^3}\mathrm{e}^{-\mathrm{i}S_{\boldsymbol{p},I_\mathrm{p}}(T_\mathrm{p},t)}\\ &= -\int_0^{T_\mathrm{p}} \mathrm{d}t\, f_{\boldsymbol{p},I_\mathrm{p}}(t)\mathrm{e}^{-\mathrm{i}S_{\boldsymbol{p},I_\mathrm{p}}(T_\mathrm{p},t)}\end{aligned} \tag{2.27}$$

with

$$f_{\boldsymbol{p},I_\mathrm{p}}(t) = 2^{7/2}(2I_\mathrm{p})^{5/4}\frac{[\boldsymbol{p}+\boldsymbol{A}(t)]\cdot\boldsymbol{E}(t)}{\pi([\boldsymbol{p}+\boldsymbol{A}(t)]^2+2I_\mathrm{p})^3}. \tag{2.28}$$

Equation (2.27) can be evaluated numerically, finding the transition probability $w_{\boldsymbol{p}} = \left|M_{\boldsymbol{p}}^{(\mathrm{SFA})}\right|^2$ (see appendix B.2 for details on the latter) for any $\boldsymbol{p}$ and thus building up a momentum-resolved photoelectron spectrum.

In the previous paragraphs only direct emission was considered. However, in many cases it is important to include rescattering effects. This can be done in the framework of the SFA starting from equation (2.14) which is still exact and can be

split into two terms,

$$M_{\boldsymbol{p}}(t) = M_{\boldsymbol{p}}^{(\mathrm{SFA,dir})}(t) + M_{\boldsymbol{p}}^{(\mathrm{SFA,resc})}(t) \tag{2.29}$$

$$M_{\boldsymbol{p}}^{(\mathrm{SFA,dir})}(t) = -\mathrm{i}\int_{t_i}^{t} \mathrm{d}t' \, \langle \Psi_{\boldsymbol{p}} | \hat{U}^{(\mathrm{V})}(t,t') \hat{W}(t') | \Psi_0(t') \rangle \tag{2.30}$$

$$M_{\boldsymbol{p}}^{(\mathrm{SFA,resc})}(t) = -\int_{t_i}^{t} \mathrm{d}t' \int_{t_i}^{t'} \mathrm{d}t'' \, \langle \Psi_{\boldsymbol{p}} | \hat{U}^{(\mathrm{V})}(t,t') \hat{V}(\boldsymbol{r}) \hat{U}(t',t'') \hat{W}(t'') | \Psi_0(t'') \rangle \,, \tag{2.31}$$

where the first term $M_{\boldsymbol{p}}^{(\mathrm{SFA,dir})}(t)$ has already been evaluated above. The second term can be simplified in a similar way (see [14, 32]). We replace the full time-evolution operator $\hat{U}(t',t'')$ by $\hat{U}^{(\mathrm{V})}(t',t'')$ which means that we restrict the calculations to a single rescattering event. This yields

$$M_{\boldsymbol{p}}^{(\mathrm{SFA,resc})}(t) = -\int_{t_i}^{t} \mathrm{d}t' \int_{t_i}^{t'} \mathrm{d}t'' \, \langle \Psi_{\boldsymbol{p}}^{(\mathrm{V})}(t',t) | \hat{V}(\boldsymbol{r}) \hat{U}^{(\mathrm{V})}(t',t'') \hat{W}(t'') | \Psi_0(t'') \rangle \tag{2.32}$$

where an integration over the intermediate momentum $\boldsymbol{k}$ appears due to the expansion of the Gordon-Volkov time-evolution operator $\hat{U}^{(\mathrm{V})}(t',t'')$. This integration can be approximated via saddle-point analysis. After appropriately transforming the integration variables the rescattering matrix element reads

$$\begin{aligned} M_{\boldsymbol{p}}^{(\mathrm{SFA,resc})} = -\int_0^{T_\mathrm{p}} \mathrm{d}t \, \mathrm{e}^{\mathrm{i}S_{\boldsymbol{p},I_\mathrm{p}}(t,0)} \int_0^t \mathrm{d}\tau \, \left(\frac{2\pi}{\mathrm{i}\tau}\right)^{3/2} V_{\boldsymbol{p}-\boldsymbol{k}_s(t,\tau)} \mathrm{e}^{-\mathrm{i}S_{\boldsymbol{k}_s(t,\tau),I_\mathrm{p}}(t,t-\tau)} \\ \times \langle \boldsymbol{k}_s(t,\tau) + \boldsymbol{A}(t-\tau) | \boldsymbol{r} \cdot \boldsymbol{E}(t-\tau) | \Psi_0 \rangle \end{aligned} \tag{2.33}$$

where the intermediate momentum $\boldsymbol{k}$ is determined using the saddle-point condition

$$\boldsymbol{\nabla}_{\boldsymbol{k}} S_{\boldsymbol{k},I_\mathrm{p}}(t,t-\tau) = 0 \qquad \rightarrow \qquad \boldsymbol{k}_s(t,\tau) = -\frac{\boldsymbol{\alpha}(t) - \boldsymbol{\alpha}(t-\tau)}{\tau} \tag{2.34}$$

with the excursion $\boldsymbol{\alpha}(t) = \int^t \mathrm{d}t' \boldsymbol{A}(t')$. The scattering matrix element $V_{\boldsymbol{p}-\boldsymbol{k}} = \langle \boldsymbol{p} | \hat{V} | \boldsymbol{k} \rangle$ for scattering potentials of the form

$$V(r) = -\left(b + \frac{a}{r}\right) \mathrm{e}^{-\lambda r} \tag{2.35}$$

reads

$$V_{\boldsymbol{p}-\boldsymbol{k}} = -\frac{2b\lambda + aC}{2\pi^2 C^2} \,, \qquad C = (\boldsymbol{p}-\boldsymbol{k})^2 + \lambda^2 \,. \tag{2.36}$$

The numerical evaluation of $M_{\boldsymbol{p}}^{(\mathrm{SFA,dir})}$ (2.27) and $M_{\boldsymbol{p}}^{(\mathrm{SFA,resc})}$ (2.33) yields momentum-resolved photoelectron spectra as shown exemplarily in figure 2.1 for a $\sin^2$-shaped laser pulse linearly polarized in z-direction given by the vector potential

$$\boldsymbol{A}(t) = \boldsymbol{e}_z A_0 \sin^2(\omega t/(2n_c)) \sin(\omega t) \,. \tag{2.37}$$

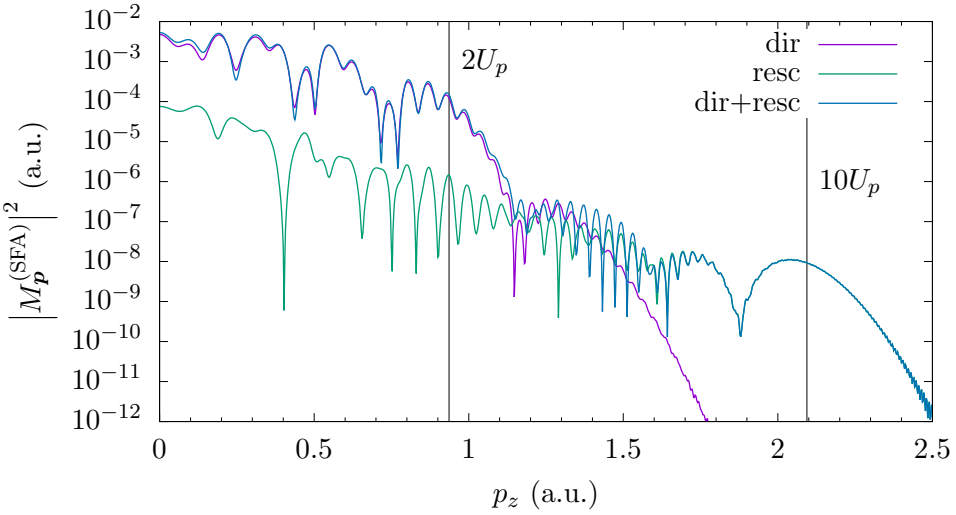

Figure 2.1.: Photoelectron momentum spectrum for a single hydrogen atom initially in the ground state irradiated by a six-cycle $\sin^2$-shaped laser pulse linearly polarized in z-direction with wavelength $\lambda = 800\,\mathrm{nm}$ and intensity $I = 1 \times 10^{14}\,\mathrm{W/cm^2}$. The spectrum is obtained by numerically evaluating equations (2.27) and (2.33). Shown are the contributions of direct (dir) and rescattering (resc) matrix element and their coherent sum (dir+resc). Indicated are the cutoff momenta for direct emission ($2U_\mathrm{p}$) and rescattering ($10U_\mathrm{p}$).

From the electric field $\boldsymbol{E}(t) = -\frac{\mathrm{d}}{\mathrm{d}t}\boldsymbol{A}(t)$ we find $A_0 = -E_0/\omega$ where E_0 is the amplitude of the electric field. The laser pulse has $n_c = 6$ optical cycles with wavelength $\lambda = 800\,\mathrm{nm}$ and intensity $I = 1 \times 10^{14}\,\mathrm{W/cm^2}$. Target is a hydrogen atom initially in the ground state. The figure shows the direct contribution $M_{\boldsymbol{p}}^{(\mathrm{SFA,dir})}$ (dir), the rescattering contribution $M_{\boldsymbol{p}}^{(\mathrm{SFA,resc})}$ (resc) and the coherent sum of both (dir+resc). Indicated are the direct cutoff at $2U_\mathrm{p}$ and the rescattering cutoff at $10U_\mathrm{p}$ (see section 2.4 on how these cutoffs are derived). U_p is given in terms of the laser parameters as

$$U_\mathrm{p} = \frac{E_0^2}{4\omega^2}\,. \tag{2.38}$$

The graphs visualize several features that are common to most strong-field ionization spectra. Up to $2U_\mathrm{p}$ the direct part dominates the spectrum. That part shows two different interference patterns, the large-scale intra-cycle interference and the small-scale inter-cycle interference (both of which are well understood, see e.g. [36]). After the cutoff the rescattering part takes over and extends the spectrum in a plateau up to $10U_\mathrm{p}$. Beyond that energy the yield rapidly decreases.

2.3. Quantum Trajectories

Apart from straightforward numerical evaluation the matrix element (2.24) provides the opportunity for physical interpretation in terms of trajectories. To achieve this, another approximation must be made, in particular the saddle-point approximation (SPA). It states that a contour integral of the form

$$\int_C f(x)\mathrm{e}^{\lambda S(x)}\mathrm{d}x \tag{2.39}$$

where C is the contour and λ is large can be approximated (see appendix A.3 for a sketch of the derivation) by a sum over saddle-points x_s of $S(x)$ as

$$\int_C f(x)\mathrm{e}^{\lambda S(x)}\mathrm{d}x \approx \sqrt{2\pi}\sum_{x_s} f(x_s)\frac{\mathrm{e}^{\lambda S(x_s)}}{\sqrt{-\lambda S''(x_s)}}\,. \tag{2.40}$$

The saddle-points x_s are defined by $S'(x_s) = 0$ where S' denotes the derivative of S.

This method shall be applied to equation (2.27). The saddle-point equation (SPE) $S'(x_s) = 0$ in this case reads

$$\left[\frac{\mathrm{d}}{\mathrm{d}t}S_{\boldsymbol{p},I_\mathrm{p}}(t)\right]_{t=t_s} = \left[\frac{\mathrm{d}}{\mathrm{d}t}\int_t^{T_\mathrm{p}}\mathrm{d}t'\left(\frac{1}{2}[\boldsymbol{p}+\boldsymbol{A}(t')]^2 + I_\mathrm{p}\right)\right]_{t=t_s} \tag{2.41}$$

$$= -\frac{1}{2}[\boldsymbol{p}+\boldsymbol{A}(t_s)]^2 - I_\mathrm{p} \tag{2.42}$$

$$\stackrel{!}{=} 0 \tag{2.43}$$

or equivalently

$$[\boldsymbol{p}+\boldsymbol{A}(t_s)]^2 \stackrel{!}{=} -2I_\mathrm{p}\,. \tag{2.44}$$

This equation has two severe consequences. First, the right-hand side is strictly negative for non-vanishing I_p, so the term in the parentheses on the left-hand side must be complex. As $\boldsymbol{p}$ is an observable and thus real by definition, $\boldsymbol{A}(t_s)$ and accordingly t_s must have a non-vanishing imaginary part.

Second, we need to plug t_s into the matrix element (2.27) in SPA,

$$M_{\boldsymbol{p}}^{(\mathrm{SFA})} = -\sqrt{2\pi}\sum_s f_{\boldsymbol{p},I_\mathrm{p}}(t_s)\frac{\mathrm{e}^{-\mathrm{i}S_{\boldsymbol{p},I_\mathrm{p}}(T_\mathrm{p},t_s)}}{\sqrt{S''_{\boldsymbol{p},I_\mathrm{p}}(t_s)}}\,, \tag{2.45}$$

with the same prefactor (2.28) as before (but neglecting a constant phase factor). The problem becomes obvious when considering the denominator of the prefactor, which vanishes at t_s. This poses a difficulty in applying the SPA to equation (2.27) in a straightforward way. A possible solution to this is presented in [17], section 6.3,

where the method is modified to circumvent the emerging divergence. The resulting equation for the matrix element (2.27) in SPA finally reads[1]

$$M_{\boldsymbol{p}}^{(\mathrm{SFA})} = -2^{-1/2}(2I_\mathrm{p})^{5/4} \sum_s \frac{\mathrm{e}^{-\mathrm{i}S_{\boldsymbol{p},I_\mathrm{p}}(t_s)}}{S''_{\boldsymbol{p},I_\mathrm{p}}(t_s)} \tag{2.46}$$

with the action defined as

$$S_{\boldsymbol{p},I_\mathrm{p}}(t) = \int_t^{T_\mathrm{p}} \mathrm{d}t' \left(\frac{1}{2}[\boldsymbol{p} + \boldsymbol{A}(t')]^2 + I_\mathrm{p} \right) . \tag{2.47}$$

The upper boundary $T_\mathrm{p} \in \mathbb{R}$ is arbitrary as it only accounts for an overall phase factor in (2.46) which vanishes when calculating the probability $\sim |M_{\boldsymbol{p}}|^2$ (see appendix B.2).

A possible physical interpretation of equation (2.46) is that every t_s is the starting point for an electron trajectory tunneling out of the atomic potential and propagating to the detector. For any momentum $\boldsymbol{p}$ several of these starting (or ionization) times t_s can be found from the SPE (2.44) depending on the laser pulse defined by $\boldsymbol{A}(t)$. Note that the drift momentum $\boldsymbol{p}$ is constant which means that the momentum $\boldsymbol{p}$ in the SPE is equal to the final momentum $\boldsymbol{p}$ at the detector. The contributions of these trajectories are added up coherently following equation (2.46), thereby determining the spectrum. For typical laser pulses these contributions can even be evaluated analytically, except for the saddle-point equation (2.44) which must be solved numerically or graphically due to its transcendental nature.

Weight of a single trajectory Let us consider a linearly polarized flat-top pulse which is defined as $\boldsymbol{A}(t) = \boldsymbol{e}_z A_0 \sin(\omega t)$ but also satisfies $\boldsymbol{A}(t \to \pm\infty) = 0$. The ramping up and down may for now be neglected. For each optical cycle and specified momentum $\boldsymbol{p}$ there are two different solutions t_s to the SPE (2.44) with equal imaginary parts $\operatorname{Im} t_s$ which repeat every cycle. This changes when using a finite pulse, e.g. $\boldsymbol{A}(t) = \boldsymbol{e}_z A_0 \sin^2(\omega t/(2n_c)) \sin(\omega t)$ for $0 \le \omega t \le 2\pi n_c$ and 0 otherwise, with a finite number of optical cycles n_c. For a long pulse many different solutions t_s can contribute to the transition matrix element $M_{\boldsymbol{p}}^{(\mathrm{SFA})}$. To reduce the effort it is useful to know beforehand which solutions have the largest contribution to the spectrum. The importance of this will become clear in chapter 3. To that end we estimate the weight $w_{\boldsymbol{p}}(t_s)$ corresponding to a single solution t_s by analyzing the exponential term in the transition matrix element (2.46),

$$M_{\boldsymbol{p}}(t_s) \propto \exp\left\{-\mathrm{i}S_{\boldsymbol{p},I_\mathrm{p}}(t_s)\right\} . \tag{2.48}$$

[1] Please note that in the denominator we have S'' instead of $\sqrt{S''}$ (as in equation (2.45)) as a result of the derivation in [17].

The weight of a single trajectory can thus be expressed as

$$w_{\boldsymbol{p}}(t_s) \propto \left|\exp\left\{-\mathrm{i}S_{\boldsymbol{p},I_\mathrm{p}}(t_s)\right\}\right|^2 \tag{2.49}$$

$$\propto \exp\left\{2\mathrm{Im}\, S_{\boldsymbol{p},I_\mathrm{p}}(t_s)\right\} . \tag{2.50}$$

Since the integration contour for the integral in equation (2.47) is arbitrary we can calculate the imaginary part of S,

$$\mathrm{Im}\, S_{\boldsymbol{p},I_\mathrm{p}}(t_s) = \mathrm{Im}\left\{\int_{t_s}^{T_\mathrm{p}} \mathrm{d}t' \left(\frac{1}{2}[\boldsymbol{p}+\boldsymbol{A}(t')]^2 + I_\mathrm{p}\right)\right\} . \tag{2.51}$$

We replace $t' = \mathrm{Re}\, t_s + \mathrm{i}\tau$ and the limits accordingly since the integration along the real axis does not contribute to $\mathrm{Im}\, S$,

$$\mathrm{Im}\, S_{\boldsymbol{p},I_\mathrm{p}}(t_s) = \int_{\mathrm{Im}\, t_s}^{0} \mathrm{d}\tau\, \mathrm{Re}\left(\frac{1}{2}[\boldsymbol{p}+\boldsymbol{A}(\mathrm{Re}\, t_s + \mathrm{i}\tau)]^2 + I_\mathrm{p}\right) \tag{2.52}$$

$$= -\left(\frac{1}{2}\boldsymbol{p}^2 + I_\mathrm{p}\right)\mathrm{Im}\, t_s + \boldsymbol{p}\cdot\int_{\mathrm{Im}\, t_s}^{0} \mathrm{d}\tau\, \mathrm{Re}\, \boldsymbol{A}(\mathrm{Re}\, t_s + \mathrm{i}\tau)$$

$$+ \frac{1}{2}\int_{\mathrm{Im}\, t_s}^{0} \mathrm{d}\tau\, \mathrm{Re}\, \boldsymbol{A}^2(\mathrm{Re}\, t_s + \mathrm{i}\tau) . \tag{2.53}$$

For further evaluation we need the form of the vector potential. As we only need an approximate result it is sufficient to use the flat-top expression from above,

$$\boldsymbol{A}(t) = \boldsymbol{e}_z A_0 \sin(\omega t) \tag{2.54}$$

$$= \boldsymbol{e}_z A_0 \left[\sin(\mathrm{Re}\,\omega t)\cosh(\mathrm{Im}\,\omega t) + \mathrm{i}\cos(\mathrm{Re}\,\omega t)\sinh(\mathrm{Im}\,\omega t)\right] . \tag{2.55}$$

Assuming that the imaginary part of t_s is small we can linearize the former expression in $\mathrm{Im}\, t$ leading to $\cosh(\mathrm{Im}\,\omega t) \approx 1$, $\sinh(\mathrm{Im}\,\omega t) \approx \mathrm{Im}\,\omega t$ and thus

$$\boldsymbol{A}(t) \approx \boldsymbol{e}_z A_0 \left[\sin(\mathrm{Re}\,\omega t) + \mathrm{i}\cos(\mathrm{Re}\,\omega t)\mathrm{Im}\,\omega t\right] . \tag{2.56}$$

Plugging this into equation (2.53) and neglecting all terms $\mathcal{O}\left((\mathrm{Im}\,\tau)^2\right)$ yields

$$\mathrm{Im}\, S_{\boldsymbol{p},I_\mathrm{p}}(t_s) \approx -\left(\frac{1}{2}\boldsymbol{p}^2 + I_\mathrm{p}\right)\mathrm{Im}\, t_s - \boldsymbol{p}\cdot\boldsymbol{e}_z A_0 \sin(\mathrm{Re}\,\omega t_s)\,\mathrm{Im}\, t_s$$

$$- \frac{1}{2}A_0^2 \sin^2(\mathrm{Re}\,\omega t_s)\,\mathrm{Im}\, t_s . \tag{2.57}$$

For the flat-top pulse and under the assumption that $\operatorname{Im} t_s$ is small we can also solve the SPE (2.44) in linear approximation to find

$$\boldsymbol{p} \approx -\boldsymbol{e}_z A_0 \sin(\operatorname{Re} \omega t_s) \,. \tag{2.58}$$

Using this to simplify equation (2.57) we find that all but one term cancel, leading to the final estimate[2]

$$\operatorname{Im} S_{\boldsymbol{p},I_\mathrm{p}}(t_s) \approx -I_\mathrm{p} \operatorname{Im} t_s \,. \tag{2.59}$$

The result is linear in $\operatorname{Im} t_s$, and always negative for $\operatorname{Im} t_s > 0$. This allows us to eliminate saddle-point times with negative imaginary part since in that case the weight would increase with increasing ionization potential I_p, which is unphysical. By combining equations (2.50) and (2.59) we can conclude that the weight of a single trajectory always decreases with increasing imaginary part of the saddle-point time. This simple result has very convenient consequences. It allows to sort the saddle-point times for a specified momentum by their imaginary part and select the most relevant solutions without having to evaluate the corresponding individual transition matrix element in the first place.

2.4. Simple Man's Theory

As already mentioned above, equation (2.46) can be interpreted as a sum over quantum trajectories. These are close to classical trajectories as used in e.g. [37]. Theories based on these classical trajectories are so-called simple man's theories (SMT). In analogy to the SFA in SPA photoelectron spectra (PES) are obtained by summing over trajectory contributions of classical trajectories. The weight of a single trajectory is determined by a tunneling rate formula (as from [16] or similar) considering the instantaneous electric field at ionization time t_ion. The initial conditions are

$$\boldsymbol{r}(t_\mathrm{ion}) = 0 \,, \qquad \boldsymbol{v}(t_\mathrm{ion}) = \boldsymbol{p} + \boldsymbol{A}(t_\mathrm{ion}) = 0 \tag{2.60}$$

where $\boldsymbol{p}$ is constant and denotes the initial drift momentum. This means the electron starts at the position of the ion (or at the "tunnel exit") with zero kinetic energy. As in tunneling rate formulas the weight follows the absolute value of the electric field, the most probable trajectory is the one with $\boldsymbol{p} = 0$. The motion of the electron is

[2] In order to reproduce ionization rates (without Coulomb correction) known from the literature [16] linearization in $\operatorname{Im} \tau$ is not sufficient.

governed by the laser field,

$$\boldsymbol{v}(t) = -\int_{t_{\mathrm{ion}}}^{t} \mathrm{d}t'\, \boldsymbol{E}(t') = \boldsymbol{A}(t) - \boldsymbol{A}(t_{\mathrm{ion}}) = \boldsymbol{p} + \boldsymbol{A}(t) \tag{2.61a}$$

$$\begin{aligned}\boldsymbol{r}(t) &= \int_{t_{\mathrm{ion}}}^{t} \mathrm{d}t'\, \boldsymbol{v}(t') = \int_{t_{\mathrm{ion}}}^{t} \mathrm{d}t' \boldsymbol{A}(t') - \boldsymbol{A}(t_{\mathrm{ion}})(t - t_{\mathrm{ion}}) \\ &= \boldsymbol{\alpha}(t) - \boldsymbol{\alpha}(t_{\mathrm{ion}}) - \boldsymbol{A}(t_{\mathrm{ion}})(t - t_{\mathrm{ion}})\end{aligned} \tag{2.61b}$$

where the elongation

$$\boldsymbol{\alpha}(t) = \int^{t} \mathrm{d}t'\, \boldsymbol{A}(t') \tag{2.62}$$

has been used. Assuming that

$$\boldsymbol{A}(0) = \boldsymbol{A}(T_{\mathrm{p}}) = 0 \tag{2.63}$$

where T_{p} is the pulse duration we find that the final velocity of the electron is determined by the vector potential at ionization time, $\boldsymbol{v}(T_{\mathrm{p}}) = -\boldsymbol{A}(t_{\mathrm{ion}})$. From this we can infer the maximum kinetic energy of directly emitted electrons,

$$E_{\mathrm{kin}}^{(\mathrm{dir})} = \frac{1}{2}\boldsymbol{A}^2(t_{\mathrm{ion}}) \leq 2U_{\mathrm{p}}\,, \tag{2.64}$$

which reflects in the PES (see figure 2.1) as the famous $2U_{\mathrm{p}}$ cutoff[3] for direct ionization. The ponderomotive energy

$$U_{\mathrm{p}} = \frac{E_0^2}{4\omega^2} = \frac{1}{4}A_0^2 \tag{2.65}$$

used here is the kinetic energy of an electron in a laser field averaged over one optical cycle.

The cutoff energy for electrons rescattering once at the parent ion can be calculated by using the rescattering condition

$$|\boldsymbol{r}(t_{\mathrm{resc}})| \leq \epsilon \tag{2.66}$$

at the rescattering time $t_{\mathrm{resc}} > t_{\mathrm{ion}}$ for some small $\epsilon > 0$. At the instant of rescattering the modulus of the momentum is conserved but the direction is changed, where the extreme case is 180° back-reflection. The maximum kinetic energy resulting from this can be found numerically or graphically as

$$E_{\mathrm{kin}}^{(\mathrm{resc})} \leq 10U_{\mathrm{p}}\,, \tag{2.67}$$

[3]The SMT predicts vanishing probability for electrons emitted with maximum kinetic energy $2U_{\mathrm{p}}$ and thus fails dramatically to reproduce the features depicted in figure 2.1. A solution to this problem is presented in chapter 4.

which is also visible in the PES in figure 2.1. Details for its derivation are given in [32], section 7.3.6.

Classification of Trajectories The trajectories used above can be classified into two different species, called *long* and *short* trajectories. This is due to their behavior in position space close to the ionization time t_{ion}. The short trajectories leave the ion directly towards the detector, while the long ones first propagate in the opposite direction and pass the ion (at least) once before reaching the detector. Mathematically this can be seen in equation (2.61a). The velocity is initially zero. Depending on whether t_{ion} lies on the rising or falling edge of the vector potential $\boldsymbol{A}(t)$, the velocity of the electron right after ionization has the same direction as $\boldsymbol{p}$ (short) or the opposite direction (long). This is visualized in figure 2.2 where equation (2.61b) has been plotted for two different ionization times within the same half-cycle corresponding to the same momentum $\boldsymbol{p}$. We assume a plane wave linearly polarized in z direction, the laser parameters are the same as in figure 2.1.

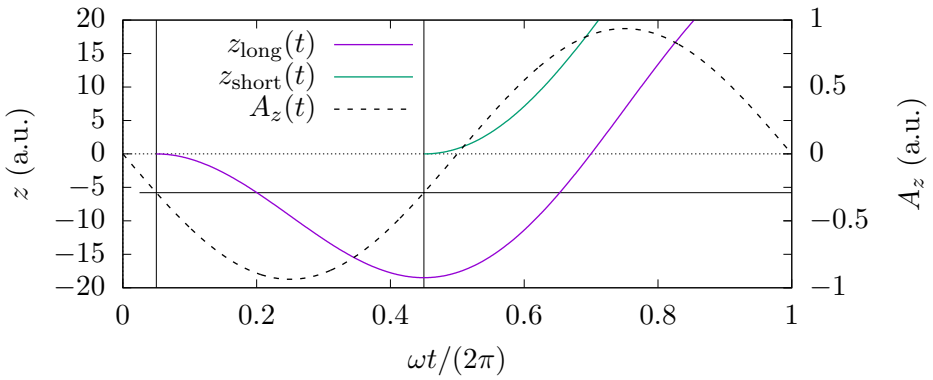

Figure 2.2.: Two different trajectories $z(t)$ in polarization direction following equation (2.61b) for different ionization times (indicated by black vertical lines) corresponding to the same momentum $\boldsymbol{p} = 0.29$. The laser parameters are the same as in figure 2.1. The black horizontal line is the graphical interpretation of $-\boldsymbol{p} = \boldsymbol{A}(t_{\text{ion}})$ following from the initial condition (2.60) for $\boldsymbol{v}(t_{\text{ion}})$.

These two different classes of trajectories from the same half-cycle give rise to the well-known intra-cycle interference pattern [36]. Although they yield identical contributions to the spectrum in the plain SFA, they can behave quite differently when extending the SFA towards external potentials. Some cases where this is important are discussed in the following chapters.

3. Single Electrons in a Time-Dependent External Potential

3.1. Motivation

In the introductory part the strong field approximation (SFA) was presented which considers the emission of a single electron from a single atom. However, topic of this work is the calculation of photoelectron spectra (PES) beyond the plain SFA. One example for looking beyond a single electron emitted from a single atom are metal clusters. Previous ionization experiments with silver clusters [38] show features in the PES at energies far beyond the expected $2U_\mathrm{p}$ (or $10U_\mathrm{p}$ when rescattering once) known from atomic spectra [17, 32]. The conclusion is that the collective field within the cluster, which arises due to coherent oscillations of the valence electrons with respect to the ionic background, can significantly influence the energy emitted electrons gain in rescattering events. In [38] this effect is termed surface-plasmon assisted rescattering in clusters (SPARC).

The experiment uses a pump-probe setup where the pump pulse excites the cluster which leads to expansion of the latter. The measured photoelectrons are generated by the probe pulse ionizing the cluster. We simplify the situation by assuming the cluster to consist of two homogeneously charged spheres with equal but opposite charges. The positively charged ion sphere is fixed while the negative electron cloud can oscillate due to the laser pulse. This model is called rigid-sphere model (RSM). The validity of the RSM is supported by simulations within the framework of time-dependent density functional theory (TD-DFT). The pump pulse is not simulated, but the expansion of the cluster is assumed to be slow compared to the laser period, so that during the probe pulse the cluster diameter does not change. The pump-probe delay is then included through variation of the cluster diameter.

This chapter includes results already published in [39] but adds further details and in-depth explanations.

3.2. Rigid Sphere Model

As already mentioned above, the metal clusters are modeled using two rigid homogeneously charged spheres with opposite charges and equal radii. The ideas leading to this model have already been used in [40–44]. Here we assume that the cluster in total stays neutral. This greatly simplifies the calculations and furthermore allows us to discriminate collective effects from the static Coulomb corrections which result from the charging of the cluster due to ionization. Taking this into account would be straightforward and, in general, necessary to achieve quantitative agreement with experimental results. However, in this chapter we want to illustrate the application of collectively generated potentials to the trajectory-based SFA and qualitatively analyze the mechanism leading to the observed electron acceleration. Hence we neglect the charging of the cluster.

The positively charged sphere is fixed in space as it models the significantly heavier ions. Here we use sodium atoms since they have only one valence electron. However, the model applies to all materials with tightly bound core electrons and delocalized valence electrons. The negative sphere models the valence electrons. This sphere can move with respect to the ion sphere. Any displacement $\boldsymbol{d}$ of the electron sphere away from the initial position leads to an attractive force between the spheres due to the opposite charges. A derivation of the force is given in appendix A.1. Including the electric field $\boldsymbol{E}(t)$ of the laser and a damping factor γ the equation of motion (EOM) for the displacement $\boldsymbol{d}$ reads

$$\ddot{\boldsymbol{d}} = -\omega_{\mathrm{Mie}}^2 \left(\boldsymbol{d} - \frac{9}{16R}\boldsymbol{d}|\boldsymbol{d}| + \frac{1}{32R^2}\boldsymbol{d}|\boldsymbol{d}|^3 \right) - \boldsymbol{E}(t) - \gamma\dot{\boldsymbol{d}}\,. \tag{3.1}$$

Important parameters are the cluster radius R and the Mie frequency ω_{Mie} which are both related to the electron density n_0 within the cluster via

$$R = N^{1/3} r_{\mathrm{S}} \tag{3.2}$$

$$\omega_{\mathrm{Mie}} = \sqrt{\frac{4\pi}{3} n_0} = r_{\mathrm{S}}^{-3/2} \tag{3.3}$$

where N is the number of valence electrons. The Wigner-Seitz radius r_{S} describes the mean volume available per electron.

Equation (3.1) describes a driven, damped anharmonic oscillator. Damping needs to be included to prevent divergence at resonance. For linear polarization of the laser field $\boldsymbol{E}||\boldsymbol{e}_z$ the problem becomes one-dimensional, $d_z = \boldsymbol{e}_z \cdot \boldsymbol{d}$. For small excursions $d_z \ll R$ the anharmonic terms $\sim d_z^2$ and $\sim d_z^4$ can be neglected. For a monochromatic driver

$$\boldsymbol{E}(t) = \boldsymbol{e}_z E_0 \cos \omega t \tag{3.4}$$

the problem becomes analytically solvable with the solution

$$d_z(t) = d_0 \sin(\omega t + \varphi) \tag{3.5a}$$

$$d_0 = \frac{-E_0}{\sqrt{(\omega_{\text{Mie}}^2 - \omega^2)^2 + \gamma^2\omega^2}} \tag{3.5b}$$

$$\varphi = \arctan\left(\frac{\omega_{\text{Mie}}^2 - \omega^2}{\gamma\omega}\right) \tag{3.5c}$$

as known from classical mechanics textbooks.

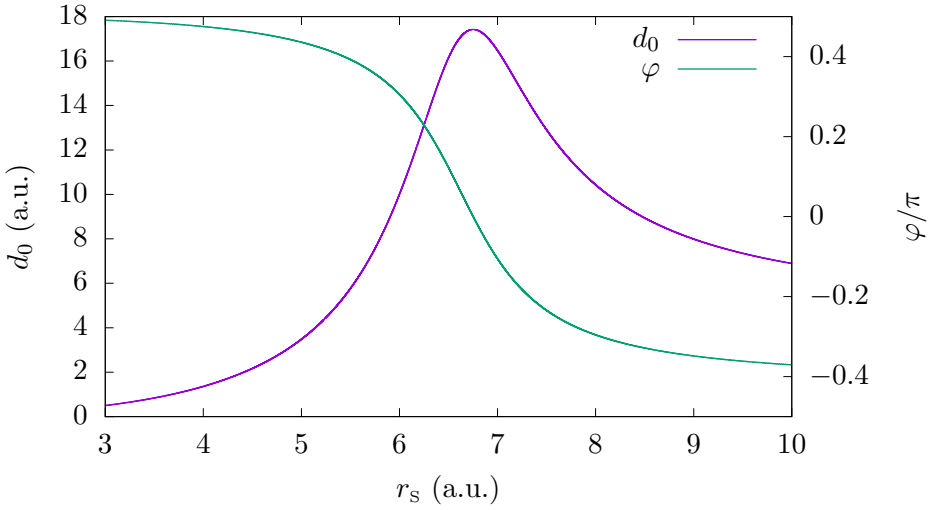

Figure 3.1.: The behavior of d_0 and φ from equation (3.5) as a solution of the EOM (3.1) for fixed field parameters E_0 and ω when varying the Wigner-Seitz radius r_S. For the parameters used in section 3.4 the system becomes resonant at $r_S \approx 6.75$.

For a slow driver, $\omega \ll \omega_{\text{Mie}}$, we find $\varphi = \pi/2$ and $|d_0| = E_0/\omega_{\text{Mie}}^2$, whereas for a very fast driver, $\omega \gg \omega_{\text{Mie}}$, the values are $\varphi = -\pi/2$ and $|d_0| = E_0/\omega^2 \to 0$. The behavior of d_0 and φ versus r_S is shown in figure 3.1. The asymmetry seen in the figure is due to the non-linear relation $r_S = \omega_{\text{Mie}}^{-2/3}$.

Having described the motion of the driven electron sphere we now need the combined electrostatic potential of electron and ion sphere. A homogeneously charged sphere has the potential

$$V_{\text{sphere}}^{\pm}(r) = \pm\frac{R^3}{r_S^3}\begin{cases} \frac{r^2}{2R^3} - \frac{3}{2R} & \text{for } r < R \\ -\frac{1}{r} & \text{for } r \geq R \end{cases} \tag{3.6}$$

with ± indicating the sign of the charge. The combined potential follows as

$$V_{\text{cluster}}(\boldsymbol{r}, t) = V^{+}_{\text{sphere}}(|\boldsymbol{r}|) + V^{-}_{\text{sphere}}(|\boldsymbol{r} - \boldsymbol{d}(t)|)\,. \tag{3.7}$$

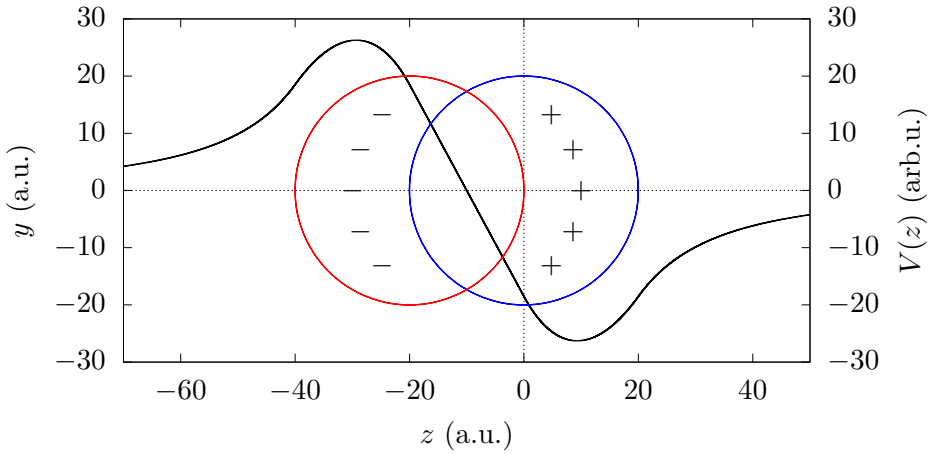

Figure 3.2.: Sketch of the RSM potential (3.7) with $d_z(t) = R$. The blue circle depicts the ion sphere, the red circle the displaced electron sphere. In black the potential $V_{\text{cluster}}(z, t)$ along the z-axis is shown.

Here we can plug in the analytical solution (3.5) from above. However, this result is only valid for the flat-top pulse (3.4), whereas we want to use finite pulses. For slowly varying pulse envelopes $E_0(t)$ this can nevertheless be used by replacing E_0 by $E_0(t)$ in the solution (3.5). It turns out that this approximation is sufficiently valid for our purpose.

Comparison with TD-DFT simulations To verify the validity of the RSM we conducted simulations within the framework of TD-DFT [45, 46] using the software package QPROP [47, 48] for the same parameters as in section 3.4. The simulation of sodium clusters within QPROP using the jellium model is described in [49]. Here we use an expanded neutral sodium cluster consisting of 20 atoms which is irradiated by a laser pulse as defined in section 3.4 below. Figure 3.3 shows the potential governing the motion of the electrons at different times. Since QPROP uses spherical harmonics as basis functions a multipole expansion is applied to the effective electron-electron interaction potential, where all terms beyond the quadrupole are neglected. The potentials plotted in figure 3.3 contain the background (jellium) potential, the interaction potential $-\boldsymbol{r} \cdot \boldsymbol{E}(t)$ with the laser and the electron-electron interaction potential up to the monopole, dipole or quadrupole term. For comparison the potential resulting from the RSM is added. As this comparison shall be on a qualitative level, the latter is scaled to match the density functional theory (DFT) potentials. The scaling depends on the damping factor γ which is a free parameter.

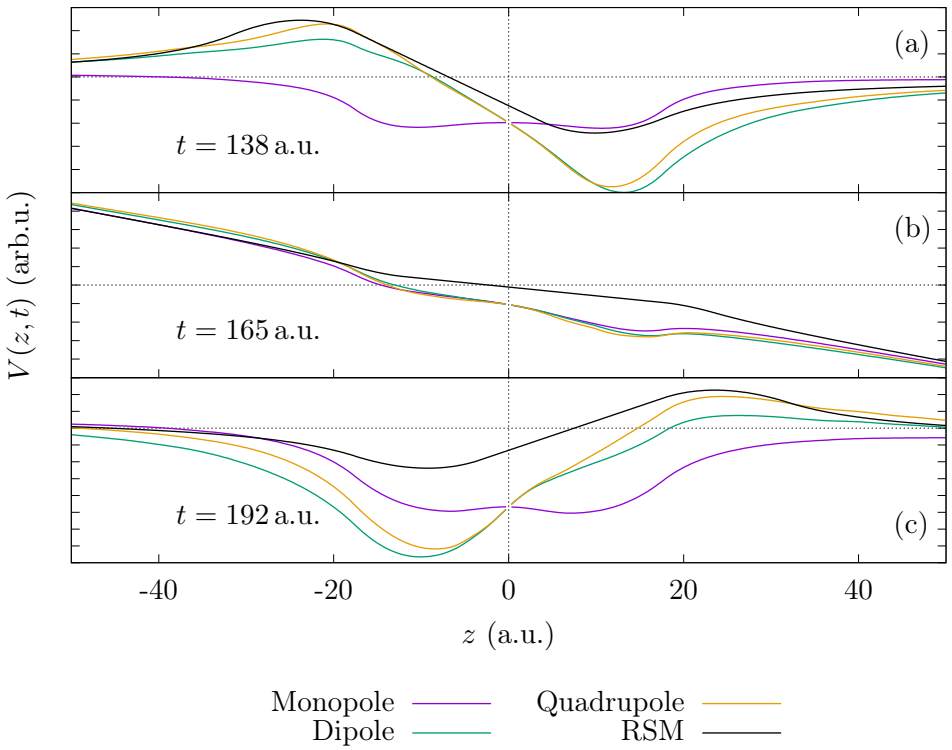

Figure 3.3.: Multipole potentials up to monopole, dipole or quadrupole from TD-DFT simulations for the parameters from section 3.4. (a) & (c) show the potentials for $E_z(t) \approx 0$ while (b) displays the maximum $E_z(t) \approx E_0$ in between. The RSM potential is added for comparison.

The three cases shown in figure 3.3 correspond to the laser field crossing zero twice and the maximum in between. We see that in all cases the RSM potential resembles the overall shape of the DFT potential quite well. The potential well in the center shown by the monopole is not reproduced. This is not surprising at all as it represents the binding potential of the cluster which is neglected in the RSM. We found that adding terms to reproduce this provides no further insight into the mechanism under consideration. The difference between the potentials up to dipole and quadrupole is rather small so that the dipole potential is sufficient to describe the situation and restricting the motion to one dimension is thus well justified.

3.3. Quantum Trajectories and External Potentials

The method we use to treat the problem introduced in section 3.1 is an extension of the trajectory-based SFA as presented in 2.2 and 2.3. The plain SFA cannot describe influences of external potentials on spectra as it uses Gordon-Volkov waves for the outgoing electrons which only include the laser field. However, the interpretation of (2.46) as a sum over trajectory contributions allows us to intuitively include corrections due to external potentials. In this section one possibility for such a correction is derived from the trajectory-based Coulomb-corrected strong field approximation (TCSFA) [22–25] where this approach was applied to the Coulomb potential. A different method to include corrections to the plain SFA (also for the Coulomb potential) is presented in chapter 4.

The matrix element (2.46) may be rewritten as

$$\begin{aligned} M_{\boldsymbol{p}_0}^{(\mathrm{SFA})} &= -2^{-1/2}(2I_\mathrm{p})^{5/4} \sum_s \frac{1}{S''_{\boldsymbol{p}_0,I_\mathrm{p}}(t_s)} \mathrm{e}^{\mathrm{i}\int_0^{t_s} \mathrm{d}t' \left(\frac{1}{2}\boldsymbol{v}_0^2(t')+I_\mathrm{p}\right)} \\ &= -2^{-1/2}(2I_\mathrm{p})^{5/4} C(\boldsymbol{p}_0) \sum_s \frac{1}{S''_{\boldsymbol{p}_0,I_\mathrm{p}}(t_s)} \mathrm{e}^{-\mathrm{i}\int_{t_s}^{t_d} \mathrm{d}t' \left(\frac{1}{2}\boldsymbol{v}_0^2(t')+I_\mathrm{p}\right)} \end{aligned} \tag{3.8}$$

where $C(\boldsymbol{p}_0) = \exp\left\{\mathrm{i}\int_0^{t_d} \mathrm{d}t \left(\frac{1}{2}\boldsymbol{v}_0^2(t) + I_\mathrm{p}\right)\right\}$ is a constant phase factor only depending on $\boldsymbol{p}_0$, $\boldsymbol{v}_0(t) = \boldsymbol{p}_0 + \boldsymbol{A}(t)$ is the velocity of the electron (which is equal to its kinetic momentum due to $m_\mathrm{e} = 1$ in atomic units) and $t_d \to \infty$ is the detection time. Here it is important to note that $\boldsymbol{p}_0$ is the canonical momentum in velocity gauge and $\boldsymbol{v}_0(t)$ is the kinetic momentum. However, since we work in length gauge here, this difference only amounts to a coordinate transformation which separates the drift momentum $\boldsymbol{p}_0$ from the laser-induced quiver momentum $\boldsymbol{A}(t)$. Notation-wise we use $\boldsymbol{v}$ for the velocity or kinetic momentum and $\boldsymbol{p}$ for the drift momentum.

Equation (3.8) is a sum over contributions from individual trajectories. Apart from the prefactor, these individual contributions consist of an integration over the kinetic energy $\frac{1}{2}\boldsymbol{v}_0^2(t)$ of the electron from the saddle-point time t_s (which can be termed ionization time as well) to the detector. Considering the origin of the integrand, the kinetic energy can also be written as a Hamiltonian[1],

$$\frac{1}{2}\boldsymbol{v}_0^2(t) = H_0(t)\,, \tag{3.9}$$

where the subscript "0" denotes the "uncorrected" nature of a variable. This Hamiltonian can now be corrected for any external potential $V(\boldsymbol{r}, t)$,

$$H(t) = \frac{1}{2}\boldsymbol{v}^2(t) + V(\boldsymbol{r}, t)\,. \tag{3.10}$$

[1] When, in contrast, considering the related method of path integrals, we have to use the Lagrangian instead. This is indeed done in appendix A.4 where a perturbative Coulomb correction is derived. There the difference between Hamiltonian and Lagrangian formulation is important due to the approximations made, as discussed in appendix B of [18]. Here the results are the same.

Note the missing subscript for the velocity. Changing the Hamiltonian by adding a potential also changes the trajectory of the electron, so that we have to replace the uncorrected velocity $\boldsymbol{v}_0(t) \to \boldsymbol{v}(t)$ by a corrected one. This applies to the position $\boldsymbol{r}_0(t) \to \boldsymbol{r}(t)$ as well. $\boldsymbol{r}(t)$, $\boldsymbol{v}(t)$ and $H(t)$ are connected via Hamiltonian mechanics which lead to Newtons EOM:

$$\dot{\boldsymbol{r}} = \boldsymbol{p}(t) + \boldsymbol{A}(t) \tag{3.11a}$$

$$\dot{\boldsymbol{p}} = -\boldsymbol{\nabla} V(\boldsymbol{r}, t)\,. \tag{3.11b}$$

Note that the drift momentum $\boldsymbol{p}(t)$ acquires time dependence here as well in contrast to the plain SFA where $\boldsymbol{p}_0$ is a constant of motion.

Regardless of the simplicity of this ansatz we have to face some issues that arise when trying to replace $H_0(t) \to H(t)$ in equation (3.8). First, $C(\boldsymbol{p}_0)$ contains $\boldsymbol{v}_0(t) = \boldsymbol{p}_0 + \boldsymbol{A}(t)$ where $\boldsymbol{p}_0$ has been a conserved quantity until now. Replacing $\boldsymbol{v}_0(t)$ by $\boldsymbol{v}(t) = \boldsymbol{p}(t) + \boldsymbol{A}(t)$ here as well invalidates the assumption that $C(\boldsymbol{p})$ stays constant as stated above. However, here we neglect this change by keeping $\boldsymbol{v}_0(t)$ in the integrand, as it was done in [24, 25]. Doing so, the integrand (and thus the whole integral) in $C(\boldsymbol{p}_0)$ stays purely real, and $C(\boldsymbol{p}_0)$ amounts only to a phase factor that cancels out when calculating the transition probability.

The other issue is the non-vanishing imaginary part of the lower limit t_s of the integration and the closely related problem of initial conditions for $\boldsymbol{r}(t)$. To achieve a better understanding for the situation we look at the detector at time t_d. There we want to measure the final drift momentum $\boldsymbol{p}(t_d) = \boldsymbol{v}(t_d)$ of the incoming electron. This must be real since it is an observable. On the other hand t_s is complex, and assuming for the moment $\boldsymbol{r}(t_s) = 0$, this leads via the EOM (3.11) to complex position and velocity for $t = t_s + \Delta t$ for small Δt, and there is no guarantee that $\boldsymbol{v}(t)$ will ever become real again. If, on the other hand, we can ensure that at some purely real time t' position $\boldsymbol{r}(t')$ and velocity $\boldsymbol{v}(t')$ are real as well, all variables will stay real for all times $t > t'$, which follows directly from the EOM (3.11). This goal can be achieved by splitting the time propagation in the exponent of equation (3.8) into two parts (dropping the indices $\boldsymbol{p}_0, I_\mathrm{p}$ for brevity),

$$S_0(t_d, t_s) = \int_{t_s}^{t_d} \mathrm{d}t' \left(\frac{1}{2}\boldsymbol{v}_0^2(t') + I_\mathrm{p}\right) \tag{3.12}$$

$$= \int_{t_s}^{\operatorname{Re} t_s} \mathrm{d}t' \left(\frac{1}{2}\boldsymbol{v}_0^2(t') + I_\mathrm{p}\right) + \int_{\operatorname{Re} t_s}^{t_d} \mathrm{d}t' \left(\frac{1}{2}\boldsymbol{v}_0^2(t') + I_\mathrm{p}\right)\,. \tag{3.13}$$

The integration path is visualized in figure 3.4.

The first part contains the purely imaginary propagation from complex t_s to the real time axis (termed "sub-barrier part"), the second part is the propagation from the "tunnel exit" (this term will be further discussed in section 4.4) at $\operatorname{Re} t_s$ to the detection time t_d. The sub-barrier part will not be corrected at all (see [50] for the possibility of sub-barrier Coulomb corrections). This has the advantage that without

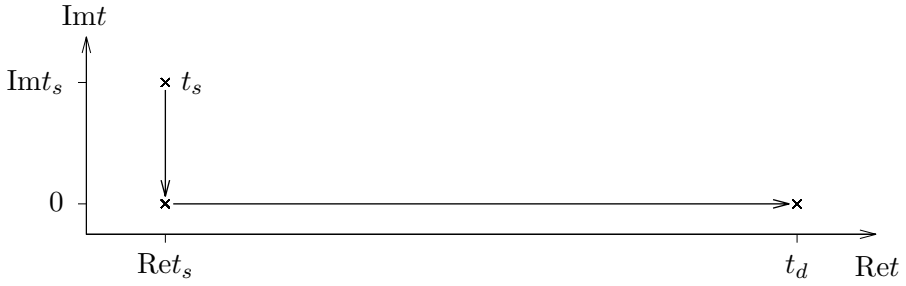

Figure 3.4.: Sketch of the integration path in the complex time plane from the ionization time t_s to the detection time t_d.

corrections the action and also the position $\boldsymbol{r}_0(t)$ can be evaluated analytically. As a consequence, $\boldsymbol{r}_0(t_s)$ can be chosen such that $\mathrm{Im}\,(\boldsymbol{r}_0(\mathrm{Re}\,t_s)) = 0$. The correction is applied to the second term which now becomes a purely real integral. The resulting action reads

$$S = S_0(\mathrm{Re}\,t_s, t_s) + S(t_d, \mathrm{Re}\,t_s) \tag{3.14}$$

$$S(t_d, \mathrm{Re}\,t_s) = \int_{\mathrm{Re}\,t_s}^{t_d} \mathrm{d}t' \left(\frac{1}{2}\boldsymbol{v}^2(t') + V(\boldsymbol{r}(t), t) + I_\mathrm{p}\right) . \tag{3.15}$$

The initial conditions for $\boldsymbol{r}_0(t)$ must be calculated from the EOM. Without external potential the latter is simply

$$\dot{\boldsymbol{r}}_0 = \boldsymbol{p}_0 + \boldsymbol{A}(t) \tag{3.16}$$

where $\boldsymbol{p}_0$ is the uncorrected drift momentum and thus constant. A single time integration leads to

$$\boldsymbol{r}_0(t) = \boldsymbol{p}_0\,(t - t_s) + \int_{t_s}^{t} \mathrm{d}t'\,\boldsymbol{A}(t') + \boldsymbol{r}_{0,\mathrm{ini}} \tag{3.17}$$

$$= \boldsymbol{p}_0\,(t - t_s) + \boldsymbol{\alpha}(t) - \boldsymbol{\alpha}(t_s) + \boldsymbol{r}_{0,\mathrm{ini}} \tag{3.18}$$

with the excursion $\boldsymbol{\alpha}(t)$ as in equation (2.62), see section 2.4. The condition for a real trajectory at the tunnel exit, $\mathrm{Im}\,(\boldsymbol{r}_0(\mathrm{Re}\,t_s)) = 0$, reads

$$\mathrm{Im}\,(\boldsymbol{r}_0(\mathrm{Re}\,t_s)) = \mathrm{Im}\,[\boldsymbol{p}_0\,(\mathrm{Re}\,t_s - t_s) + \boldsymbol{\alpha}(\mathrm{Re}\,t_s) - \boldsymbol{\alpha}(t_s) + \boldsymbol{r}_{0,\mathrm{ini}}] = 0 \tag{3.19}$$

$$\Rightarrow \mathrm{Im}\,\boldsymbol{r}_{0,\mathrm{ini}} = \boldsymbol{p}_0\,\mathrm{Im}\,t_s + \mathrm{Im}\,\boldsymbol{\alpha}(t_s) \tag{3.20}$$

where we used that $\mathrm{Im}\,\boldsymbol{p}_0 = 0$ and $\mathrm{Im}\,\boldsymbol{\alpha}(\mathrm{Re}\,t_s) = 0$. As we want the electron trajectory to start at the center, we set the real part $\mathrm{Re}\,\boldsymbol{r}_{0,\mathrm{ini}} = 0$. Using this we

can calculate the position of the electron at $t = \mathrm{Re}\, t_s$, i.e. the tunnel exit,

$$\begin{aligned} \boldsymbol{r}_0(\mathrm{Re}\, t_s) &= \boldsymbol{p}_0 \,(\mathrm{Re}\, t_s - t_s) + \boldsymbol{\alpha}(\mathrm{Re}\, t_s) - \boldsymbol{\alpha}(t_s) + \mathrm{i}\boldsymbol{p}_0 \,\mathrm{Im}\, t_s + \mathrm{i}\mathrm{Im}\, \boldsymbol{\alpha}(t_s) && (3.21) \\ &= \boldsymbol{\alpha}(\mathrm{Re}\, t_s) - \mathrm{Re}\, \boldsymbol{\alpha}(t_s)\,. && (3.22) \end{aligned}$$

Having found the proper initial condition for $\boldsymbol{r}$ at the tunnel exit we can calculate the action (3.14). The first term can, as already mentioned, be evaluated analytically,

$$\begin{aligned} S_0(\mathrm{Re}\, t_s, t_s) &= \int_{t_s}^{\mathrm{Re}\, t_s} \mathrm{d}t' \left(\frac{1}{2} \boldsymbol{v}_0^2(t') + I_\mathrm{p} \right) && (3.23) \\ &= \int_{t_s}^{\mathrm{Re}\, t_s} \mathrm{d}t' \left(\frac{1}{2} [\boldsymbol{p}_0 + \boldsymbol{A}(t')]^2 + I_\mathrm{p} \right) && (3.24) \\ &= \frac{1}{2} \boldsymbol{p}_0^2 \,(\mathrm{Re}\, t_s - t_s) + \boldsymbol{p}_0 \cdot (\boldsymbol{\alpha}(\mathrm{Re}\, t_s) - \boldsymbol{\alpha}(t_s)) \\ &\quad + \frac{1}{2} (\alpha^{(2)}(\mathrm{Re}\, t_s) - \alpha^{(2)}(t_s)) + I_\mathrm{p}(\mathrm{Re}\, t_s - t_s)\,, && (3.25) \end{aligned}$$

where we defined $\boldsymbol{\alpha}(t)$ as above and $\alpha^{(2)}(t)$ as

$$\alpha^{(2)}(t) = \int^t \mathrm{d}t' \, \boldsymbol{A}(t')^2\,. \tag{3.26}$$

Both $\boldsymbol{\alpha}(t)$ and $\alpha^{(2)}(t)$ are in most cases known analytically and thus easily calculated.

The second term in equation (3.14) contains the real-time propagation of the electron from the tunnel exit to the detector. Setting the initial conditions for the trajectory $\boldsymbol{r}(\mathrm{Re}\, t_s) = \boldsymbol{r}_0(\mathrm{Re}\, t_s)$ and $\boldsymbol{v}(\mathrm{Re}\, t_s) = \boldsymbol{p}_0 + \boldsymbol{A}(\mathrm{Re}\, t_s)$ allows us to perform a numerical propagation of $\boldsymbol{r}(t)$ and $\boldsymbol{v}(t)$ according to the EOM (3.11). $S(t_d, \mathrm{Re}\, t_s)$ is evaluated along that trajectory.

The denominator in the matrix element (3.8) is the second time derivative of the action. In accordance with the preceding derivations the uncorrected action S_0 is used here. This results in

$$\begin{aligned} S_0''(t) &= \frac{\mathrm{d}^2}{\mathrm{d}t^2} \int^t \mathrm{d}t' \left(\frac{1}{2} \boldsymbol{v}_0^2(t') + I_\mathrm{p} \right) \\ &= \frac{\mathrm{d}}{\mathrm{d}t} \left(\frac{1}{2} \boldsymbol{v}_0^2(t) + I_\mathrm{p} \right) \\ &= -\boldsymbol{E}(t) \cdot (\boldsymbol{p}_0 + \boldsymbol{A}(t)) && (3.27) \end{aligned}$$

where $\boldsymbol{E}(t) = -\frac{\mathrm{d}}{\mathrm{d}t} \boldsymbol{A}(t)$ was used. Dropping the phase factor $C(\boldsymbol{p}_0)$ the equation for

the transition matrix element for a single trajectory now reads

$$M_{\boldsymbol{p}_0}(t_s) = -\frac{(2I_\mathrm{p})^{5/4}}{\sqrt{2}} \frac{\exp\left\{-\mathrm{i}(S_0(\mathrm{Re}\, t_s, t_s) + S(t_d, \mathrm{Re}\, t_s))\right\}}{-\boldsymbol{E}(t_s)\cdot(\boldsymbol{p}_0 + \boldsymbol{A}(t_s))}\,. \tag{3.28}$$

Numerical Implementation Equation (3.28) describes the transition from a hydrogenic ground state to a continuum state with asymptotic momentum at the detector $\boldsymbol{p}(t_d \to \infty) = \boldsymbol{p}_\infty$. Due to the numerical propagation[2] this significantly differs from the initial drift momentum $\boldsymbol{p}_0$. However, $\boldsymbol{p}_\infty$ is the point in momentum space where a trajectory contributes to the PES. This has considerable consequences for the numerical implementation. In the plain SFA the matrix element (3.8) contains a simple summation over saddle-point times found numerically[3] from (2.44) to find the contribution to the spectrum at momentum $\boldsymbol{p}_0$. On the contrary, here the summation needs to run over all trajectories with the same asymptotic momentum $\boldsymbol{p}_\infty$. As the relation between $\boldsymbol{p}_0$ and $\boldsymbol{p}_\infty$ is unknown, we need to calculate many trajectories for different $\boldsymbol{p}_0$ and gather their contributions $M_{\boldsymbol{p}_0}(t_s)$ on a momentum grid $\boldsymbol{p}_n$, Δp according to their individual $\boldsymbol{p}_\infty$ in the fashion of

$$M(\boldsymbol{p}_n) = \sum_{|\boldsymbol{p}_\infty - \boldsymbol{p}_n| < \Delta p} M_{\boldsymbol{p}_0}(t_s)\,, \tag{3.29}$$

details can be found in the appendix B.2. As a result, the resolution of the spectra depends on the number of trajectories, which leads to diverging numerical effort. Therefore it is useful to select only the most relevant solutions of (2.44) as described in section 2.3. This is applicable here as well since the sub-barrier part, which fully determines the weight of a trajectory, is not modified.

The actual numerical calculation of the asymptotic momentum and action depends on the range of the potential $V(\boldsymbol{r}, t)$. Obviously a numerical propagation is limited to finite times $t_{d,\mathrm{finite}}$. For short-range potentials (as from section 3.2) it is sufficient to choose the upper integration limit $t_{d,\mathrm{finite}}$ large enough to allow the electrons to leave the range of the potential after the laser is off. In that case $\boldsymbol{p}_\infty = \boldsymbol{p}(t_{d,\mathrm{finite}})$. The remaining action $S(\infty, t_{d,\mathrm{finite}})$ can then be calculated analytically. The usually divergent upper limit can be neglected as a constant phase factor as it is the same for every trajectory with the same $\boldsymbol{p}_\infty$. For long-range potentials this is more complicated as $\boldsymbol{p}(t)$ changes even for large distances. For the Coulomb potential this problem can be solved using Kepler's equations (see appendix B.1 for details).

[2] The EOM (3.11) are solved with an adaptive-step Runge-Kutta solver based on the algorithm RK5(4)7M from [51].

[3] The saddle-point equation (SPE) (2.44) is solved using the ACM TOMS algorithm 365 [52].

3.4. Photoelectron Momentum Spectra

The method presented in section 3.3 is applied using the potential from section 3.2 to numerically obtain PES for ionization from laser-driven metal clusters. Below details about the implementation are given and resulting spectra are shown.

First we need to review the setup described in [38] that is to be modeled. There neutral metal clusters consisting of several hundred atoms are irradiated with pairs of laser pulses (pump and probe) with a wavelength of $\lambda = 800\,\mathrm{nm}$ and intensities around $I = 10^{13}\,\mathrm{W/cm^2}$, pulse duration of $T_p = 100\,\mathrm{fs}$ each and adjustable time delay Δt between the pulses. The kinetic energy distribution of the emitted electrons is measured.

As already mentioned we do not directly simulate the expansion of the cluster due to the pump pulse. Instead we mimic an expanded cluster by changing the size of the cluster while leaving the atom number constant, i.e., we change the Wigner-Seitz radius r_s used in the RSM. This modifies the resonance frequency of the oscillation (see section 3.2 and especially figure 3.1) and thus the interaction between cluster and laser pulse. The probe pulse is represented by a vector potential of the form

$$\boldsymbol{A}(t) = \boldsymbol{e}_z A_0 \sin^2(\Omega t)\sin(\omega t) = \boldsymbol{e}_z A_z(t) \tag{3.30}$$

for $0 < \Omega t < \pi$ and zero otherwise. Here $\Omega = \omega/(2n_c)$ is the envelope frequency, n_c the number of optical cycles under the envelope and $A_0 = -E_0/\omega$ the amplitude of the vector potential. The laser frequency $\omega = 0.057$, the number of cycles $n_c = 3$ and the electric field amplitude $E_0 = 0.01688$ are chosen to match the experimental values stated above. The only remaining free parameter in the RSM is the damping factor $\gamma = 0.017$. Here it is chosen such that for the mentioned laser parameters electron and ion sphere always overlap[4]. The cluster we use in our simulations consists of 20 sodium atoms (Na_{20}) with one valence electron each. This is significantly smaller than in the experiment, nevertheless qualitatively the same effects are observed as demonstrated below. The initial electronic state enters in equation (3.28) as a pre-exponential factor. As a full description of the valence band of a sodium cluster is not within the scope of this work, we have to find a suitable approximation for that state. Besides the hydrogenic ground state used in section 2.3 we tried a Gaussian wave function of width $\sim R$ and a short-range δ-potential like state. We found that the qualitative structure of the resulting spectra is not affected by that choice. In particular, the cutoffs we want to observe are determined by the action, not by the prefactor. In the following we show results using the hydrogenic ground state. The only property of the ground state that enters the action is the ionization potential I_p. This is set to the experimental value of $I_\mathrm{p} = 0.14$ for the ground state of Na_{20} [53]. Changes of the ionization potential due to the expansion of the cluster are neglected. Another ingredient for the calculation of the action is the tunnel exit

[4] Within this restriction we deliberately minimized the strength of the damping to maximize the effect of the collective potential. This does not lead to qualitative changes but solely increases the visibility of the effects under investigation.

$\boldsymbol{r}(\mathrm{Re}\, t_s)$ that enters via the electron trajectory. For the potential from the RSM this has to be modified to ensure that the electron appears *outside* the cluster after tunneling. To that end, the atomic tunnel exit $\boldsymbol{r}(\mathrm{Re}\, t_s)$ calculated from equation (3.22) is shifted outwards by three times the cluster radius R from equation (3.2). For the linearly polarized laser field defined by equation (3.30) this means

$$z'(\mathrm{Re}\, t_s) = z(\mathrm{Re}\, t_s) + 3R\frac{z(\mathrm{Re}\, t_s)}{|z(\mathrm{Re}\, t_s)|} \tag{3.31}$$

with $\boldsymbol{r}(\mathrm{Re}\, t_s) = \boldsymbol{e}_z z(\mathrm{Re}\, t_s)$. This procedure seems rather *ad hoc*. However, the features seen in the PES prove to be robust with respect to changes in this shift. The boundary conditions are that (i) the electron must start outside the cluster, i.e., $|z'(\mathrm{Re}\, t_s)| > |d_z(\mathrm{Re}\, t_s) + R|$, and (ii) the laser is still on while the electron passes the cluster. The reason for this robustness is that the acceleration mechanism (as seen in section 3.5 below) is not very sensitive to the emission time. If for one emission time t_s and corresponding momentum $\boldsymbol{p}_0$ the electron is not accelerated due to the shift of $z(\mathrm{Re}\, t_s)$, another pair of $\boldsymbol{p}_0'$ and t_s' exists for which it does get accelerated, within the limits mentioned above.

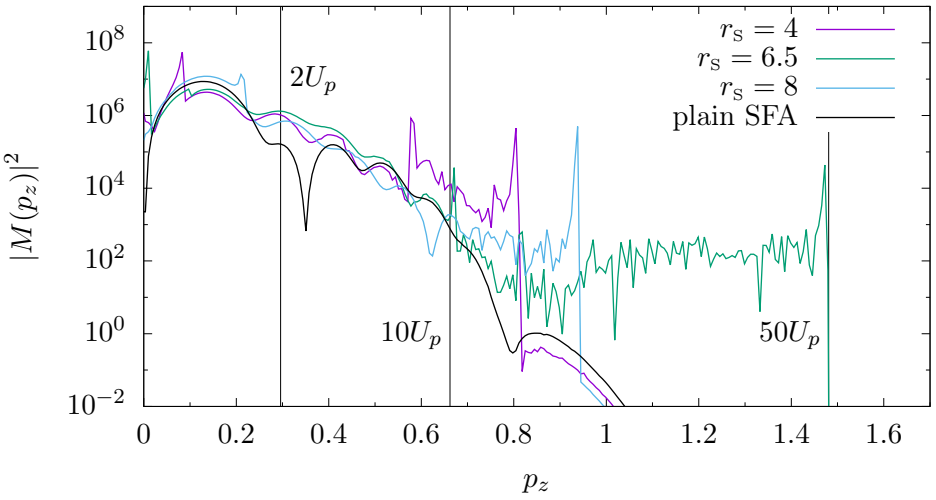

Figure 3.5.: Momentum-resolved photoelectron spectra from Na_{20} clusters for different expansions. For comparison a plain SFA spectrum is shown in black. The resonance condition is reached at $r_S \approx 6.5$. For $r_S = 4$ (value for bulk sodium, no expansion) the Mie frequency is larger than the laser frequency, for $r_S = 8$ it is smaller. The laser parameters are $\omega = 0.057$, $n_c = 3$ and $E_0 = 0.01688$. Only positive momenta are shown due to symmetry reasons.

For the calculation of PES we evaluate equation (3.28) as described in section 3.3. PES for different expansions (different Wigner-Seitz radii r_S) of the cluster are shown in figure 3.5. For $N_{\boldsymbol{p}_0} = 2 \times 10^5$ momenta in the range $\boldsymbol{p}_0 = [-2, 2]$ we use the four

most relevant saddle-point solutions per momentum. For comparison a plain SFA spectrum is included as well. The feature we want to analyze is the maximum photoelectron momentum $p_{\max}$ in polarization direction (or the corresponding kinetic energy $E_{\mathrm{kin,max}}$) before the sharp drop in the yield $|M(p_z)|^2$, and its dependence on the cluster expansion. Only positive momenta are considered as the situation is similar in the opposite direction (although the obtained cutoff energies are different). As mentioned in section 3.1 the expected maximum kinetic energy is $2U_\mathrm{p}$ for directly emitted electrons or $10U_\mathrm{p}$ when considering a single rescattering event. These values follow directly from the simple man's theory (SMT) as presented in section 2.4. The spectra for $r_\mathrm{S} = 4$ (value of bulk sodium, no expansion) and $r_\mathrm{S} = 8$ show only moderate enhancement of $p_{\max}$ with respect to the plain SFA spectrum. For $r_\mathrm{S} = 6.5$ the kinetic energy reaches $50U_\mathrm{p}$ which is far beyond the expected values[5]. Obviously the maximum kinetic energy behaves non-monotonously with the expansion. This is consistent with the oscillation of the background electron cloud as described by the RSM where the peak oscillation amplitude is reached at $r_\mathrm{S}^{(\mathrm{RSM})} = 6.75$. This indicates that the observed behavior is a resonance effect.

3.5. Trajectory Analysis of the Acceleration Mechanism

The beauty of the SFA in saddle-point approximation (SPA) lies in the possibility to analyze spectral features in terms of electron trajectories. This is preserved when adding external potentials as done above. It is used here to identify the mechanism leading to the features shown in section 3.4.

We focus on the resonance case for $r_\mathrm{S} = 6.5$ as seen in figure 3.5. To analyze the mechanism which accelerates the electrons we first need to find the electron trajectories contributing most in the high energy part of the spectrum. To that end we gather all trajectories with final momentum $\boldsymbol{p}_\infty \cdot \boldsymbol{e}_z = p_\infty > 0.8$ in polarization direction on a grid for $\mathrm{Re}\, t_s$ and incoherently[6] sum up the inidiviual contributions $|M_{\boldsymbol{p}_0}(t_s)|^2$ from equation (3.28) within time bins of width $\Delta t = 2$. The resulting distribution is shown in figure 3.6 where the vector potential $A_z(\mathrm{Re}\, t_s)$ is added as a reference frame.

It shows that most of the trajectories contributing to the high energy part of the spectrum are emitted within a very short time window, $120 < \mathrm{Re}\, t_s < 130$. That means the mechanism considered here applies to trajectories with specific initial conditions only. From the emission time and the vector potential one can deduce that these are long trajectories, which means that plain SFA trajectories with the same initial conditions pass the center at least once before reaching the detector (see section 2.4 for details).

[5] Although this number has to be regarded with care as the magnitude of the effect depends on the damping factor γ which was chosen arbitrarily. However, the quality of the effect remains unaffected.

[6] The summation must be performed incoherently to exclude any artificial interference between trajectories with different momenta.

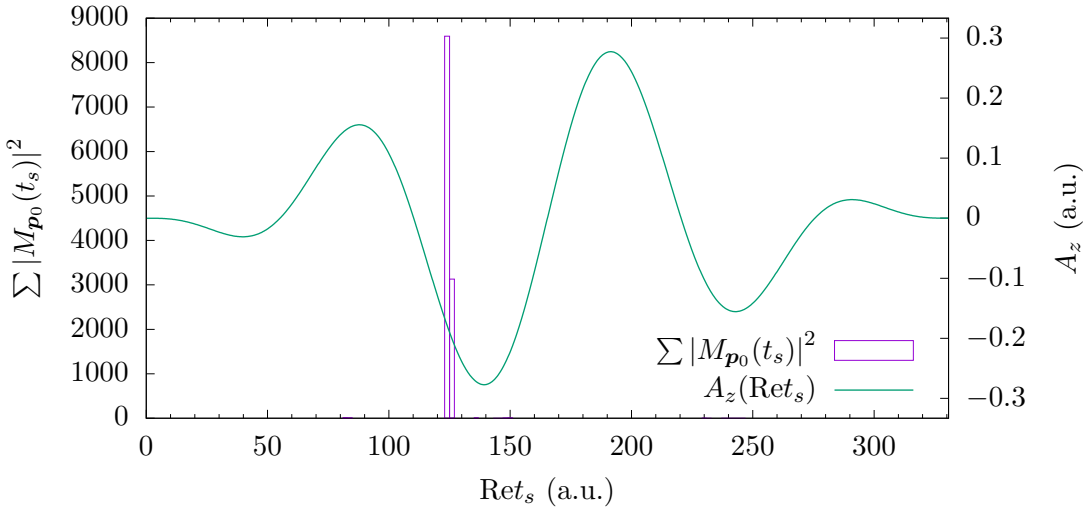

Figure 3.6.: Incoherent sum over the individual trajectory contributions $|M_{\boldsymbol{p}_0}(t_s)|^2$ for trajectories with final momenta $p_\infty > 0.8$ gathered in bins of similar initial times $\mathrm{Re}\, t_s$. The vector potential $A_z(\mathrm{Re}\, t_s)$ is added to guide the eye.

This is illustrated in figure 3.7 where the trajectories selected in figure 3.6 are plotted as position $z(t)$ versus real time. Due to the large number of propagated trajectories only a small fraction is shown for clarity. A part of these indeed crosses the cluster center. Other trajectories are reflected from the boundary and leave in opposite direction. This is one example for the sometimes chaotic relation between the initial momentum $\boldsymbol{p}_0$ and the final momentum $\boldsymbol{p}_\infty$ (the consequences of which are outlined in appendix B.2). When additionally the momentum is restricted to $p_\infty > 0.8$ (figure 3.7, green lines) we see that all corresponding trajectories cross the cluster once in a narrow time window. The cluster boundaries indicate that within this time window the electron sphere is significantly displaced with respect to the ion sphere. As depicted in figure 3.2 this results in a very steep potential inside the cluster which in turn accelerates the crossing electrons.

This acceleration can be observed in detail when plotting momentum as a function of time for the respective trajectories as done in figure 3.8. There the final momentum is restricted to $p_\infty > 1.2$ for clarity. Note that the drift momentum $p_z(t)$ (violet) is shown, not the kinetic momentum $v_z(t) = p_z(t) + A_z(t)$. As seen from the EOM (3.11) any change in the drift momentum is a direct consequence of the external potential. The most prominent feature of $p_z(t)$ shown here is a strong increase around the time the trajectories cross the cluster center (see figure 3.7). The reason for this acceleration becomes clear when looking at the total force $F_{z,\mathrm{total}}(t) = \frac{\mathrm{d}}{\mathrm{d}t} v_z(t) = -\frac{\mathrm{d}}{\mathrm{d}z} V(z,t) - E_z(t)$ on the electrons (figure 3.8, green lines). This strongly deviates from the force exerted by the laser $F_{z,\mathrm{laser}} = -E_z(t)$ (shown in black) within the same time window. The kinks in the total force are

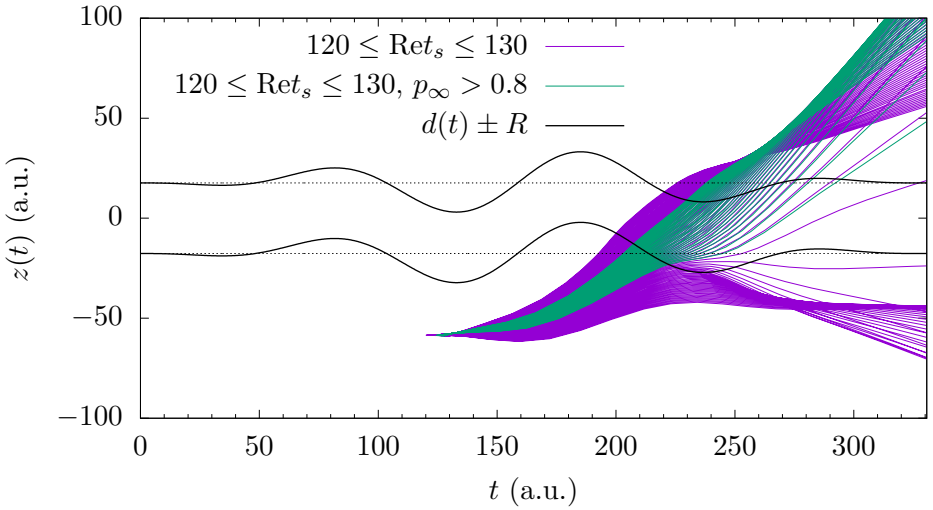

Figure 3.7.: Trajectories $z(t)$ (violet lines) emitted within the time window found in figure 3.6. Black (dotted) lines denote the boundaries of the electron (ion) sphere, green lines show trajectories with large final momenta, $p_\infty > 0.8$.

caused by the structure of the cluster potential (3.7) which is defined piecewise. As a consequence the force as the spatial derivative of the potential is continuous but not continuously differentiable. This could be lifted by modifying the RSM towards spheres with smooth boundaries, but the qualitative behavior of the trajectories would not change.

The positive force observed in figure 3.8 leads to an increase of $p_z(t)$ for the selected trajectories and thus to final momenta much larger than predicted by the plain SFA. This has fundamental consequences for the PES as shown in figure 3.5. Remember that the weight of a single trajectory is determined at the tunnel exit. Following the approximations made in the SMT (section 2.4) we know that smaller momenta correspond to larger weight. Thus we arrive at the following interpretation: the trajectories discussed above are refocused and thus shift their weight from the low-energy part of the spectrum to higher energies, that way generating an extended plateau in the spectrum.

Another observation made in figure 3.8 is that the momenta of the selected trajectories do not exceed a certain peak momentum where an accumulation of trajectories can be noticed. This leads to a distinct peak at the cutoff momentum in the PES shown in figure 3.5. Such caustics are known to appear in semi-classical descriptions of quantum dynamics. In full quantum calculations these are usually smoothed out, however, in some cases they are still observable [24].

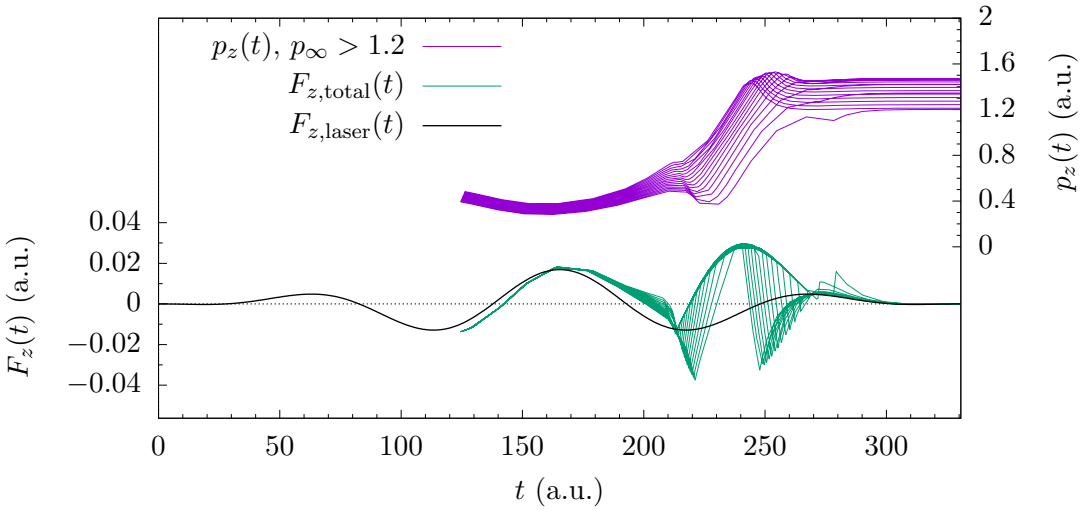

Figure 3.8.: Trajectories emitted within the time window found in figure 3.6 and with final momenta $p_\infty > 1.2$. The drift momentum $p_z(t)$ is shown in violet. Additionally the total force (green) acting along the selected trajectories and the contribution of the laser field (black) to the total force is shown.

3.6. Conclusions

In this chapter we applied the concept of the trajectory-based SFA to metal clusters where the collective field of the bound valence electrons significantly alters the motion of emitted electrons. To that end we combined the ideas of the TCSFA as used in [24, 25] with the RSM to include the collective field of the cluster. We showed that this approach is capable of explaining the emission of high energy electrons from laser-irradiated metal clusters close to resonance. Thanks to the formulation in terms of quantum trajectories we could analyze the mechanism leading to this phenomenon. We found that some of the so-called long trajectories revisiting the cluster interior within a certain time window can be significantly accelerated by the collective field. This effect depends on the oscillation of the valence electrons with respect to the ion sphere and is therefore strongest at resonance.

One consequence of the trajectory analysis performed in this chapter is that the spectral phenomenon under consideration should also be accessible to purely classical methods as it only relies on the momentum shift of the electrons. However, in comparison to classical simulations our method has the advantage that it allows for interference. This is essential for effects like above-threshold ionization peaks and holographic side-lobes [54], or for structural analysis where information about the internal structure is reconstructed from interference patterns [55].

4. Enhanced Direct Photoelectron Emission at High Energies

4.1. Motivation

The strong field approximation (SFA) [11–13] is the work horse of theoretical strong-field physics due to its high predictive power and the additional insight it provides thanks to its formulation in terms of quantum orbits [17, 18, 56, 57]. However, neglecting the Coulomb potential after the ionization event leads to several effects not covered by the plain SFA, especially in the low-energy regime. Here the low [1–3], very low [4, 5] and zero energy [6, 7] structures were found which exhibit surprisingly high yield at particular final electron momenta. These structures originate from soft laser-driven recollisions [3, 58] with the parent ion. Their positions in momentum space are encoded in the SFA when including the rescattering matrix element [59, 60] but do not exhibit increased probabilities.

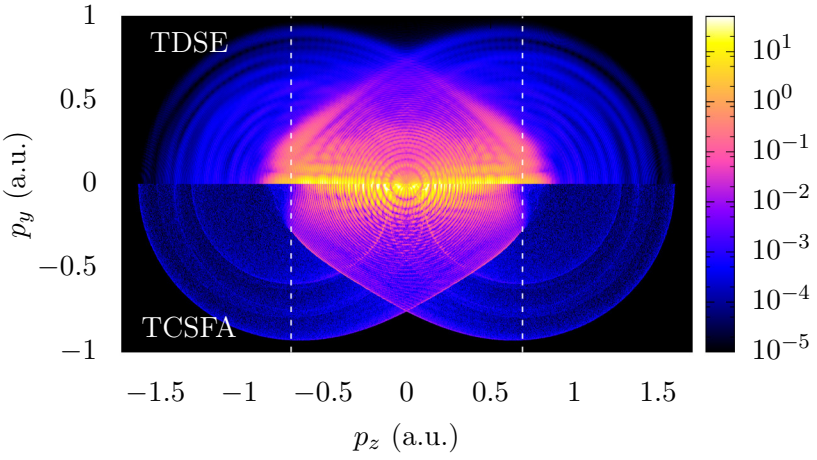

Figure 4.1.: Comparison of momentum-resolved PES from TDSE and TCSFA for the same $I_\mathrm{p} = 0.14$ (3.8 eV) and laser parameters as in Ref. [54], i.e., $\omega = 0.0065$ (7 microns), $E_0 = 0.0045$ ($I = 7.1 \times 10^{11}\,\mathrm{W/cm^2}$), $\alpha_\mathrm{C} \simeq 12.4$ (see section 4.2, with asymptotic charge $Z = 1$), $\alpha_\mathrm{L} \simeq 8.6$, using a six-cycle $\sin^2$-shaped pulse envelope, linear polarization in z direction and the effective potential from equation (4.9). The $2U_\mathrm{p}$ cutoff positions are indicated by white dashed lines.

Here we examine another energy regime where the so-called "$2U_\mathrm{p}$ cutoff" is lo-

cated. U_p is the ponderomotive energy, i.e. the kinetic energy of a free electron oscillating in a laser field, averaged over one optical cycle. The cutoff energy of $2U_\mathrm{p}$ is predicted by the simple man's theory (SMT) (see section 2.4) as the maximum kinetic energy for electrons emitted directly (without rescattering events) upon photoionization. Following the SMT and using tunneling rate formulas [16] these electrons would acquire zero weight. On the other hand, photoelectron spectra (PES) obtained from the plain SFA, apart from the well understood intra- and intercycle interference patterns, just roll off featureless, exhibiting no sign of a $2U_\mathrm{p}$ cutoff at all. However, spectra obtained as numerical solutions of the time-dependent Schrödinger equation (TDSE) clearly show enhanced yield around that energy for certain parameters as shown in section 4.2. A prominent example can be seen in [54] where experimental data is shown in comparison to TDSE and Coulomb-corrected SFA simulations. In figure 4.1 we show the result from a TDSE calculation obtained from QPROP [47, 48, 61] compared to a simulation using the trajectory-based Coulomb-corrected strong field approximation (TCSFA) [22–25, 39] with the parameters from [54]. The direct cutoff on the polarization axis ($p_y = 0$) is expected at a momentum of $|p_z| \approx 0.7$ as indicated. The TDSE spectrum shows a plateau which starts to drop significantly just after the cutoff momentum, whereas the TCSFA spectrum decreases much earlier. This becomes even more visible in figure 4.2 where TDSE and plain SFA PES in polarization direction are compared, demonstrating significant differences around the cutoff momentum.

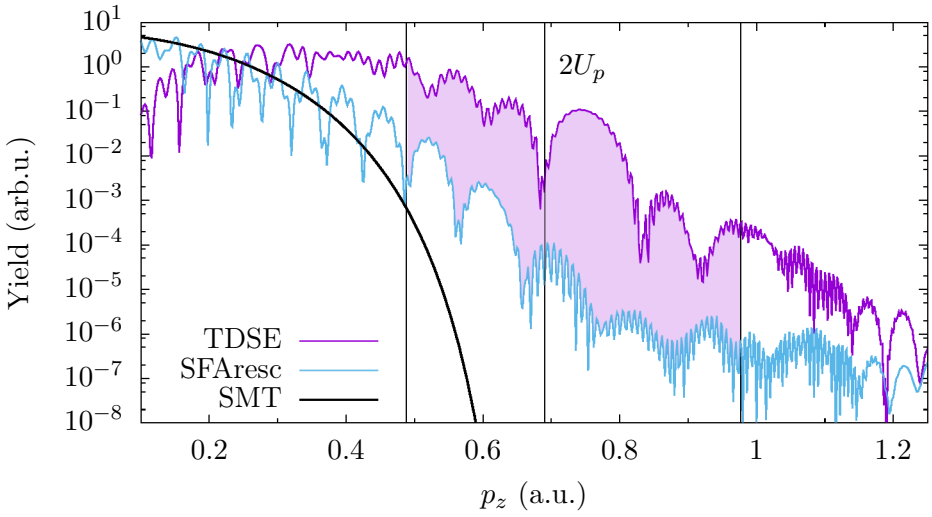

Figure 4.2.: TDSE spectra around the $2U_\mathrm{p}$ cutoff compared to the plain SFA including rescattering (SFAresc) calculated from equations (2.27) and (2.33), same parameters as in figure 4.1. The shaded area between TDSE and SFA spectrum highlights the order-of-magnitude discrepancy. Vertical lines indicate 1, 2, and $4U_\mathrm{p}$. The SMT prediction for direct emission is plotted bold black.

The corresponding TCSFA spectrum is not shown as it qualitatively follows the plain SFA one. The SMT prediction added in black deviates even more from the TDSE result as it approaches zero at the cutoff. How the observed enhancement in the yield depends on the laser and target parameters and how this effect can be incorporated into the SFA will be shown in this chapter. The main results have already been published in [62] but are presented here in more detail.

4.2. Scaling the Time-Dependent Schrödinger Equation

The theory of reference on which we gauge the validity of the SFA is the TDSE, which is considered exact in this regime[1]. To study the parameter dependence of spectral features it is therefore useful to analyze the scaling behavior of the TDSE. Assuming an electron in a linearly polarized laser field

$$\boldsymbol{E}(t) = \boldsymbol{e}_z E_0 f(t) \sin(\omega t) \tag{4.1}$$

with $0 \leq f(t) \leq 1$ being a dimensionless envelope function the TDSE in SI units reads

$$\mathrm{i}\hbar \frac{\mathrm{d}}{\mathrm{d}t}\Psi(\boldsymbol{r},t) = \left[-\frac{\hbar^2}{2m_\mathrm{e}}\Delta_{\boldsymbol{r}} - \frac{eZ}{4\pi\varepsilon_0 r} + \boldsymbol{r}\cdot\boldsymbol{e}_z\, eE_0 f(t)\sin(\omega t)\right]\Psi(\boldsymbol{r},t) \tag{4.2}$$

where we purposefully dropped atomic units to allow for unambiguous dimensional analysis. This equation can be expressed in dimensionless time and position,

$$\tau = \omega t \tag{4.3}$$

$$\bar{\boldsymbol{r}} = \sqrt{\frac{m_\mathrm{e}\omega}{\hbar}}\boldsymbol{r}\,, \tag{4.4}$$

leading to

$$\mathrm{i}\frac{\mathrm{d}}{\mathrm{d}\tau}\Psi(\bar{\boldsymbol{r}},\tau) = \left[-\frac{1}{2}\Delta_{\bar{\boldsymbol{r}}} - \sqrt{\frac{m_\mathrm{e}}{\hbar^3\omega}}\frac{e^2}{4\pi\varepsilon_0}\frac{Z}{\bar{r}} + \frac{eE_0}{\sqrt{m_\mathrm{e}\hbar\omega^3}}\bar{\boldsymbol{r}}\cdot\boldsymbol{e}_z\, f(t)\sin(\tau)\right]\Psi(\bar{\boldsymbol{r}},\tau)\,. \tag{4.5}$$

The scaling is chosen such that the left-hand side and the kinetic energy term on the right-hand side keep their form, i.e., do not acquire extra prefactors. The conversion to atomic units simplifies above equation to

$$\mathrm{i}\frac{\mathrm{d}}{\mathrm{d}\tau}\Psi(\bar{\boldsymbol{r}},\tau) = \left[-\frac{1}{2}\Delta_{\bar{\boldsymbol{r}}} - \frac{Z}{\sqrt{\omega}\bar{r}} + \frac{E_0}{\omega^{3/2}}\bar{z}\, f(t)\sin(\tau)\right]\Psi(\bar{\boldsymbol{r}},\tau) \tag{4.6}$$

[1] Apart from the dipole approximation, which has only minor effects in this regime, see chapter 5, and higher order relativistic effects, which are negligible here. For many-electron atoms additionally the single active electron (SAE) approximation is applied, which is valid to sufficiently high accuracy in all cases considered here.

with $\bar{z} = \bar{\boldsymbol{r}} \cdot \boldsymbol{e}_z$. Consequently the Coulomb potential scales with $\alpha_C = Z/\sqrt{\omega}$ and the laser field with $\alpha_L = E_0/\omega^{3/2} = \sqrt{z_F}$ where $z_F = \frac{e^2 E_0^2}{m_e \hbar \omega^3}$ (in SI units) is the strong-field parameter [13]. For hydrogen-like ions a simple relation is found. Using $I_\mathrm{p} = Z^2/(2n^2)$ the ratio between the two scaling parameters yields

$$\alpha_C/\alpha_L = n\sqrt{I_\mathrm{p}/(2U_\mathrm{p})} \tag{4.7}$$

$$= n\gamma \tag{4.8}$$

with the principal quantum number n and the Keldysh parameter γ [11].

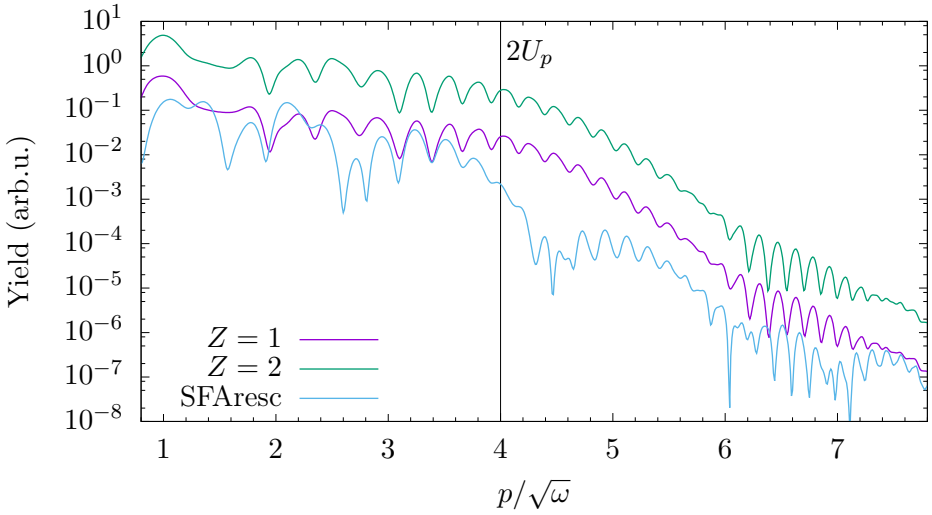

Figure 4.3.: Two TDSE PES versus dimensionless momentum, both for the ground state as initial state and with $\alpha_\mathrm{C} = \alpha_\mathrm{L} = 4$, but one for $Z = 1$, $\omega = 0.0625$, $E_0 = 0.0625$ (violet) and the other for $Z = 2$, $\omega = 0.25$, $E_0 = 0.5$ (green, shifted for better comparison). The SFA result is included (blue).

The validity of this scaling is demonstrated in figure 4.3 where two spectra from a hydrogen-like target are shown for $n = 1$ and $\alpha_C = \alpha_L = 4$ and thus $\alpha_C/\alpha_L = 1$ but different laser and target parameters, see figure caption. The spectra are obtained from numerically solving the TDSE using QProp [47, 48, 61], and shifted vertically for better comparison. They are identical within the accuracy of the simulation. The SFA spectrum was obtained by direct numerical evaluation of equations (2.27) and (2.33), the results of which are added up coherently. It is known that the SFA depends only on two dimensionless parameters, e.g., any pair of the set z_F, γ, the reduced electric field $F = E_0/(2I_\mathrm{p})^{3/2}$ and the multiquantum parameter $K_0 = I_\mathrm{p}/\omega$. Accordingly in figure 4.3 only one SFA spectrum is shown as the other one is identical. It shows a pronounced intracycle interference pattern which is responsible for a strong disagreement slightly above the momentum corresponding to $2U_\mathrm{p}$. However, apart from that the overall slope matches quite well. The agreement

becomes even better when increasing the laser parameter to $\alpha_L = 6$ ($\alpha_C/\alpha_L = 0.67$) which is shown in figure 4.4. Here both TDSE and SFA spectrum show a plateau-like feature up to $2U_\mathrm{p}$. Again the disagreement comes from the intracycle overemphasized interference pattern in the SFA.

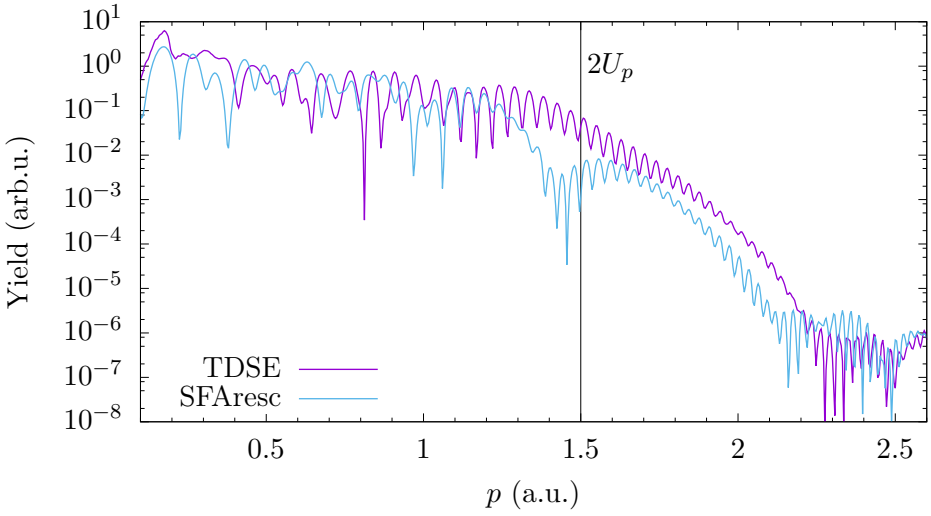

Figure 4.4.: TDSE and SFA PES in good agreement for H(1s) as in figure 4.3 but for $\alpha_\mathrm{L} = 6$ ($\omega = 0.0625$, $E_0 = 0.09375$).

The situation is different when considering targets which are not hydrogen-like or prepared in an excited state. The former are usually many-electron targets which are often simulated within SAE approximation with an effective potential to obtain the desired ionization potential I_p and asymptotic charge Z. Here we use an effective potential of the form

$$V_\mathrm{eff}(r) = -\frac{Z + (Z_\mathrm{full} - Z)\mathrm{e}^{-r/r_\mathrm{s}}}{r} \tag{4.9}$$

where Z and Z_full are the charges for $r \to \infty$ and $r \to 0$ respectively, and r_s is the screening length which is tuned to obtain I_p. For the TDSE spectrum in figure 4.2 the parameters are $Z = 1$, $Z_\mathrm{full} = 54$ and $r_\mathrm{s} = 0.026$. In the case of effective potentials equation (4.7) does not hold anymore as the dependence of I_p on n is more complicated than for hydrogen-like ions. However, we can analogously define an effective principal quantum number $n_\mathrm{eff} = Z/\sqrt{2I_\mathrm{p}}$ which leads to

$$\alpha_C/\alpha_L = n_\mathrm{eff}\gamma\,. \tag{4.10}$$

Figure 4.5 demonstrates that both hydrogen-like ions and many-electron systems in SAE approximation can be treated on an equal basis for the purpose of this work. There TDSE PES for hydrogen in the excited $2s$ state ($I_\mathrm{p} = 0.125$) and cesium in the ground state (SAE approximation, $6s$ state, $I_\mathrm{p} = 0.143$ obtained using the

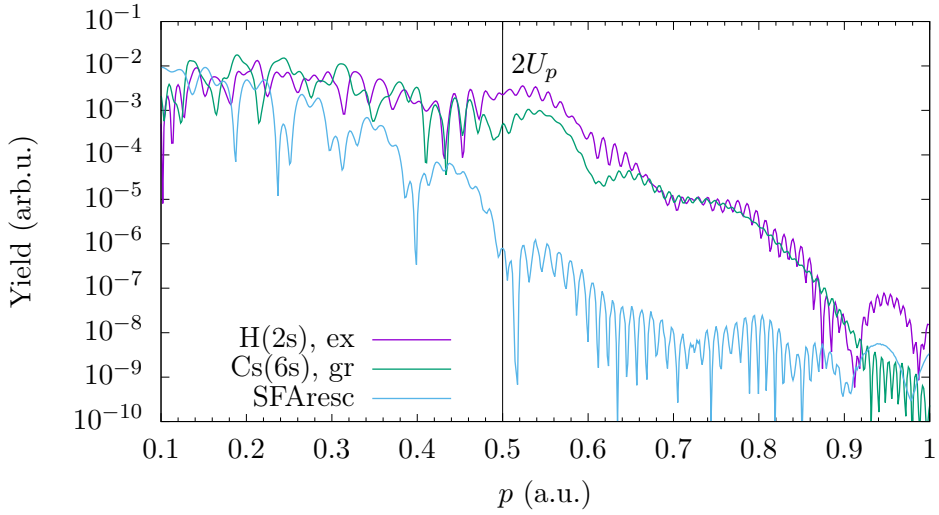

Figure 4.5.: Two TDSE PES for similar I_p realized via an excited state (violet) and an effective potential (green), respectively (see text). In both cases $\alpha_C = 11.3$ and $\alpha_L = 5.7$. The corresponding SFA spectrum is in striking disagreement.

parameters $Z = 1$, $Z_\mathrm{full} = 0.1$ and $r_\mathrm{s} = 3.13$) are compared, including the plain SFA spectrum for hydrogen. The laser parameters are $\omega = 0.0078$ and $E_0 = 0.0039$, leading to the scaling parameters $\alpha_C = 11.3$ and $\alpha_L = 5.7$. Both TDSE spectra are quite similar although the targets are qualitatively different (while having similar I_p), but deviate significantly from the SFA spectrum, as expected from the large ratio $\alpha_C/\alpha_L = 1.98$. It also demonstrates that the Keldysh parameter alone (which is $\gamma = 1$ here as in figure 4.3) is not sufficient to characterize the importance of Coulomb effects.

The conclusion is that the ratio α_C/α_L governs the difference between spectra obtained from TDSE simulations and the predictions of the SFA. The existence of a plateau, i.e., the difference of the slope of the PES below and above $2U_\mathrm{p}$, is associated with the laser parameter α_L, or the strong-field parameter $z_F = \alpha_L^2$, where for larger parameters the plateau is more distinct. This can be recognized when comparing figure 4.3 with $\alpha_L = 4$ and figure 4.4 with $\alpha_L = 6$, the latter having a considerably more pronounced plateau structure.

4.3. Phase-only Coulomb Correction for Quantum Trajectories

Section 4.2 describes the scaling of the TDSE and the (dis)agreement of the plain SFA with the latter. However, the effect leading to the displayed large discrepancy for certain parameters is not revealed. This is the purpose of the next sections, via analyzing the effect in question with the help of quantum trajectories. Our approach is based on the ideas from [63], the foundation of which dates back to the 1960s [19–21].

As basis we use the equations derived in section 2.3. The SFA matrix element in saddle-point approximation (SPA), equation (2.46), is rewritten similar as in section 3.3,

$$M_{\boldsymbol{p}}^{(\mathrm{SFA})} = -2^{-1/2}(2I_\mathrm{p})^{5/4} C(\boldsymbol{p}) \sum_s \frac{1}{S''_{\boldsymbol{p},I_\mathrm{p}}(t_s)} \mathrm{e}^{-\mathrm{i}\int_{t_s}^{t_d} \mathrm{d}t \left(\frac{1}{2}[\boldsymbol{p}+\boldsymbol{A}(t)]^2 + I_\mathrm{p}\right)} \tag{4.11}$$

with $C(\boldsymbol{p}) = \exp\left\{\mathrm{i}\int_0^{t_d} \mathrm{d}t \left(\frac{1}{2}[\boldsymbol{p}+\boldsymbol{A}(t)]^2 + I_\mathrm{p}\right)\right\}$ being a constant phase factor only depending on $\boldsymbol{p}$. Since the integral in the exponent of $C(\boldsymbol{p})$ is purely real, the latter vanishes when calculating the probability $w(\boldsymbol{p}) = |M_{\boldsymbol{p}}|^2$ and thus can be dropped.

Here a Coulomb correction is applied solely to the action integral in the exponent of equation (4.11) while the trajectory remains the same. A detailed derivation based on a perturbative treatment is given in appendix A.4. The action integral (2.47) is modified resulting in

$$S(t_s) = \int_{t_s}^{t_d} \mathrm{d}t' \left(\frac{1}{2}[\boldsymbol{p}+\boldsymbol{A}(t')]^2 - \frac{Z}{\sqrt{\boldsymbol{r}^2(t')}} + I_\mathrm{p}\right) \tag{4.12}$$

which is evaluated along the plain SFA (i.e., uncorrected[2]) trajectory $\boldsymbol{r}(t)$. In contrast to section 2.3 the integrand is position-dependent, so we need the trajectory $\boldsymbol{r}(t)$ explicitly. This is found from Newtons equations of motion,

$$\dot{\boldsymbol{r}} = \boldsymbol{p} + \boldsymbol{A}(t) \tag{4.13a}$$

$$\dot{\boldsymbol{p}} = 0\,. \tag{4.13b}$$

Here we use a notation similar to section 3.3 where $\boldsymbol{p}$ denotes the constant drift momentum and $\boldsymbol{v}$ is the velocity being identical to the kinetic momentum due to the use of atomic units. The EOM can be evaluated analytically,

$$\boldsymbol{v}(t) = \boldsymbol{p} + \boldsymbol{A}(t) \tag{4.14a}$$

$$\boldsymbol{r}(t) = \int_{t_s}^{t} \mathrm{d}t' \,[\boldsymbol{p} + \boldsymbol{A}(t')] + \boldsymbol{r}(t_s)\,, \tag{4.14b}$$

where we have to choose the initial condition $\boldsymbol{r}(t_s)$. The ionization time t_s given

[2]The subscript "0" is omitted for brevity.

by the saddle-point equation (SPE) (2.44) is necessarily complex. This complicates the choice of the initial conditions for $\boldsymbol{r}(t)$ as discussed in section 3.3. There it was chosen such that $\boldsymbol{r}(\operatorname{Re} t_s) \in \mathbb{R}^3$ which ensures a real trajectory for all times $t \geq \operatorname{Re} t_s$. However, this choice involves a non-zero imaginary part of $\boldsymbol{r}(t_s)$ which might seem a little arbitrary. Here we use $\boldsymbol{r}(t_s) = 0$ as initial condition. The resulting divergence of the action integral (4.12) at the lower boundary is treated by a matching procedure as derived in appendix A.5. The problem of complex observables as encountered in section 3.3 does not apply here as the equations of motion are not altered and thus the final electron velocity $\boldsymbol{v}(t \to \infty)$ equals the drift momentum $\boldsymbol{p}$ which is real. The position acquires an imaginary part contributing to the ionization probability, the consequences of which will be discussed in the next section. As only the final momentum is "measured" in this method and not the final position, having a complex $\boldsymbol{r}(t)$ does not violate the requirement of real observables.

The prefactor $1/S''_{\boldsymbol{p},I_\mathrm{p}}(t_s)$ in equation (4.11) is calculated without the additional term in $S(t_s)$, i.e., as in equation (3.27), so that the transition matrix element finally reads

$$M_{\boldsymbol{p}} = -2^{-1/2}(2I_\mathrm{p})^{5/4} \sum_s \frac{\mathrm{e}^{-\mathrm{i}S(t_s)}}{-\boldsymbol{E}(t_s) \cdot (\boldsymbol{p} + \boldsymbol{A}(t_s))} \,. \tag{4.15}$$

with $S(t_s)$ as defined in equation (4.12). As before this has to be evaluated by first determining the saddle-point times t_s given by the SPE (2.44) with a chosen momentum $\boldsymbol{p}$ and then summing up the respective contributions. Here the main effort lies within the evaluation of $S(t_s)$ as this entails a contour integration in the complex time plane. Contrary to the plain SFA (section 2.3) this cannot be circumvented due to the position dependence of the additional Coulomb term $-Z/\sqrt{\boldsymbol{r}^2(t)}$ in the integrand. The issues arising from this are discussed in section 4.4. When applying this formalism to total ionization rates it is sufficient to consider only the most probable trajectory which is the one for $\boldsymbol{p} = 0$. In this case the resulting trajectory becomes purely real and the transition amplitude can be calculated analytically [18], leading to the famous Coulomb-corrected PPT rate [21].

4.4. Complex Integration Pathways

As stated in section 4.3 the most elaborate part in the evaluation of the transition matrix element (4.15) is the contour integral in the action (4.12). The latter must be integrated along a contour in the complex time plane starting from the complex ionization time t_s. The problematic part here is the position-dependent Coulomb term

$$S_C = -\int_{t_s}^{t_d} \mathrm{d}t' \frac{Z}{\sqrt{\boldsymbol{r}^2(t')}} \,. \tag{4.16}$$

The trajectory $\boldsymbol{r}(t)$ is described analytically by equation (4.14). Due to $t_s \in \mathbb{C}$ it acquires an imaginary part. Consequently we have to take the square root $\sqrt{\boldsymbol{r}^2(t)}$ of a complex number, which has two solutions, or branches, as illustrated in figure 4.6. The solution with positive $\mathrm{Re}\,\sqrt{z}$ is defined as the principal value while the other

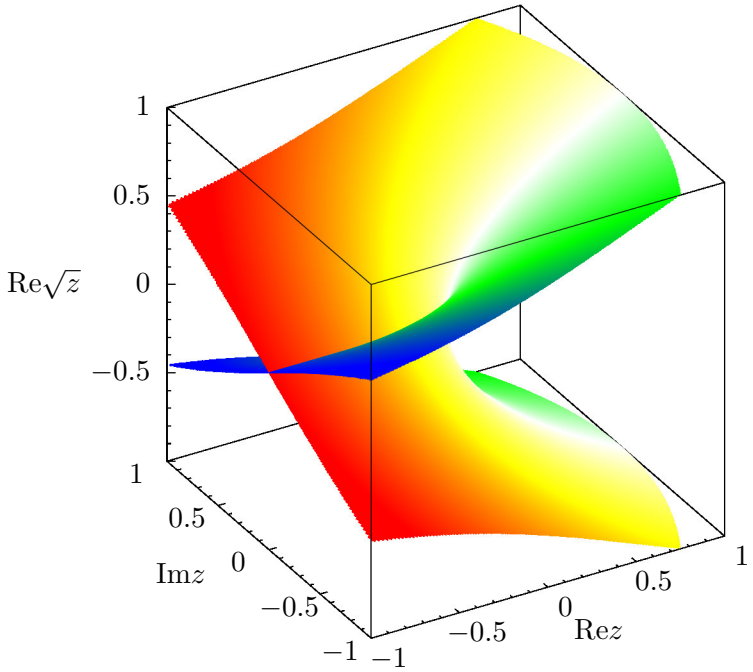

Figure 4.6.: Illustration of the branch point at $z = 0$ and the branch cut for $\mathrm{Re}\,z < 0$, $\mathrm{Im}\,z = 0$ of the complex square root $\sqrt{z}$. The color indicates the imaginary part of the square root, $\mathrm{Im}\,\sqrt{z}$ (blue < 0, white $= 0$, red > 0).

solution carries the opposite sign. The Riemann sheets defined by these different sets of solutions are connected via the branch cut at $\mathrm{Re}\,z < 0$, $\mathrm{Im}\,z = 0$ which terminates in the branch point at $z = 0$. Mathematically speaking, the complex square root is not holomorphic on the whole complex plane. This has severe consequences when integrating over the square root along a complex contour. Starting with the principal value the contour moves along the upper Riemann sheet. If the contour crosses the branch cut the result is ambiguous. Either the integration stays on the upper Riemann sheet but encounters a discontinuity in the derivative, or it switches to the lower Riemann sheet. The latter leads to non-vanishing results when integrating along a closed contour which is most undesirable as it spoils the free choice of the integration path. Either way, integration contours crossing branch cuts must be avoided.

This problem needs to be translated to the present case due to $\sqrt{z} = \sqrt{\boldsymbol{r}^2(t)}$ and the integration contour lying within the complex time plane $t \in \mathbb{C}$. The time dependence of $\boldsymbol{r}(t)$ is shown in equation (4.14b). It contains trigonometric functions (depending on the choice of the vector potential) and is thus far from trivial. The

topology of the resulting branch cuts in the complex time plane has been analyzed in [29, 30, 63].

Examples for the "landscape" in complex time generated by $\sqrt{\boldsymbol{r}^2(t)}$ are shown in figure 4.7 for a short and a long trajectory (refer to section 2.4) with the same momentum ($p_z = 0.69$, $p_y = 0.02$) in the vicinity of the $2U_\mathrm{p}$ cutoff. Parameters are the same as in figure 4.2. For the short trajectory in panel (a) the situation is

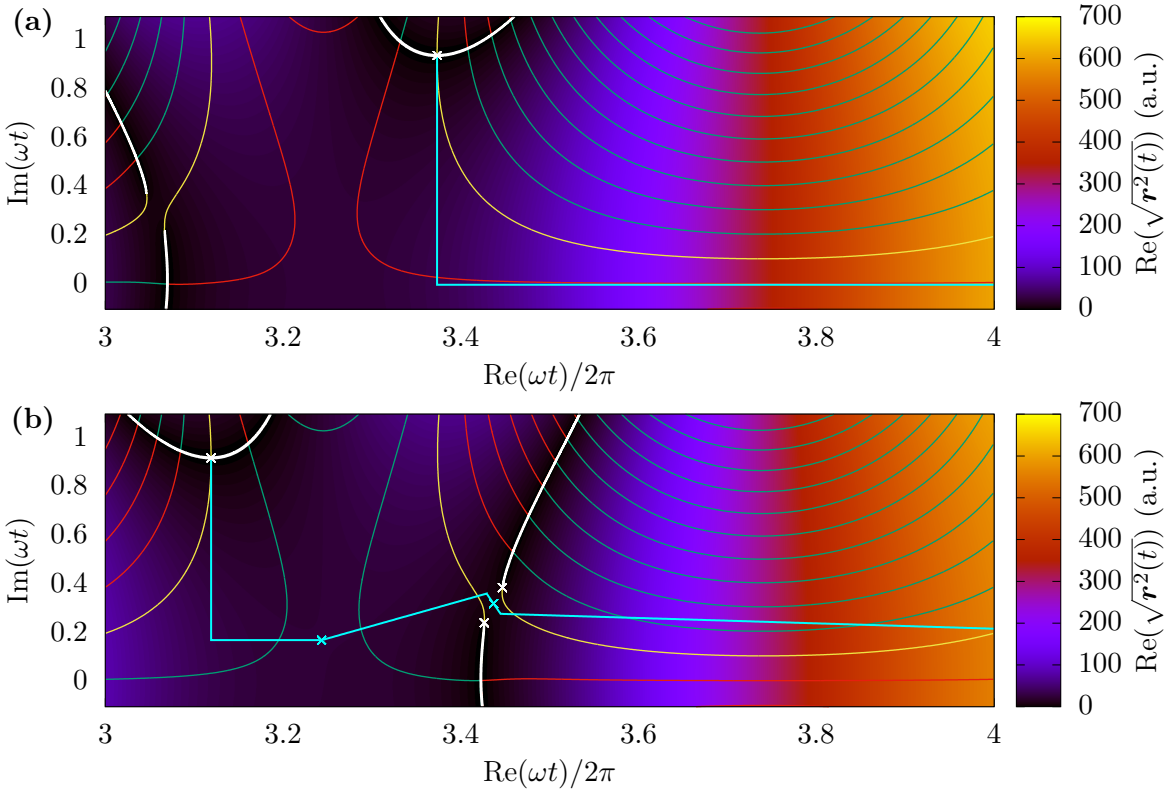

Figure 4.7.: Panels (a) and (b) show integration contours (cyan) in the complex time plane for a short and a long trajectory at the cutoff momentum, respectively (same parameters as in figure 4.2). The color scale shows $\mathrm{Re}\sqrt{\boldsymbol{r}^2(t)}$, the colored lines represent isolines of $\mathrm{Im}\sqrt{\boldsymbol{r}^2(t)}$ (red < 0, yellow $= 0$, green > 0). White lines show branch cuts terminating in branch points (the relevant ones are indicated by white crosses). In panel (b) cyan crosses show the solutions of equation (4.18) used to determine the integration contour.

straightforward. Apart from t_s being a branch point itself (which is treated using a matching procedure as discussed in appendix A.5) there are no obstacles between t_s and t_d. Accordingly the integration path can be chosen as in section 3.3 (indicated by a cyan line in figure 4.7(a); see also figure 3.4). Panel (b) shows a long trajectory which is emitted in the same half-cycle but on the opposite edge of the vector

potential as compared to panel (a). This trajectory revisits the ion before leaving towards the detector as illustrated by $\mathrm{Re}\,\sqrt{\boldsymbol{r}^2(t)}$ which is the real distance between electron and ion. When flying past the ion branch cuts appear in the complex time plane which prohibit the simple integration path as used for the short trajectory. These branch cuts extend towards $\mathrm{Im}\,t \to \pm\infty$ and leave only a small "gate" at finite $\mathrm{Im}\,t$. Figure 4.7(b) shows one possible choice for the integration contour (cyan line) which utilizes this gate to avoid crossing the branch cuts.

The Algorithm The task is now to find a valid integration contour for every trajectory from the respective ionization time $t_s \in \mathbb{C}$ to the detection time $t_d \in \mathbb{R}$ along which the action (4.12) can be evaluated. Doing this manually for a single trajectory is simple, as can be gauged from figure 4.7. For the calculation of a whole spectrum many ($> 10^3$ for a 1D calculation) trajectories have to be evaluated, a task which by far exceeds the limit of reasonable effort when doing it manually. Accordingly an algorithm must be found which automates the construction of valid integration contours. One possibility for such an algorithm is presented in [29] where the emergence of low-energy structures (LES) from complex trajectory calculations is demonstrated. However, the topologies encountered there are much more complicated than in our case since they concentrate on small momenta in polarization direction. On the other hand, the algorithm detailed in [29] does not necessarily handle all situations found for larger momenta which are in focus here.

Our algorithm utilizes the fact that the branch cuts in complex time are associated with returns to the parent ion in real space. These are easily calculated[3] from equation (4.14b) for any given $\boldsymbol{p}$ and t_s. To that end we iteratively determine the minima of $\mathrm{Re}\,\sqrt{\boldsymbol{r}^2(t)}$ on the real time axis for $t > \mathrm{Re}\,t_s - \frac{1}{4}\frac{2\pi}{\omega}$ leaving a little margin for numerical reasons. The resulting minima are used as input for the calculation of branch points as solutions of

$$\boldsymbol{r}^2(t_{\mathrm{branch}}) = 0\,. \tag{4.17}$$

The solutions t_{branch} are indicated in figure 4.7 as white crosses. Note that branch points always come in pairs as discussed in [63]. These form the gate which needs to be passed by the integration contour. Having found one branch point, we calculate the corresponding time of closest approach (as it is termed in [29]) which approximately coincides with the center of the gate. The equation defining these points is

$$\boldsymbol{r}(t_{\mathrm{turn}}) \cdot \boldsymbol{v}(t_{\mathrm{turn}}) = 0 \tag{4.18}$$

in analogy to classical mechanics. This equation has two qualitatively different sets of solutions. One describes the closest approach where the velocity vector is perpendicular to the position vector as measured from the parent ion. The other

[3] This algorithm can only work with the analytically known trajectory $\boldsymbol{r}(t)$. As a consequence, modifying the equations of motion as in chapters 3 and 5 is prohibitive here.

set is characterized by vanishing velocity which in classical mechanics indicates a turning point. In real space these can be easily distinguished as they are minima and maxima of $\boldsymbol{r}^2(t_{\mathrm{turn}})$, respectively. This holds true in complex spacetime, however, we use the simple fact that times of closest approach are always associated with branch points. On the contrary, turning points are far away (in complex time) from any branch point. This condition is easy to implement and, as the topologies in complex time for the relevant[4] trajectories are always similar to those figure 4.7, entirely sufficient here.

In summary, the construction of a valid integration contour is done as follows:

- Find real return time t_{ret} as minimum of $\sqrt{\boldsymbol{r}^2(\mathrm{Re}\, t)}$
- Determine branch point t_{branch} from $\boldsymbol{r}^2(t_{\mathrm{branch}}) = 0$ (with t_{ret} as initial guess)
- Calculate associated gate center t_{gate} by solving $\boldsymbol{r}(t_{\mathrm{gate}}) \cdot \boldsymbol{v}(t_{\mathrm{gate}}) = 0$ (with t_{branch} as initial guess)
- Find intermediate turning point t_{turn} from $\boldsymbol{r}(t_{\mathrm{turn}}) \cdot \boldsymbol{v}(t_{\mathrm{turn}}) = 0$ (about halfway between t_s and t_{gate})

The integration contour needs to include t_{turn} and t_{gate} as primary waypoints. Additionally some secondary waypoints are inserted to further reduce the probability of crossing the branch cuts. One is $t_{\mathrm{secondary}} = \mathrm{Re}\, t_s + \mathrm{i}\, \mathrm{Im}\, t_{\mathrm{turn}}$ assuring that the integration contour runs perpendicular to the branch cuts associated with t_s. The other ones are arranged around t_{gate} in a way that the gate is crossed perpendicularly. An example for the resulting integration contour is displayed in figure 4.7(b) where crosses indicate the branch points t_s, t_{branch} (white) and saddle points t_{gate}, t_{turn} (cyan). The secondary waypoints are visible as kinks in the integration contour.

Limitations As already mentioned the applicability of the algorithm detailed above is limited. The first limitation to be named is the huge diversity of different topologies encountered. Our algorithm is designed for soft recollisions at medium to large momenta in polarization direction and small perpendicular momenta. It might handle multiple returns if they are "well-behaved", i.e., similar to the ones considered above. For more complicated topologies like the ones discussed in [29] for small drift momenta, or in the case of large perpendicular momenta, one needs a more general algorithm. Due to these difficulties our propagation routine includes checks whether a branch cut was crossed accidentally and excludes these trajectories from the final result.

Another limitation is the dependence on the drift momentum perpendicular to the polarization direction. For vanishing perpendicular component of the drift momentum the branch point pair merges into a single pole (cf. [63]) and the contribution of the Coulomb integral (4.16) diverges. Accordingly this theory is only applicable for non-zero perpendicular drift momenta. Spectra along the polarization direction are

[4] For the effect under consideration in this chapter.

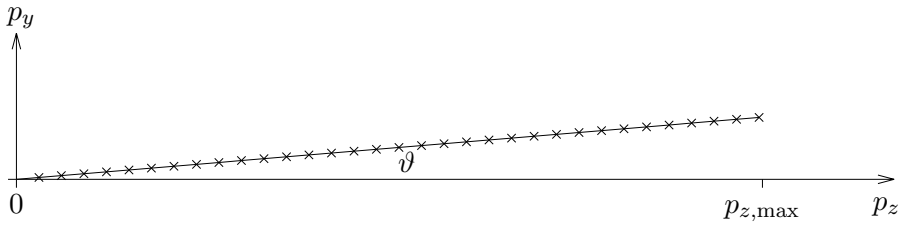

Figure 4.8.: Sketch of how momenta are selected in the two-dimensional momentum plane for the calculation of PES according to equation (4.15). As the momenta on the polarization axis $\boldsymbol{e}_z$ are not accessible (see text), the desired momenta (indicated by black crosses) are chosen on a line tilted by the small angle ϑ against $\boldsymbol{e}_z$.

thus inaccessible. Unfortunately these are of utmost interest as the TDSE spectra in section 4.2 are calculated on the polarization axis. This problem is solved by choosing momenta on a line which is slightly tilted by some angle ϑ with respect to the latter as illustrated in figure 4.8. The resulting spectra quantitatively depend on ϑ up to a divergence for $\vartheta \to 0$. Additionally for small ϑ the approximations made in the derivation of equation (4.12) (see appendix A.4) break down as the difference between uncorrected and full trajectory becomes large. Thus an appropriate ϑ needs to be chosen to obtain reasonable results. This procedure might appear somewhat arbitrary, however, the qualitative significance of the results presented below remains unaffected.

Finally the action obtained above depends on the upper integration limit. The integration to $t_d \to \infty$ cannot be carried out analytically as in chapters 3 and 5 due to the perturbative nature of the method[5] (as discussed in [18]). This results in changing interference patterns and slight modulations in the trajectory weight depending on the numerically chosen upper integration limit t_d. Again, as the discussions below happen only on a qualitative level, this problem is disregarded in the following.

4.5. Spectral Analysis

The algorithm explained in section 4.4 can now be used to evaluate the action integral (4.12) and thus the matrix element (4.15). Doing that for many momenta in the desired momentum range we find the momentum-resolved photoelectron spectrum predicted by our Coulomb-corrected SFA. As explained above the quantitative significance of the results obtained here is limited since the weight of the trajectories strongly depends on the angle ϑ with respect to the polarization axis (see figure 4.8). This dependence is demonstrated in figure 4.9.

[5] For the analytical propagation to infinity it is necessary that the trajectory follows the equations of motion that are reflected in the integrand of the action, which is not the case here.

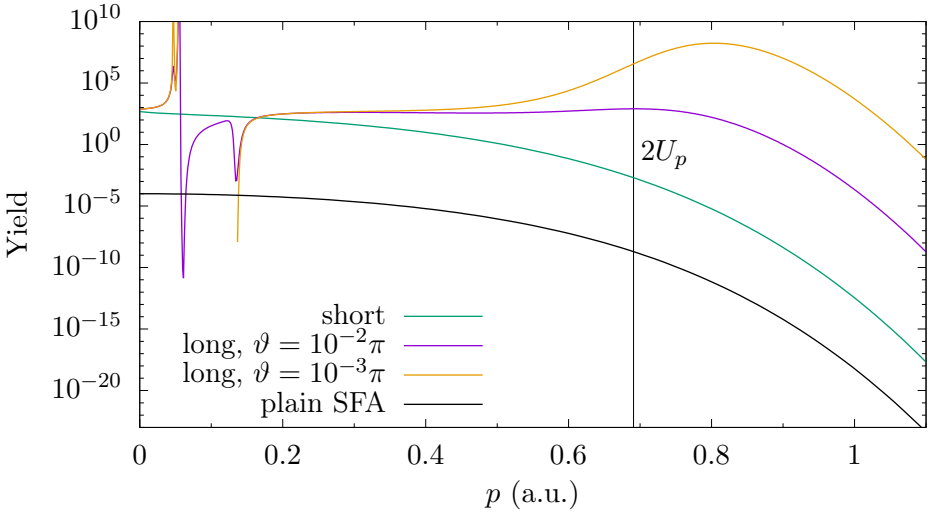

Figure 4.9.: Partial spectra for the same parameters as in figure 4.2. For every momentum only a single trajectory (long or short, as indicated) has been evaluated. In the plain SFA (including only the direct term) long and short contributions are identical. For the long trajectories different angles ϑ (see text) are displayed. The peak structures at small momenta are signatures of the LES which are discussed in great detail in [29, 30].

Here we show partial spectra obtained by limiting the real part of the ionization time t_s to one quarter of an optical cycle. This allows us to select either long or short trajectories as indicated in figure 2.2. For the plain SFA the contributions of both are identical and need not be distinguished. For the Coulomb-corrected SFA these are qualitatively different. The figure shows a plain SFA spectrum as reference. Since only one single trajectory per momentum contributes to the spectrum no intra-cycle interference pattern appears. The "short" spectrum qualitatively matches the plain SFA spectrum but is shifted vertically due to the additional Coulomb term. This resembles the main effect of the Coulomb correction for the PPT rate [21]. The "long" spectrum is shown for two different angles ϑ. For the larger angle $\vartheta = 10^{-2}\pi$ a flat plateau up to $2U_\mathrm{p}$ is visible. For the ten times smaller angle $\vartheta = 10^{-3}\pi$ the yield above $2U_\mathrm{p}$ is increased by several orders of magnitude, thus demonstrating the strong dependence on ϑ. Nevertheless the result for the larger angle nicely produces a flat plateau as seen in the TDSE spectra in figures 4.2 and 4.5. From that we can conclude that the Coulomb correction we applied to the SFA indeed improves the agreement with the TDSE, although only on a qualitative level. The formulation in terms of trajectories allows us to analyze this qualitative change in detail.

Formally the only difference between the plain SFA in SPA as in section 2.3 and the Coulomb-corrected SFA used here is the Coulomb integral (4.16). Accordingly the increased yield around $2U_\mathrm{p}$ is not caused by electrons shifted to larger momenta as observed in chapter 3. Instead the ionization probability or weight of the trajectories

is changed. As shown in section 2.3 the weight of a single trajectory is mainly determined by the imaginary part of its action integral,

$$\log w_{\boldsymbol{p}} \propto -\mathrm{Im}\, S\,. \tag{4.19}$$

The contribution of the Coulomb integral to the trajectory weight can thus be gauged by taking a closer look at its imaginary part. As long and short trajectories are qualitatively different where the short ones behave similar to the plain SFA trajectories, it is useful to compare the behavior of $\mathrm{Im}\, S_C(t)$ along the integration contours for both types. This is shown in figure 4.10 for the integration contours from figure 4.7. For the long trajectory the saddle points t_{turn} and t_{gate} determined by the algorithm from section 4.4 as solutions of equation (4.18) are indicated by black crosses. We observe the following behavior: the "short" curve rises up to a sharp kink which indicates the change in direction of the integration contour when reaching the real time axis, see figure 4.7(a). From there it monotonously decreases until it converges to its final value ($\mathrm{Im}\, S_C^{\mathrm{short}}(t_d) = 6.67$). The "long" curve rises until it passed the gate at t_{gate}, see also figure 4.7(b). Subsequently it decreases monotonously as well until it reaches the final value ($\mathrm{Im}\, S_C^{\mathrm{long}}(t_d) = 12.85$). This monotonous decrease is caused by the imaginary part of the position $\boldsymbol{r}(t)$ which is acquired along the propagation to the real time axis and mainly depends on the imaginary part of t_s. It is essentially identical for long and short trajectories with the same drift momentum $\boldsymbol{p}$ and thus not of interest here.

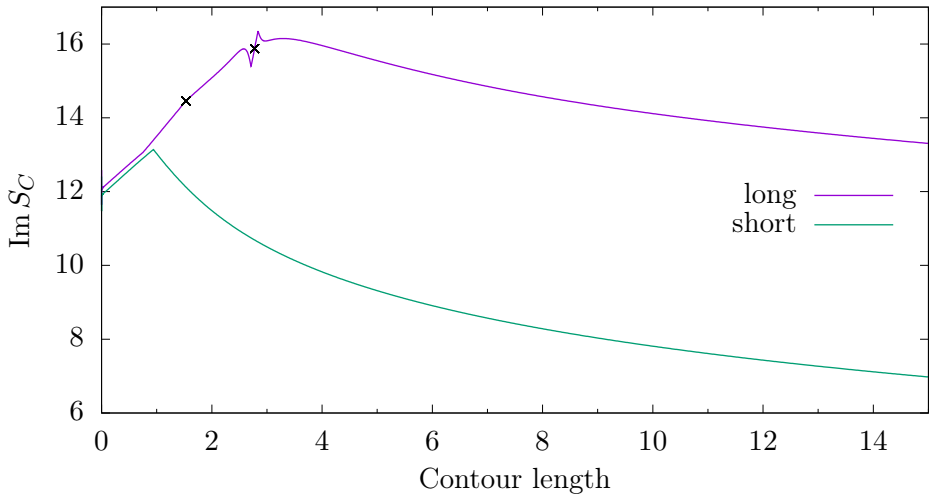

Figure 4.10.: The behavior of the imaginary part $\mathrm{Im}\, S_C(t)$ of the Coulomb integral (4.16) along the integration contours from figure 4.7. Note that every kink here is related to a change of direction in the integration contour. Black crosses indicate the respective solutions of equation (4.18).

Figure 4.10 shows that the observed huge difference emerges from the propagation of the long trajectory between t_s and t_{gate}, both of which are complex. The

SMT (see section 2.4) states that recollisions can be understood as ionization with a certain probability which is then followed by a scattering event. This interpretation is applied in chapter 3 where the propagation is split into the tunneling step determining the trajectory weight and the classical propagation to the detector, the latter including rescattering events. Here the situation is considerably different. Before passing the gate the integration contour must stay complex. It is possible to integrate partially along the real time axis, yet the gate must be passed at non-vanishing[6] $\operatorname{Im} t$. Afterwards the integration contour may stay on the real time axis up to the detection time t_d. This has serious consequences. Due to the integration contour being forced into the complex time plane the weight of a trajectory is not fixed after the tunneling step but determined by the whole propagation up to the detector. Especially the soft recollisions severely change the weight which leads to the probability enhancement for momenta around the $2U_\mathrm{p}$ cutoff. This puts the whole concept of a "tunnel exit" into perspective as it is not well-defined within this concept. Here, on the contrary, the whole propagation up to the gate[7] can be interpreted as being "under the barrier" motion as it still influences the ionization probability.

4.6. Conclusions

We have demonstrated that orders-of-magnitude differences between TDSE and SFA PES can occur at electron energies around the $2U_\mathrm{p}$ cutoff. This disagreement is reduced to the ratio $\alpha_C/\alpha_L = n\gamma$ of two scaling constants derived from the TDSE. The greater this ratio, the bigger the expected disagreement, as shown in figures 4.2 ($\alpha_C/\alpha_L = 1.44$, disagreement), 4.3 ($\alpha_C/\alpha_L = 1$, agreement), 4.4 ($\alpha_C/\alpha_L = 0.67$, good agreement) and 4.5 ($\alpha_C/\alpha_L = 1.98$, strong disagreement). This disagreement was analyzed in terms of quantum trajectories. As the plain SFA is not sufficient to reproduce this effect, we implemented a perturbative Coulomb correction for the complex SFA trajectories, taking into account that the choice of the integration contour is severely restricted by branch points and cuts in the complex time plane. We found that the ionization probability of certain trajectories is significantly altered when the integration contour is forced to cross gates between branch points at complex times. Physically, these parts of the integration contours correspond to soft recollisions.

We found that our method can reproduce the observed orders-of-magnitude enhancement in the probability. Thus we conclude that the whole time propagation of the electron from the ionization time to the detector influences the weight of a trajectory. Of course, this is a matter of physical interpretation of the mathematics rather than of quantum mechanical observables. However, this argumentation allows us to view the concept of a tunnel exit in a different light, as the ultimate approach

[6] At least in some cases. This depends on the topology, i.e., on the vector potential, the drift momentum and the corresponding ionization time.

[7] Or even the *last* gate, as there might be several returns.

of the real time axis[8] does not necessarily happen at the real part of the ionization time. On the contrary, in the case of soft recollisions this ultimate approach can happen only after the last return, making the concept of a tunnel exit somewhat arbitrary.

Another effect that must be considered here is the so-called Coulomb focusing. One could argue that the increased probability at the cutoff energy is generated by many classical trajectories being focused into the considered energy range by the Coulomb potential[9]. In our method this effect would then be encoded as increased weight of a single *guiding* trajectory. This explanation is highly unlikely as it can hardly produce changes of several orders of magnitude as observed here. Furthermore, previously used methods including Coulomb focusing (similar to the methods used in chapters 3 and 5) failed to reproduce the effect considered in this chapter.

These conclusions challenge the validity of the three-step model, i.e., the separability of tunneling ionization into the tunneling step and the free propagation afterwards, and all models derived from the latter. However, one should consider that the visibility of the discussed effect in photoelectron spectra is only significant within a certain parameter range as indicated above. In most cases the influence on observables is negligible and consequently the three-step model is sufficiently valid. What should be kept in mind is the conclusion that recollisions are inherently quantum and should not lightly be treated as purely classical.

[8] Which is the usual definition of the tunnel exit in this context.

[9] This is the case for the caustics corresponding to the LES as demonstrated in [24].

5. Photoelectron Spectra Beyond the Dipole Approximation

5.1. Motivation

The dipole approximation is quite commonly applied in strong-field physics. However, its validity is rarely questioned. The assumption is usually that the dipole approximation is sufficiently accurate when the wavelength is much larger than the typical length scales of the problem, e.g. the electron excursion, or the electron velocity is much smaller than c, the speed of light in vacuum (which is $c \approx 137\,\text{a.u.}$). Both conditions lead to the expression $A_0/c \ll 1$ with A_0 being the amplitude of the vector potential. For the parameters used below (the same as in reference [9]) we find $A_0/c \approx 0.02$ which sufficiently fulfills the condition from above, thus one would expect no observable non-dipole effects.

However, recent experiments [8, 9] show results that measurably deviate from the expectations obtained using the dipole approximation. Most remarkable is the fact that this happens for large wavelengths and rather non-relativistic intensities. The observations are that photoelectron spectra (PES) are shifted with respect to the direction of the *propagation* of the laser pulse. In dipole approximation the latter does not enter the calculation of PES. Such shifts have been theoretically reproduced using classical trajectory Monte Carlo (CTMC) and similar [9, 64], methods derived from the strong field approximation (SFA) [65–67], time-dependent Schrödinger equation (TDSE) calculations [68] and even the time-dependent Dirac equation [69]. It is consistently attributed to the transfer of photon momentum to the electrons or, classically speaking, to the magnetic part of the Lorentz force, which are two sides of the same coin, i.e., light pressure. It has been observed that the shift of the spectrum can be in or (counterintuitively) against propagation direction, which has been associated with Coulomb effects leading to momentum partitioning between electron and ion. This has been discussed in some detail in [68] in terms of classical trajectories where it was found that the long trajectories (see section 2.4) are the main cause for this. In [67] a non-dipole SFA was developed using the exact non-dipole Volkov solution for the Schrödinger equation and including Coulomb effects via rescattering.

Despite the abundance of literature on this topic we show that the trajectory-based Coulomb-corrected strong field approximation (TCSFA) can be adapted to reproduce this effect as well. The strategy is similar to that in section 3.3. Additionally we derive relativistically corrected equations of motion and include the magnetic field of the laser. Based on the results we construct a semi-analytical model in the

spirit of the simple man's theory (SMT) (see section 2.4) where we perturbatively include the action of the magnetic field as well as the Coulomb interaction. We show that this simple model is able to explain the observed counterintuitive shift of the spectrum against propagation direction. This chapter contains results from [70], but here more details are given.

5.2. Non-Dipole Quantum Trajectories

As in the previous chapters the basis for the method presented here is the SFA in saddle-point approximation (SPA) from section 2.3. For the derivations presented in this section SI units are used. The inclusion of the Coulomb potential happens in analogy to section 3.3 where a cluster model potential was included instead. However, the most important difference to the previous considerations is the omission of the dipole approximation and the hence necessary modification of the vector potential. The latter acquires a position dependence,

$$\boldsymbol{A}(\boldsymbol{r},t) = A_0 \boldsymbol{e}_z \sin^2(\Omega t - \boldsymbol{K}\cdot\boldsymbol{r}) \sin(\omega t - \boldsymbol{k}\cdot\boldsymbol{r} + \varphi) \tag{5.1}$$

$$= A_0 \boldsymbol{e}_z \sin^2(\Phi) \sin(\phi) \tag{5.2}$$

where a $\sin^2$-shaped envelope function was chosen as in the previous chapters, which is defined as above for $0 < \Phi < \pi$ and zero otherwise. The abbreviations $\phi = \omega t - \boldsymbol{k}\cdot\boldsymbol{r} + \varphi$ and $\Phi = \Omega t - \boldsymbol{K}\cdot\boldsymbol{r}$ are introduced, the carrier-envelope phase φ is set to 0 in the following. $A_0 = -E_0/\omega$ is the amplitude of the vector potential, E_0 the amplitude of the electric field and $\Omega = \omega/(2n_c)$ the envelope frequency with n_c the number of optical cycles. The propagation direction is set by the wave vector $\boldsymbol{k} = \boldsymbol{e}_y\omega/c$ and the corresponding envelope wave vector $\boldsymbol{K} = \boldsymbol{k}/(2n_c)$. The fields $\boldsymbol{E}(\boldsymbol{r},t) = -\frac{\partial}{\partial t}\boldsymbol{A}(\boldsymbol{r},t)$ and $\boldsymbol{B}(\boldsymbol{r},t) = \boldsymbol{\nabla}\times\boldsymbol{A}(\boldsymbol{r},t)$ read

$$\boldsymbol{E}(\boldsymbol{r},t) = E_0 \boldsymbol{e}_z \sin(\Phi)\left(\frac{1}{n_c}\cos(\Phi)\sin(\phi) + \sin(\Phi)\cos(\phi)\right) \tag{5.3}$$

$$\boldsymbol{B}(\boldsymbol{r},t) = \frac{E_0}{c}\boldsymbol{e}_x \sin(\Phi)\left(\frac{1}{n_c}\cos(\Phi)\sin(\phi) + \sin(\Phi)\cos(\phi)\right) \tag{5.4}$$

$$= \frac{1}{c}\left(\boldsymbol{E}(\boldsymbol{r},t)\cdot\boldsymbol{e}_z\right)\boldsymbol{e}_x\,. \tag{5.5}$$

Without position dependence the latter would not be present at all. In most cases this is a good approximation due to $|\boldsymbol{B}| = \frac{1}{c}|\boldsymbol{E}|$ as follows from the equations given above.

The presence of a magnetic field calls for a modification of the equations of motion to include its effects on the electron trajectory. In contrast to the previous chapters we use the kinetic momentum $\boldsymbol{p}$ instead of the drift momentum. Accordingly the

EOM read

$$\frac{\mathrm{d}}{\mathrm{d}t}\boldsymbol{r} = \boldsymbol{v}\,, \quad \frac{\mathrm{d}}{\mathrm{d}t}\boldsymbol{p} = \boldsymbol{F} \tag{5.6}$$

as known from classical mechanics. The force

$$\boldsymbol{F} = -e\left(\boldsymbol{E} + \boldsymbol{v} \times \boldsymbol{B}\right) - \boldsymbol{\nabla} V \tag{5.7}$$

consists of the Lorentz force

$$\boldsymbol{F}_{\mathrm{L}} = -e\left(\boldsymbol{E} + \boldsymbol{v} \times \boldsymbol{B}\right)\,, \tag{5.8}$$

which now additionally contains the magnetic term $\boldsymbol{v} \times \boldsymbol{B}$, and the Coulomb force

$$\boldsymbol{F}_{\mathrm{C}} = -\boldsymbol{\nabla} V \tag{5.9}$$

$$V(\boldsymbol{r}) = -\frac{eZ}{\sqrt{\boldsymbol{r}^2(t)}}\,. \tag{5.10}$$

Knowing the relation between $\boldsymbol{B}$ and $\boldsymbol{E}$ we see that the magnetic part of the Lorentz force is by a factor of $\frac{v}{c}$ smaller than the electric part. To incorporate this correctly into the electron trajectory it is useful to take the relativistic relation between momentum and velocity,

$$\boldsymbol{p} = \gamma m_{\mathrm{e}} \boldsymbol{v} \tag{5.11}$$

where m_{e} is the rest mass of the electron and

$$\gamma = \frac{1}{\sqrt{1 - \frac{v^2}{c^2}}} \tag{5.12}$$

is the well-known Lorentz factor. As we want to write the EOM in terms of $\boldsymbol{r}$ and $\boldsymbol{p}$ we need to express $\boldsymbol{v}$ as a function of $\boldsymbol{p}$ which can be done using the energy-momentum relation

$$E = \sqrt{p^2c^2 + m_{\mathrm{e}}^2 c^4} \tag{5.13}$$

$$= \gamma m_{\mathrm{e}} c^2 \tag{5.14}$$

from which we find

$$\gamma = \sqrt{1 + \frac{p^2}{m_{\mathrm{e}}^2 c^2}} \tag{5.15}$$

and thus

$$\boldsymbol{v} = \frac{\boldsymbol{p}}{m_{\mathrm{e}}\sqrt{1 + \frac{p^2}{m_{\mathrm{e}}^2 c^2}}}\,. \tag{5.16}$$

Accordingly the rewritten EOM read

$$\frac{\mathrm{d}}{\mathrm{d}t}\boldsymbol{r} = \frac{\boldsymbol{p}}{m_\mathrm{e}\sqrt{1+\frac{p^2}{m_\mathrm{e}^2c^2}}} \tag{5.17a}$$

$$\frac{\mathrm{d}}{\mathrm{d}t}\boldsymbol{p} = -e\left(\boldsymbol{E} + \frac{\boldsymbol{p}}{m_\mathrm{e}\sqrt{1+\frac{p^2}{m_\mathrm{e}^2c^2}}} \times \boldsymbol{B}\right) - \boldsymbol{\nabla} V(\boldsymbol{r})\,. \tag{5.17b}$$

One should note that these, although using the relativistic velocity-momentum relation, are not fully relativistic since we neglect retardation effects. However, it turns out that this does not pose a problem for the effects considered here.

The trajectories can now be found by numerically evaluating the EOM (5.17). To obtain PES it is necessary to calculate the action integral from equation (2.47) including additional terms, which is performed similar to section 3.3. The time integration is split into the sub-barrier part and the real-time propagation (see figure 3.4 for an illustration of the integration contour). The sub-barrier part is calculated analytically as in the plain SFA,

$$S_\mathrm{sub}(t_s) = \int_{t_s}^{\mathrm{Re}\,t_s} \mathrm{d}t' \left(\frac{[\boldsymbol{p}_\mathrm{drift} + \boldsymbol{A}(t')]^2}{2m_\mathrm{e}} + I_\mathrm{p}\right) \tag{5.18}$$

where $\boldsymbol{p}_\mathrm{drift}$ is the drift momentum at t_s and thus the one inserted into the saddle-point equation (SPE) (2.44) which reads in SI units

$$[\boldsymbol{p}_\mathrm{drift} + e\boldsymbol{A}(t_s)]^2 = -2I_\mathrm{p}\,. \tag{5.19}$$

Here we used $\boldsymbol{A}(t) = \boldsymbol{A}(\boldsymbol{r} = 0, t)$, assuming that the tunneling process is not influenced by the magnetic field. It would as well be possible to include relativistic tunneling effects [71] but since the parameters we use are non-relativistic the difference would be negligible.

The real-time propagation starting at $\mathrm{Re}\,t_s$ includes the changes made to the EOM discussed above, the corresponding action reads

$$S_\mathrm{real}(t_s) = \int_{\mathrm{Re}\,t_s}^{t_d} \mathrm{d}t' \left(\frac{\boldsymbol{p}^2(t')}{2m_\mathrm{e}} + V(\boldsymbol{r}(t')) + I_\mathrm{p}\right)\,. \tag{5.20}$$

This expression is identical to the classical expression obtained in section 3.3. Relativistic corrections to it could be derived with the relativistic kinetic energy expression

$$E - m_\mathrm{e}c^2 = \frac{\boldsymbol{p}^2}{2} + \mathcal{O}\left(\frac{v^2}{c^2}\right)\,. \tag{5.21}$$

Using this yields above expression and higher order terms which are at least quadratic in $\frac{v}{c}$. Since the effect considered here is caused by the influence of the magnetic field

which is linear in $\frac{v}{c}$ we keep only terms $\mathcal{O}\left(\frac{v}{c}\right)$ and neglect those of higher order. This allows the use of the non-relativistic TDSE (on which all theory in this thesis is based) in the first place.

Finally expressions (5.18) and (5.20) are added up to the total action integral

$$S(t_s) = S_{\mathrm{sub}}(t_s) + S_{\mathrm{real}}(t_s)\,. \tag{5.22}$$

This is inserted into the transition matrix element (3.28) for a single trajectory. To obtain PES many trajectories are calculated as described in section 3.3. The initial conditions for the real-time propagation are also derived in the same way which yields

$$\boldsymbol{p}(\mathrm{Re}\, t_s) = \boldsymbol{p}_{\mathrm{drift}} + e\boldsymbol{A}(\mathrm{Re}\, t_s) \tag{5.23a}$$

$$\boldsymbol{r}(\mathrm{Re}\, t_s) = \boldsymbol{\alpha}(\mathrm{Re}\, t_s) - \mathrm{Re}\, \boldsymbol{\alpha}(t_s) \tag{5.23b}$$

with the elongation $\boldsymbol{\alpha}(t)$ from equation (2.62) which in SI units reads

$$\boldsymbol{\alpha}(t) = \frac{e}{m_{\mathrm{e}}} \int^t \mathrm{d}t' \boldsymbol{A}(t')\,. \tag{5.24}$$

From there the propagation is performed to the detection time $t_d \to \infty$ as the upper limit. For the numerical evaluation some finite time t_d needs to be chosen carefully. Whereas in the previous chapters it was sufficient to choose the end of the pulse $T_{\mathrm{p}} = n_c \frac{2\pi}{\omega}$ as the upper limit, here we have to ensure that for all considered trajectories the laser pulse has completely passed by. As the electron velocities are always much smaller than c it is sufficient to choose t_d significantly larger than T_{p}, e.g., $t_d = 2T_{\mathrm{p}}$. Once the laser is off, $\boldsymbol{A}(\boldsymbol{r}(t_d), t_d) = 0$, the propagation to infinity can be carried out analytically using Kepler's laws (see appendix B.1), neglecting relativistic corrections $\mathcal{O}\left(\frac{v^2}{c^2}\right)$ as above.

5.3. Photoelectron Spectra and Trajectory Analysis

To show that our method presented in section 5.2 is able to reproduce shifts of PES in or against propagation direction we calculate a spectrum using parameters from [9]. There it was observed that the spectra were on average slightly shifted against polarization direction, both experimentally and in CTMC calculations. From here on atomic units (see section 2.1) shall be used again unless noted otherwise.

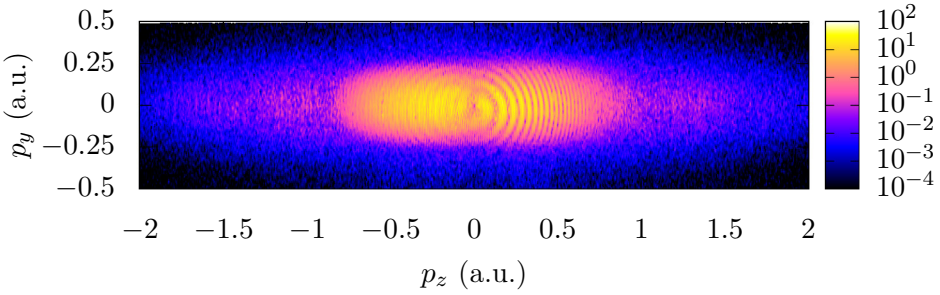

Figure 5.1.: Momentum-resolved photoelectron spectrum for a model xenon atom with $I_\mathrm{p} = 0.447$ irradiated by a six-cycle $\sin^2$-shaped laser pulse. The laser intensity is $I = 6 \times 10^{13}\,\mathrm{W/cm^2}$, the wavelength $\lambda = 3.4\,\mu\mathrm{m}$. p_z is the momentum in polarization direction, p_y in propagation direction of the laser pulse. The probability distribution $w_{\boldsymbol{p}} = |\sum M_{\boldsymbol{p}}|^2$ is plotted.

The obtained PES for a model xenon atom with $I_\mathrm{p} = 0.447$ is shown in figure 5.1. It is irradiated by a six-cycle $\sin^2$-shaped laser pulse with an intensity of $I = 6 \times 10^{13}\,\mathrm{W/cm^2}$ ($E_0 = 0.0413$) and a wavelength of $\lambda = 3.4\,\mu\mathrm{m}$ ($\omega = 0.0134$). We numerically propagated $N = 6 \times 10^7$ trajectories to obtain the presented spectrum. The $2U_\mathrm{p}$ cutoff for direct electron emission is at $p_z \approx 3.1$, accordingly the spectrum covers only small momenta compared to the momentum ranges considered in chapters 3 and 4. The shift is not visible in figure 5.1 although slight asymmetries with respect to the propagation direction $\boldsymbol{e}_y$ can be observed.

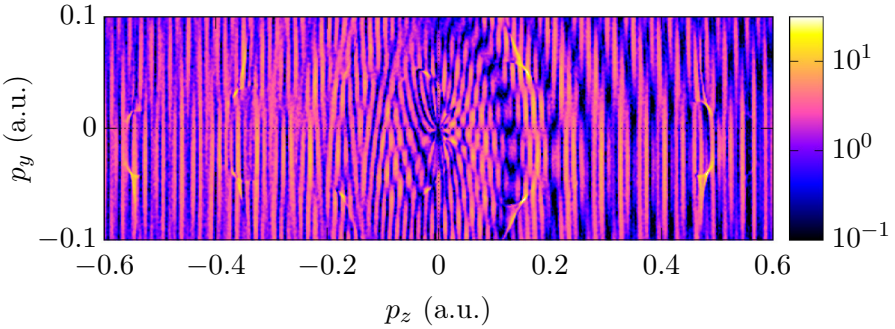

Figure 5.2.: Same as figure 5.1 but for a smaller momentum range and calculated with higher resolution.

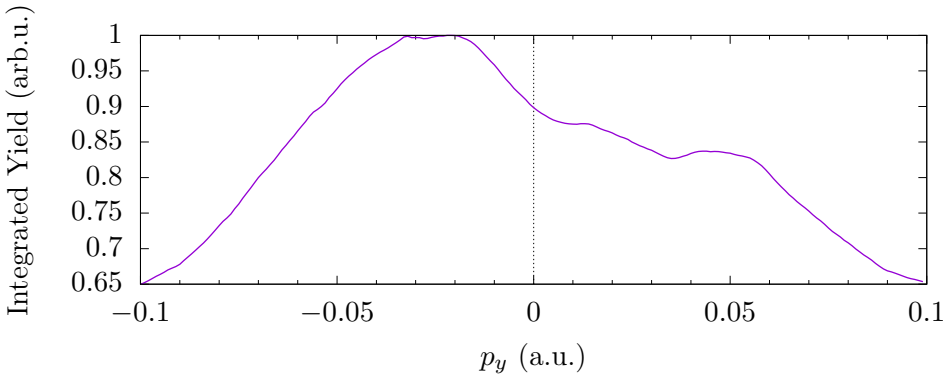

Figure 5.3.: Same parameters as in figure 5.2 but integrated over p_z and rescaled so that the maximum value is 1. Additionally the spectrum has been smoothed prior to integration.

When zooming into the central part (figure 5.2) the asymmetries are more distinct. The most prominent features are the caustics for $p_z \approx 0.5$ and $p_z \approx -0.55$. These can be identified as the so-called low-energy structures (LES) [1, 4, 72]. Evaluating the equations given in [72] predicts LES from the strongest peaks of the used $\sin^2$-pulse at $p_z = 0.487$ and $p_z = -0.548$ which matches the positions observed in figure 5.2. Closer inspection shows that these structures are indeed slightly shifted in negative p_y direction, that is, against propagation direction. What can only be guessed from that figure is that the center of the whole spectrum is shifted towards negative p_y. As in [9] this can be illustrated by projecting the spectrum onto the p_y axis by integrating over p_z. This is shown in figure 5.3.

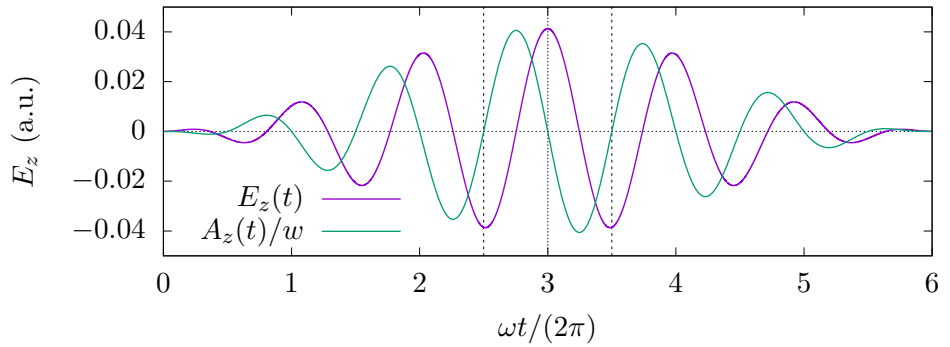

Figure 5.4.: The $\sin^2$ pulse shape used for the numerical calculations. The figure shows the electric field in z direction $E_z(t)$ and the corresponding vector potential $A_z(t)$ scaled by the frequency ω. The central optical cycle as the relevant time window used for the calculation of the shift in figure 5.5 is indicated by vertical dashed lines.

The center of the distribution is shifted by $\Delta p_y \approx -0.025$ which is on the same

order as the shift observed in [9] for the same parameters. We conclude that our method is able to reproduce the previously observed non-dipole effects with reasonable accuracy.

Based on that we want to go one step further and analyze the effect of spectral shift in terms of trajectories. This shift can be visualized very well by considering the difference to the plain SFA. Every trajectory calculated to produce the spectra shown above has some initial drift momentum $\boldsymbol{p}_{\text{drift}}$ which in the plain SFA is the final momentum for that trajectory as well. Accordingly the difference between $\boldsymbol{p}_{\text{drift}}$ and the numerically obtained $\boldsymbol{p}_\infty = \boldsymbol{p}(t \to \infty)$ should give an impression on the shift of the spectrum.

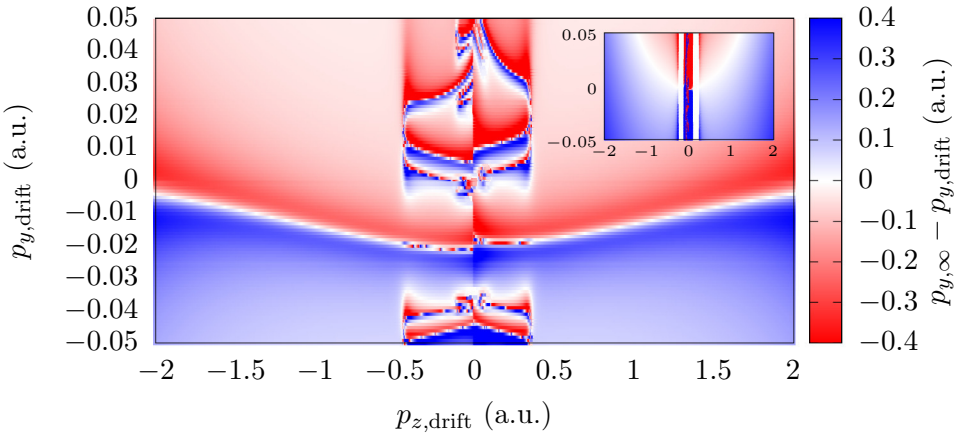

Figure 5.5.: Momentum shift $p_{y,\infty} - p_{y,\text{drift}}$ in direction of $\boldsymbol{e}_y$, plotted against $\boldsymbol{p}_{\text{drift}}$. Color scale shows positive (blue) or negative (red) shift. The main figure (inset) shows only long (short) trajectories. The color scale for the inset spans only one twentieth of that in the main figure.

As we are interested in the shift in propagation direction we look at the components in $\boldsymbol{e}_y$ direction only. We also distinguish between long and short trajectories as in [68] it was stated that the long trajectories are responsible for the counterintuitive shift against the laser propagation direction. Accordingly only one trajectory (i.e., the most important solution of the SPE) per momentum is selected within the time window depicted in figure 5.4. The result is shown in figure 5.5 where the main figure (inset) shows the long (short) trajectories. The color scale is chosen such that blue (red) shows positive (negative) shifts. The message of the figure might not be accessible at first sight, however, its significance will become clear in the following. The central part for $|p_{z,\text{drift}}| \lessapprox 0.5$ shows chaotic behavior. This can be attributed to trajectories which return several times to the parent ion and are therefore scattered in basically random directions. The reason for the relatively sharp boundary of the chaotic region is illustrated in figure 5.6 where three plain SFA long trajectories in a flat-top laser pulse are plotted in position space for small perpendicular momentum $p_y = 0.1$ and different parallel momenta p_z. Note that the z axis spans 2000 atomic

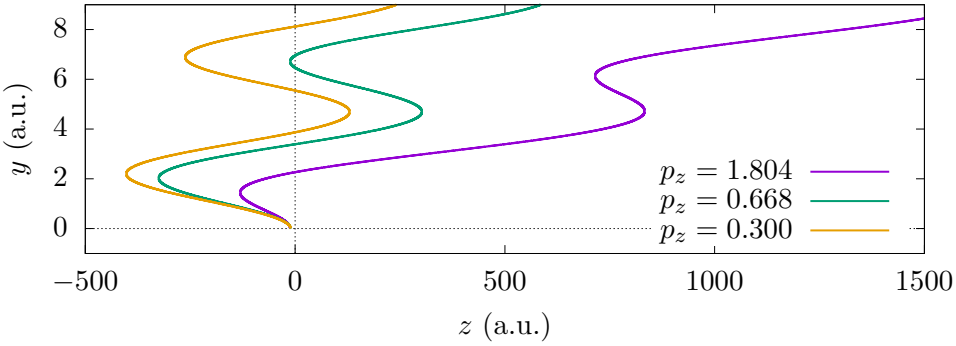

Figure 5.6.: Plain SFA long trajectories in position space in a flat-top laser pulse for small perpendicular momentum $p_y = 0.1$ and different parallel momenta p_z. Note the different scales in z and y direction.

units and the y axis only 10. The initial conditions are the same as in section 5.2. For large parallel momentum the electron leaves the parent ion and passes it once ($z = 0$ and y still small) before leaving for good. For small p_z the electron passes the parent ion several times as mentioned above. In between there is a threshold momentum (here at $p_z \approx 0.668$) where the electron passes the parent ion once and then visits it again with very small velocity. It has been shown [24, 72] that these trajectories are generating the LES. A quantitative comparison of the threshold momentum found here and the boundaries observed in figure 5.5 is however not meaningful, since here a flat-top pulse has been used instead of a finite pulse, and no Coulomb effects are included. Taking both into account as in [72] is possible and yields the positions of the LES in momentum space. Yet this mechanism explains how the observed sharp boundaries emerge.

Thus disregarding the central part of figure 5.5 we see that in the upper half the trajectories are shifted towards negative momenta in p_y direction whereas in the lower half the shift is positive. The boundary between these domains is however not at zero perpendicular momentum but bent downwards and thus asymmetric with respect to the reflection $p_y \to -p_y$. The inset shows different behavior. First one should note that the color scale spans only one twentieth of that in the main figure, so the response of the short trajectories is much weaker. In the center the behavior of the latter is also chaotic. Apart from that the short trajectories mainly exhibit positive shifts, except for the upper central part where a parabola-shaped part is shifted towards negative p_y. The white vertical stripes in the center of the inset indicate trajectories that end up in bound states and thus never reach the detector (see appendix B.1 on how this is determined).

To understand this asymmetric behavior of the momentum shift we try to disentangle the influence of the two forces acting in that direction, i.e., the Coulomb force and the magnetic part of the Lorentz force. To that end we perform numerical calculations where we switch on only one of these forces and show the same quantity as in figure 5.5. This is shown for the Coulomb force in figure 5.7 and for the

magnetic force in figure 5.8.

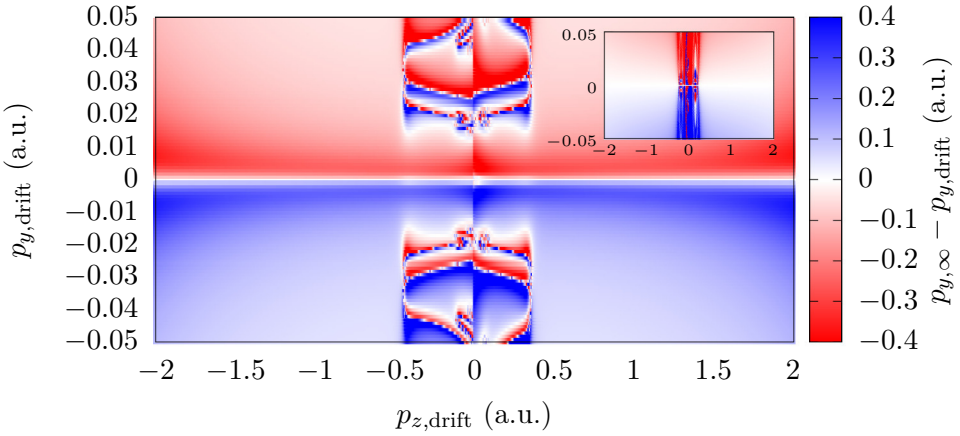

Figure 5.7.: Same as in figure 5.5 but without the magnetic part of the Lorentz force.

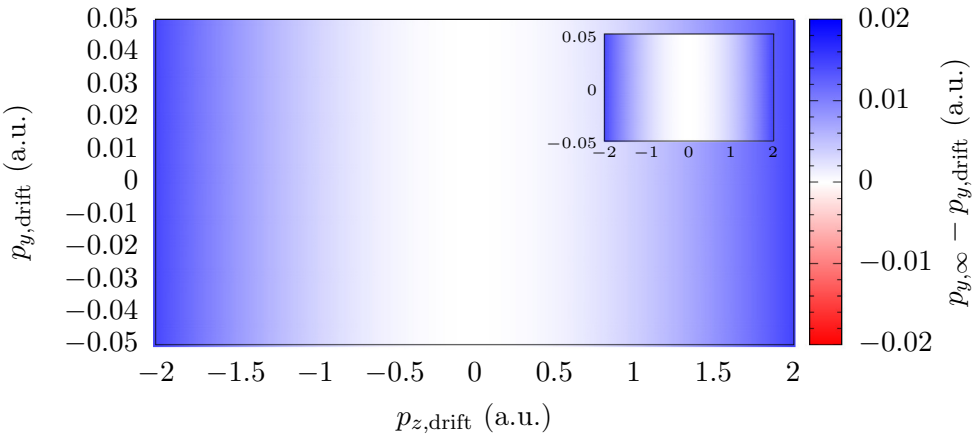

Figure 5.8.: Same as in figure 5.5 but without the Coulomb force. Here the color scale for main figure and inset is identical.

The Coulomb force in figure 5.7 yields the intuitively expected picture. Apart from the chaotic central part the shift is negative in the upper half and positive in the lower half. The boundary is in the center at zero perpendicular momentum. This reflects the attractive nature of the Coulomb potential slowing down electrons that leave the system. It is also much stronger for the long trajectories as these come close the parent ion at least once after the initial tunneling step. The response of the short trajectories is also symmetric, although much weaker.

The shift induced by the magnetic force is presented in figure 5.8. It is much smaller by magnitude than for the Coulomb force. Furthermore the response of long and short trajectories is identical. We observe solely positive shifts which increase with increasing $|p_z|$. This matches the expectations from the picture of *radiation*

pressure due to the $\boldsymbol{v} \times \boldsymbol{B}$ force where the absorption of photons leads to a change of momentum. Faster electrons carry more kinetic energy and thus must have absorbed more photons, i.e., more momentum in propagation direction.

Comparing the figures 5.7 (only the Coulomb force) and 5.5 (both forces) one sees that the latter is very similar to the former but slightly distorted. For the long trajectories the main difference is that the boundary line between the two domains with different sign is bent downwards. It seems that the qualitative behavior of the trajectories is conserved. Under this assumption one can infer from the difference of the two figures that those trajectories originally representing the center of the spectrum now end up at negative momentum in propagation direction. As these trajectories carry most of the weight, the whole spectrum must be shifted. This again matches the numerically observed shift towards negative p_y in figure 5.3 very well, rendering the respective assumption quite plausible.

Further implications from the observations made above are that neither the magnetic force nor the Coulomb force alone can induce shifts in propagation direction which are asymmetric with respect to the reflection $p_y \to -p_y$. This is in line with the conclusions in the literature that the interplay of both forces can lead to counterintuitive shifts against propagation direction. This interplay will be analyzed and disentangled in the next section with the help of model calculations in the spirit of the SMT.

5.4. Semi-Analytical Model Calculations

In this section we build a simplified perturbative model similar to the SMT to reproduce the spectral shift visualized in figure 5.5. Following the argumentation in section 5.3 we treat this quantity as a significant signature of the non-dipole effects considered in this chapter.

Our model is based on the plain-SFA trajectories following the EOM (5.6) but with $\boldsymbol{F} = -\boldsymbol{E}$ only as in section 4.3. This yields analytic expressions for momentum and position by integration,

$$\boldsymbol{p}_0(t) = \boldsymbol{p}_{\text{drift}} + \boldsymbol{A}(t) = \boldsymbol{v}_0(t) \tag{5.25a}$$

$$\boldsymbol{r}_0(t) = \boldsymbol{p}_{\text{drift}}\,(t - t_s) + \int_{t_s}^{t} \mathrm{d}t'\, \boldsymbol{A}(t') + \boldsymbol{r}_{\text{initial}} \tag{5.25b}$$

for which we use the same initial conditions (5.23) as in section 5.2. The ionization time is found from the SPE (5.19). The subscript 0 denotes the *uncorrected* nature of the variables. One example for equation (5.25b) is shown in figure 5.9 (solid black line), along with a graphical representation of the model calculation performed below.

Along these trajectories we want to evaluate the influence of magnetic and Coulomb force. We know that the former basically acts along the whole trajectory while the latter is strongest for small $|\boldsymbol{r}_0(t)|$. Thus we first calculate the momentum change in

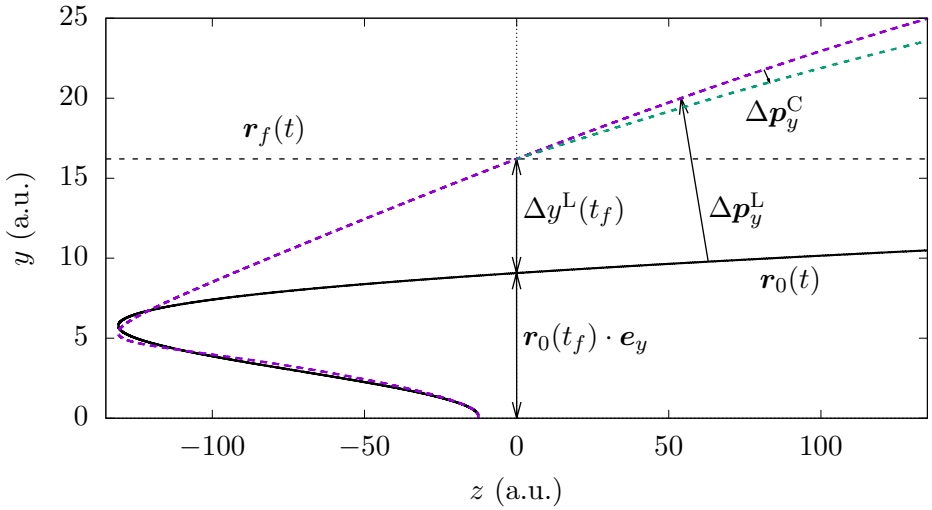

Figure 5.9.: Sketch of the model calculations performed in section 5.4. It shows the unperturbed trajectory $\boldsymbol{r}_0(t)$ (solid black), the perturbatively corrected trajectory $\boldsymbol{r}_0(t) + \boldsymbol{e}_y\Delta y^{\mathrm{L}}(t)$ (dashed violet), the trajectory including the momentum shift from the Coulomb force $\Delta p_y^{\mathrm{C}} = \Delta p_y^{\mathrm{C,flyby}} + \Delta p_y^{\mathrm{C,long\text{-}range}}$ (dashed green) and the flyby trajectory $\boldsymbol{r}_f(t)$ (dashed black). Other important quantities are indicated by arrows and labels, for details see text. Note the different scales in z and y direction.

propagation direction $\boldsymbol{e}_y$ caused by the magnetic force. Starting at the tunnel exit[1] at $\mathrm{Re}\, t_s$, this can be written as

$$\Delta p_y^{\mathrm{L}}(t) = -\int_{\mathrm{Re}\, t_s}^{t} \mathrm{d}t' \; \left[\boldsymbol{v}(t') \times \boldsymbol{B}(\boldsymbol{r}, t')\right] \cdot \boldsymbol{e}_y \,. \tag{5.26}$$

Note that in principle the full trajectory has to be plugged in. However, assuming that the magnetic force is small compared to the electric force (which is reasonable due to the argumentation given in section 5.2) we can plug in the uncorrected trajectory $\boldsymbol{v}_0(t)$ and in this way find a first order perturbative result. Following the same argument we neglect the position dependence in the magnetic field. We thus have to calculate

$$\Delta p_y^{\mathrm{L}}(t) = -\int_{\mathrm{Re}\, t_s}^{t} \mathrm{d}t' \; \left[\boldsymbol{v}_0(t') \times \boldsymbol{B}(t')\right] \cdot \boldsymbol{e}_y \,. \tag{5.27}$$

This can be rewritten using the relation (5.5) between electric and magnetic field, $\boldsymbol{B}(t) = \boldsymbol{e}_x \frac{1}{c} E_z(t)$, the definition of the electric field $\boldsymbol{E}(t) = -\frac{\mathrm{d}}{\mathrm{d}t}\boldsymbol{A}(t)$ and the unper-

[1] We assume that the under-barrier motion is not affected by the magnetic field.

turbed trajectory (5.25a) to read

$$\Delta p_y^{\mathrm{L}}(t) = \frac{1}{c}\int_{\mathrm{Re}\,t_s}^{t} \mathrm{d}t' \; \left(p_{z,\mathrm{drift}} + A_z(t')\right)\left(\frac{\mathrm{d}}{\mathrm{d}t'}A_z(t')\right) . \tag{5.28}$$

Applying integration by parts to the second term yields the expression

$$\Delta p_y^{\mathrm{L}}(t) = \frac{1}{c}\left[p_{z,\mathrm{drift}}A_z(t') + \frac{1}{2}A_z^2(t')\right]_{\mathrm{Re}\,t_s}^{t} \tag{5.29}$$

which can be directly evaluated. Due to $\boldsymbol{A}(t\to\infty) = 0$ the total momentum shift for $t\to\infty$ caused by the magnetic field reads

$$\Delta p_{y,\mathrm{total}}^{\mathrm{L}} = -\frac{1}{c}\left[p_{z,\mathrm{drift}}A_z(\mathrm{Re}\,t_s) + \frac{1}{2}A_z^2(\mathrm{Re}\,t_s)\right] . \tag{5.30}$$

We can determine the induced change of $\boldsymbol{r}_0(t)$ in $\boldsymbol{e}_y$ direction from the momentum shift,

$$\begin{aligned}\Delta y^{\mathrm{L}}(t) &= \int_{\mathrm{Re}\,t_s}^{t} \mathrm{d}t'\, \Delta p_y^{\mathrm{L}}(t') \\ &= \left[\frac{p_{z,\mathrm{drift}}}{c}\alpha(t') + \frac{1}{2c}\alpha^{(2)}(t') + \Delta p_{y,\mathrm{total}}^{\mathrm{L}}\, t'\right]_{\mathrm{Re}\,t_s}^{t} ,\end{aligned} \tag{5.31}$$

where in analogy to equation (2.62)

$$\alpha(t) = \int^t \mathrm{d}t'\, A_z(t') , \quad \alpha^{(2)}(t) = \int^t \mathrm{d}t'\, A_z^2(t') . \tag{5.32}$$

For the $\sin^2$-shaped laser pulse used above this can be evaluated analytically. In figure 5.9 the perturbatively corrected trajectory $\boldsymbol{r}_0(t) + \boldsymbol{e}_y\Delta y^{\mathrm{L}}(t)$ is shown as a violet dashed line.

The conclusion in section 5.3 was that the long trajectories are the ones responsible for the counterintuitive shift of the spectrum against propagation direction. Accordingly we focus on these in our investigations. The main difference between long and short trajectories is that the former pass the parent ion (at least) once before leaving towards the detector whereas the latter do not. It is therefore reasonable to assume that this *flyby* causes the observed qualitative differences. During flyby the distance between electron and parent ion becomes small so that the Coulomb force becomes large. The effect of this flyby on the total momentum in $\boldsymbol{e}_y$ direction can be estimated perturbatively. To that end we assume a linear flyby trajectory

$$\boldsymbol{r}_f(t) = y_f\boldsymbol{e}_y + p_{z,f}(t - t_f)\boldsymbol{e}_z \tag{5.33}$$

with constant distance y_f in $\boldsymbol{e}_y$ direction and constant momentum

$$p_{z,f} = \boldsymbol{p}_0(t_f) \cdot \boldsymbol{e}_z \tag{5.34}$$

in polarization direction $\boldsymbol{e}_z$. The flyby time is defined by

$$\boldsymbol{r}_0(t_f) \cdot \boldsymbol{e}_z = 0\,. \tag{5.35}$$

The flyby trajectory $\boldsymbol{r}_f(t)$ is displayed in figure 5.9 as a black dashed line, coinciding at $z = 0$ with the Lorentz-shifted trajectory $\boldsymbol{r}_0(t) + \boldsymbol{e}_y \Delta y^{\mathrm{L}}(t)$ mentioned above. The Coulomb force $F^{\mathrm{C}}(\boldsymbol{r}) = -\boldsymbol{\nabla} V(\boldsymbol{r})$ can be integrated along $\boldsymbol{r}_f(t)$ to determine the resulting momentum shift in $\boldsymbol{e}_y$ direction,

$$\Delta p_y^{\mathrm{C,flyby}} = -\int_{t_f-\Delta t}^{t_f+\Delta t} \mathrm{d}t\, \frac{y_f}{\left(y_f^2 + p_{z,f}^2 (t-t_f)^2\right)^{3/2}}\,. \tag{5.36}$$

This has to be restricted to a time interval $[t_f - \Delta t, t_f + \Delta t]$ as the accuracy of $\boldsymbol{r}_f(t)$ is only reasonable in a small region around t_f. However, as the denominator of the integrand exhibits a cubic divergence for large $|t - t_f|$, we can assume $\Delta t \to \infty$ without significantly changing the integral. The latter can be solved analytically,

$$\Delta p_y^{\mathrm{C,flyby}} = -y_f \left[\frac{t-t_f}{y_f^2 \sqrt{y_f^2 + p_{z,f}^2 (t-t_f)^2}}\right]_{t_f-\Delta t}^{t_f+\Delta t} \tag{5.37}$$

$$= -\frac{2\Delta t}{y_f \sqrt{y_f^2 + p_{z,f}^2 \Delta t^2}}\,, \tag{5.38}$$

which condenses to a very simple result when taking the limit $\Delta t \to \infty$,

$$\Delta p_y^{\mathrm{C,flyby}} = -\frac{2}{y_f \sqrt{p_{z,f}^2}}\,. \tag{5.39}$$

The distance y_f at flyby time is taken from the Lorentz-shifted trajectory,

$$y_f = \boldsymbol{r}_0(t_f) \cdot \boldsymbol{e}_y + \Delta y^{\mathrm{L}}(t_f)\,. \tag{5.40}$$

For this and the flyby momentum (5.34) we need the flyby time t_f. This can only be found numerically or graphically due to the transcendental nature of the respective equation (5.35).

In addition to the considerations above we can estimate the effect of the long-range Coulomb potential on the final momentum by a simple calculation. Assuming that only the kinetic energy of the electron is affected without any change in direction we can write the final kinetic energy as the initial kinetic (drift) energy plus the

(negative) potential energy at the tunnel exit, which yields for the final momentum

$$|\boldsymbol{p}_{\text{fin}}| = \sqrt{\boldsymbol{p}_{\text{drift}}^2 + 2V(\boldsymbol{r}_0(\operatorname{Re} t_s))}\,. \tag{5.41}$$

This amounts to a change of momentum in propagation direction,

$$\Delta p_y^{\text{C,long-range}} = \left(\frac{\sqrt{\boldsymbol{p}_{\text{drift}}^2 + 2V(\boldsymbol{r}_0(\operatorname{Re} t_s))}}{\sqrt{\boldsymbol{p}_{\text{drift}}^2}} - 1 \right) p_{y,\text{drift}}\,. \tag{5.42}$$

Taking all changes of momentum calculated above into account, we arrive at the final expression for the total momentum change due to magnetic field and Coulomb potential,

$$\Delta p_y^{\text{total}} = \Delta p_{y,\text{total}}^{\text{L}} + \Delta p_y^{\text{C,flyby}} + \Delta p_y^{\text{C,long-range}}\,. \tag{5.43}$$

This equation can now be evaluated on the same momentum grid as used for figure 5.5. We select the most important ionization time t_s corresponding to a long trajectory and calculate the first return time t_f. The resulting total momentum shift $\Delta p_y^{\text{total}}$ is shown in figure 5.10.

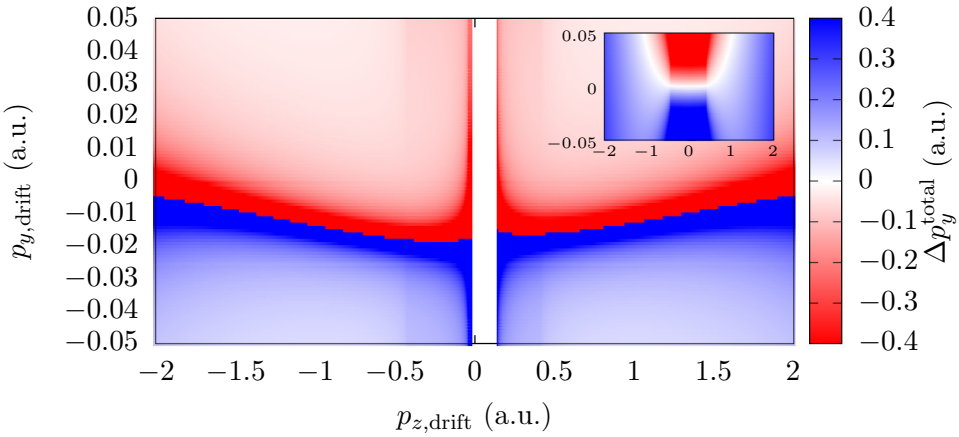

Figure 5.10.: Same as figure 5.5, but calculated from equation (5.43) instead of a full numerical propagation. The main figure shows the shift for long trajectories (assuming one flyby). The missing part for small positive momenta is caused by trajectories which do not complete their flyby during the pulse. The inset shows the momentum shift corresponding to short trajectories (no flyby, so $\Delta p_y^{\text{C,flyby}} = 0$). The color scale for the inset spans only one twentieth of that in the main figure.

As for figure 5.5 we select trajectories with $\operatorname{Re} t_s$ within one optical cycle around the center of the pulse as illustrated in figure 5.4. Apart from the central part which looks different figure 5.10 can be directly compared to the numerically obtained shift

in figure 5.5. Multiple returns are not included in the model so the chaotic behavior in the center is not at all reproduced. The missing (blank) part for small $|p_{z,\mathrm{drift}}|$ is a signature of trajectories which do not complete their flyby before the end of the pulse. This happens due to the finite pulse envelope. After the center of the pulse the amplitude of the vector potential, and thus the oscillation amplitude of the electrons, decreases rapidly (cf. figure 5.4). For electrons with small drift momenta this leads to the phenomenon that the oscillation dies away before a flyby happens. After the pulse is over, these electrons slowly drift past the ion instead of a fast laser-driven flyby. As this is qualitatively different from what we assume for our model, we do not take those trajectories into account.

For larger $|p_{z,\mathrm{drift}}|$ the agreement between figures 5.5 and 5.10 is good. The boundary between positive and negative shift is much sharper in the model calculations. This can be attributed to the large scattering angles up to 180° included in the numerical propagation but not in the model calculations where we always assume a linear flyby. The position of this boundary however is reproduced with good accuracy. This allows us to conclude that our simple model captures the main mechanism responsible for the shift of the spectra in negative propagation direction.

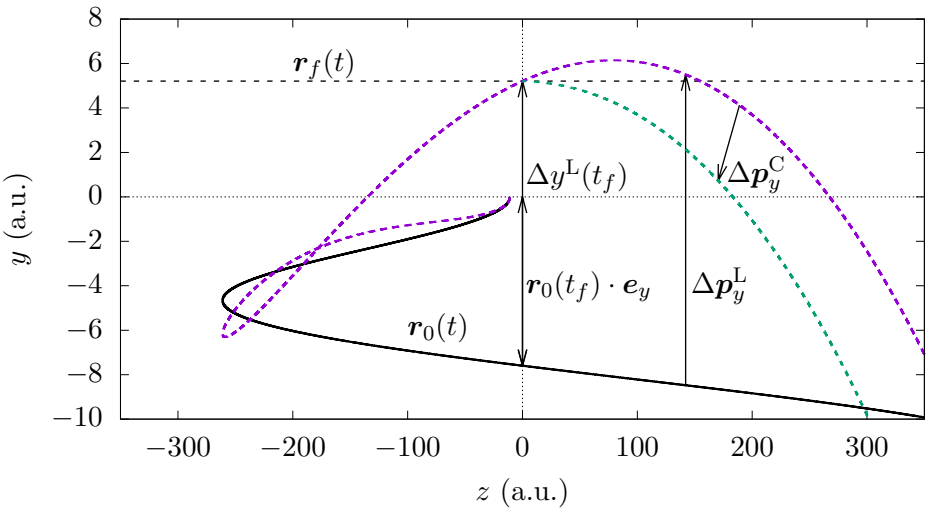

Figure 5.11.: Same as in figure 5.9 but for different initial momentum. It illustrates how a trajectory with negative initial momentum can be scattered into the lower half of the momentum plane due to radiation pressure.

The inset of figure 5.10 shows the shift for short trajectories with $\Delta p_y^{\mathrm{C,flyby}} = 0$. Note that the color scale for the inset only spans one twentieth of that in the main figure, so the observed shift is much smaller. The structure seen in the inset of figure 5.5 is qualitatively reproduced due to the estimate for the long-range Coulomb shift $\Delta p_y^{\mathrm{C,long\text{-}range}}$. Without this only the radiation pressure would be present, the effect of which is shown in figure 5.8. On the other hand, for the long trajectories the long-range Coulomb shift is negligible as it is by far dominated by the flyby

shift $\Delta p_y^{\mathrm{C,flyby}}$.

Finally we can use our model to visualize how trajectories can be shifted towards negative p_y despite negative initial $p_{y,\mathrm{drift}}$. This is illustrated in figure 5.11 where we see a trajectory with initially negative drift momentum in propagation direction. Without the influence of the magnetic force (black line) it passes the ion at negative y which would lead to $\Delta p_y^{\mathrm{C,flyby}} > 0$. However, due to the magnetic force the flyby is shifted to positive y (violet dashed line), which in turn inverses the effect of the flyby, $\Delta p_y^{\mathrm{C,flyby}} < 0$. We can conclude that this mechanism leads to the counterintuitive spectral shift discussed in this chapter.

5.5. Conclusions

In this chapter we analyzed how non-dipole effects can influence photoelectron spectra even for non-relativistic laser parameters. We focused on counterintuitive shifts of final photoelectron momenta against the laser propagation direction as observed in previous experiments [8, 9]. These shifts were reproduced by a full numerical solution of the equations of motion including both Coulomb potential and magnetic Lorentz force. Furthermore we found that the underlying effects can be explained within a simplified semi-analytical model where both forces are included perturbatively. To that end first the momentum shift due to the magnetic Lorentz force is evaluated along the unperturbed trajectory, followed by a perturbative Coulomb correction. The latter is based on the observation that mainly the long trajectories show counterintuitive behavior. Accordingly the momentum shift due to the Coulomb force is evaluated along an approximated flyby trajectory including the positional shift induced by the Lorentz force. Doing so we confirmed that the mechanism leading to the counterintuitive shifts is indeed the modification of soft recollisions by the radiation pressure.

These results show that trajectory-based methods like the TCSFA can easily be adapted to include non-dipole effects. As in the previous chapters this allows for intuitive interpretations in terms of trajectories and thus leads to better understanding of the underlying physics. In contrast to classical simulations the TCSFA also includes interference effects and can thus be applied to a wide range of problems depending on those, e.g. holographic imaging or the retrieval of structural information from interference patterns.

6. Final Remarks

In this thesis we demonstrated how the trajectory-based strong field approximation (SFA) can be extended to reproduce different effects that are otherwise inaccessible to the plain SFA.

In chapter 3 we adapted the trajectory-based Coulomb-corrected strong field approximation (TCSFA) to include the collective field of a laser-driven metal cluster for the electron propagation to analyze the emission of highly energetic electrons. We found that long trajectories, when passing the cluster in phase with the oscillation of the valence electron cloud, can acquire final momenta far beyond the expected cutoff.

Another phenomenon beyond the scope of the plain SFA was presented in chapter 4 where we analyzed the unexpectedly high yield around the $2U_\mathrm{p}$ cutoff for certain parameters found in numerical solutions of the time-dependent Schrödinger equation (TDSE) and experimentally acquired photoelectron spectra (PES) but not reproduced by the SFA. We showed that by scaling the TDSE this behavior can be described by two dimensionless parameters governing both the appearance of a plateau structure as well as the difference to the plain SFA result. To incorporate this effect into the trajectory-based SFA we developed a complex Coulomb correction based on the same ideas as already used in the 1960s. The occurring problem of branch cuts in the complex time plane was solved by using the analytically known electron trajectories to find a valid integration path. Doing so we found that the weight of a single trajectory is (within this framework) determined by the full propagation up to the detector instead of just up to the tunnel exit, thus putting the whole concept of a tunnel exit into perspective.

In the last chapter 5 we demonstrated how non-dipole effects can be included into the TCSFA to analyze experimentally observed counterintuitive momentum shifts against the laser propagation direction. We incorporated the magnetic Lorentz force into the electron propagation using relativistically corrected equations of motion and so qualitatively reproduced the experimental findings. We further showed that the effect of counterintuitive shifts against propagation direction can be explained within a simplified semi-analytical model where the magnetic Lorentz force and the Coulomb potential where included successively in a perturbative way. By that we confirmed that the observed effect is caused by soft recollisions which are modified due to the radiation pressure.

In conclusion we have shown the trajectory-based SFA to be a versatile tool in gaining additional understanding of the underlying physical mechanisms for very different effects in strong-field physics. Thanks to its derivation from the TDSE the SFA itself already incorporates many effects found in strong-field physics. Its formu-

lation in terms of trajectories allows for intuitive explanations and detailed analysis of the latter. Additionally it gives us the opportunity to incorporate external potentials or modify the equations of motion to analyze effects beyond the scope of the plain SFA, as demonstrated in the previous chapters. Thanks to this flexibility it can be applied not only to single atoms but also to molecules or clusters, as long as the single active electron approximation is justified. In contrast to classical simulations the trajectory-based SFA contains interference effects and hence can even be applied to problems like holographic imaging or structural analysis where information about the interior of an object is reconstructed from interference patterns.

However, there are still open problems to be solved. The most prominent one is the applicability of the complex Coulomb correction for quantitative comparisons with ab initio or experimental data. For this to be possible one would have to circumvent the divergence for head-on recollisions and lift the dependence of the result on the upper integration limit, as discussed in section 4.4. A possible solution to this could be an effective treatment of the recollisions incorporated into the real propagation used in chapters 3 and 5.

Further applications of the methods presented here could include the analysis of interference patterns from diatomic (or more complex) molecules [55]. On the other hand one could stay with single atoms as the target and consider more complex laser fields, like bichromatic pulses with varying phase difference [73].

A. Derivations

A.1. Force Between Two Overlapping Oppositely Charged Spheres

The following derivation was already published in [39]. It is reproduced here in slightly more detail for the sake of completeness.

The rigid-sphere model (RSM) consists of two homogeneously charged spheres with equal radii R and opposite charges. Here we assume one valence electron per atom, but the model can easily be adapted to other cases. To describe the dynamics of this system we need to know the electrostatic force between the spheres. Due to the underlying physical situation that is to be modeled we assume the spheres always overlap. We start with the force exerted on a charge distribution $\rho_1(\boldsymbol{r}')$ by a potential $\Phi_2(\boldsymbol{r}-\boldsymbol{r}')$ depending on the relative distance $\boldsymbol{r}$,

$$\boldsymbol{F}(\boldsymbol{r}) = -\int \rho_1(\boldsymbol{r}')\boldsymbol{\nabla}_{\boldsymbol{r}}\Phi_2(\boldsymbol{r}-\boldsymbol{r}')\mathrm{d}^3r' \,. \tag{A.1}$$

The divergence of this force is

$$\boldsymbol{\nabla}_{\boldsymbol{r}} \cdot \boldsymbol{F}(\boldsymbol{r}) = -\int \rho_1(\boldsymbol{r}')\Delta_{\boldsymbol{r}}\Phi_2(\boldsymbol{r}-\boldsymbol{r}')\mathrm{d}^3r' \tag{A.2}$$

where we can plug in Poisson's equation

$$\begin{aligned} \Delta_{\boldsymbol{r}}\Phi_2(\boldsymbol{r}-\boldsymbol{r}') &= \Delta_{\boldsymbol{r}-\boldsymbol{r}'}\Phi_2(\boldsymbol{r}-\boldsymbol{r}') && \text{(A.3)} \\ &= -4\pi\rho_2(\boldsymbol{r}-\boldsymbol{r}') && \text{(A.4)} \end{aligned}$$

with $\rho_2(\boldsymbol{r})$ being the generating charge density for the potential $\Phi_2(\boldsymbol{r})$. This results in the overlap integral

$$\boldsymbol{\nabla}_{\boldsymbol{r}} \cdot \boldsymbol{F}(\boldsymbol{r}) = 4\pi \int \rho_1(\boldsymbol{r}')\rho_2(\boldsymbol{r}-\boldsymbol{r}')\mathrm{d}^3r' \tag{A.5}$$

between the two charge distributions. For point charges this leads to Coulomb's law. Here we need to define the charge distributions of the homogeneously charged spheres as $\rho_1(\boldsymbol{r}) = -n_0\Theta(R-|\boldsymbol{r}|)$ (electron sphere) and $\rho_2(\boldsymbol{r}) = n_0\Theta(R-|\boldsymbol{r}|)$ (ion sphere) with the particle density n_0 and the Heaviside step function

$$\Theta(x) = \begin{cases} 0 & \text{for } x < 0 \\ 1 & \text{for } x \geq 0 \end{cases} . \tag{A.6}$$

Note that in atomic units the electron charge is -1. Plugging the charge distributions as defined above into the overlap integral leads to

$$\begin{aligned} \boldsymbol{\nabla}_{\boldsymbol{r}} \cdot \boldsymbol{F}(\boldsymbol{r}) &= -4\pi n_0^2 \int \Theta(R-|\boldsymbol{r}'|)\Theta(R-|\boldsymbol{r}-\boldsymbol{r}'|)\mathrm{d}^3r' && \text{(A.7)} \\ &= -4\pi n_0^2\, 2V && \text{(A.8)} \end{aligned}$$

where V is the volume of a spherical cap

$$V = \frac{\pi h^2}{3}(3R - h) \tag{A.9}$$

with $h = |\boldsymbol{r}|/2$ being the height of the cap. This holds as long as $|r| < 2R$, i.e., as long as the spheres overlap. Thus with $r = |\boldsymbol{r}|$ we find for the gradient of the force

$$\boldsymbol{\nabla}_{\boldsymbol{r}} \cdot \boldsymbol{F}(\boldsymbol{r}) = -4\pi n_0^2 \frac{4\pi R^3}{3}\left(1 - \frac{3}{4}\frac{r}{R} + \frac{1}{16}\frac{r^3}{R^3}\right) \tag{A.10}$$

which only depends on r but not on the direction. Accordingly the motion is restricted to one dimension and we can write the left-hand side as

$$\boldsymbol{\nabla}_{\boldsymbol{r}} \cdot \boldsymbol{F}(\boldsymbol{r}) = \frac{1}{r^2}\frac{\partial}{\partial r}\left[r^2 F_r(\boldsymbol{r})\right] \tag{A.11}$$

where $F_r(\boldsymbol{r})$ is the radial component of $\boldsymbol{F}(\boldsymbol{r})$. This can now be calculated,

$$F_r(\boldsymbol{r}) = \frac{1}{r^2}\int^r \mathrm{d}r' r'^2 \boldsymbol{\nabla}_{\boldsymbol{r}'} \cdot \boldsymbol{F}(\boldsymbol{r}') \tag{A.12}$$

$$= -4\pi n_0^2 \frac{4\pi R^3}{3}\frac{1}{r^2}\int^r \mathrm{d}r' r'^2 \left(1 - \frac{3}{4}\frac{r'}{R} + \frac{1}{16}\frac{r'^3}{R^3}\right) \tag{A.13}$$

$$= -\frac{4\pi n_0}{3}\frac{4\pi n_0 R^3}{3}\left(r - \frac{9}{16}\frac{r^2}{R} + \frac{1}{32}\frac{r^4}{R^3}\right), \tag{A.14}$$

or, using $\boldsymbol{F}(\boldsymbol{r}) = F_r(\boldsymbol{r})\frac{\boldsymbol{r}}{|\boldsymbol{r}|}$,

$$\boldsymbol{F}(\boldsymbol{r}) = -\frac{4\pi n_0}{3}\frac{4\pi n_0 R^3}{3}\left(\boldsymbol{r} - \frac{9}{16R}\boldsymbol{r}\,|\boldsymbol{r}| + \frac{1}{32R^3}\boldsymbol{r}\,|\boldsymbol{r}|^3\right). \tag{A.15}$$

To determine the equation of motion we fix the ion sphere in the origin and replace $\boldsymbol{r}$ by the displacement $\boldsymbol{d}$. As we want to know the motion of the electron sphere we use

$$\boldsymbol{F} = M\ddot{\boldsymbol{d}} \tag{A.16}$$

$$= \frac{4\pi n_0 R^3}{3}\ddot{\boldsymbol{d}} \tag{A.17}$$

and the Mie frequency

$$\omega_{\mathrm{Mie}} = \sqrt{\frac{4\pi n_0}{3}} \tag{A.18}$$

from section 3.2 to find the final result

$$\ddot{\boldsymbol{d}} = -\omega_{\mathrm{Mie}}^2 \left(\boldsymbol{d} - \frac{9}{16R} \boldsymbol{d} \left| \boldsymbol{d} \right| + \frac{1}{32R^3} \boldsymbol{d} \left| \boldsymbol{d} \right|^3 \right) . \tag{A.19}$$

A.2. Interaction Matrix Element $\langle \boldsymbol{k}|\hat{\boldsymbol{r}}\cdot\boldsymbol{E}|\Psi_0\rangle$

For the evaluation of the strong field approximation (SFA) matrix element in section 2.2 we need the matrix element $\langle \boldsymbol{k}|\hat{\boldsymbol{r}}\cdot\boldsymbol{E}(t)|\Psi_0\rangle$. It can be calculated as follows,

$$\langle \boldsymbol{k}|\hat{\boldsymbol{r}}\cdot\boldsymbol{E}(t)|\Psi_0\rangle = \mathrm{i}\boldsymbol{\nabla}_{\boldsymbol{k}}\langle \boldsymbol{k}|\Psi_0\rangle\cdot\boldsymbol{E}(t)\,, \tag{A.20}$$

where we used that the representation of the position operator in momentum space is $\hat{\boldsymbol{r}} = \mathrm{i}\boldsymbol{\nabla}_{\boldsymbol{k}}$. For this we need $\langle \boldsymbol{k}|\Psi_0\rangle$ which is the ground state wave function projected into momentum space. We start from the ground state wave function of hydrogen in position space and SI units,

$$\Psi_0(r) = \frac{1}{\sqrt{\pi}a_0^{3/2}}\mathrm{e}^{-r/a_0}\,, \tag{A.21}$$

where a_0 is the Bohr radius. Its projection into momentum space is calculated via a Fourier transform,

$$\langle \boldsymbol{p}|\Psi_0\rangle = \frac{1}{(2\pi\hbar)^{3/2}}\int_{\mathbb{R}^3}\mathrm{d}^3r\,\mathrm{e}^{-\mathrm{i}\boldsymbol{p}\cdot\boldsymbol{r}/\hbar}\Psi_0(r) \tag{A.22}$$

$$= \frac{1}{(2\pi\hbar)^{3/2}}\frac{1}{\sqrt{\pi}a_0^{3/2}}\int_{\mathbb{R}^3}\mathrm{d}^3r\,\mathrm{e}^{-\mathrm{i}\boldsymbol{p}\cdot\boldsymbol{r}/\hbar - r/a_0}\,, \tag{A.23}$$

and in spherical coordinates with $\mathrm{d}^3r = r^2\mathrm{d}r\,\sin\vartheta\mathrm{d}\vartheta\,\mathrm{d}\varphi$,

$$\langle \boldsymbol{p}|\Psi_0\rangle = \frac{1}{(2\pi\hbar)^{3/2}}\frac{1}{\sqrt{\pi}a_0^{3/2}}\int_0^\infty \mathrm{d}r\,r^2\int_0^\pi \mathrm{d}\vartheta\,\sin\vartheta\int_0^{2\pi}\mathrm{d}\varphi\,\mathrm{e}^{-\mathrm{i}rp\cos\vartheta/\hbar - r/a_0} \tag{A.24}$$

$$= \frac{1}{(2\pi\hbar)^{3/2}}\frac{2\pi}{\sqrt{\pi}a_0^{3/2}}\int_0^\infty \mathrm{d}r\,r^2\int_0^\pi \mathrm{d}\vartheta\,\sin\vartheta\mathrm{e}^{-\mathrm{i}rp\cos\vartheta/\hbar - r/a_0}\,, \tag{A.25}$$

and using $\sin\vartheta\mathrm{d}\vartheta = \mathrm{d}\cos\vartheta$,

$$\langle \boldsymbol{p}|\Psi_0\rangle = \frac{1}{(2\pi\hbar)^{3/2}}\frac{2\pi}{\sqrt{\pi}a_0^{3/2}}\int_1^{-1}\mathrm{d}\cos\vartheta\int_0^\infty \mathrm{d}r\,r^2\mathrm{e}^{-r(\mathrm{i}p\cos\vartheta/\hbar + 1/a_0)}\,. \tag{A.26}$$

The integral over r can be solved by using $\int_0^\infty \mathrm{d}x\,x^n\mathrm{e}^{-x} = n!$,

$$\langle \boldsymbol{p}|\Psi_0\rangle = \frac{1}{(2\pi\hbar)^{3/2}}\frac{2\pi}{\sqrt{\pi}a_0^{3/2}}\int_1^{-1}\mathrm{d}\cos\vartheta\,\frac{2}{(-\mathrm{i}\frac{p\cos\vartheta}{\hbar} - \frac{1}{a_0})^3} \tag{A.27}$$

$$= \frac{1}{(2\pi\hbar)^{3/2}}\frac{2\pi}{\sqrt{\pi}a_0^{3/2}}\frac{\hbar}{-\mathrm{i}p}\frac{4\frac{-\mathrm{i}p}{\hbar a_0}}{\left(\frac{p^2}{\hbar^2} + \frac{1}{a_0^2}\right)^2} \tag{A.28}$$

$$= \frac{2^{3/2}\hbar^{5/2}}{a_0^{5/2}}\frac{1}{\pi\left(p^2 + \frac{\hbar^2}{a_0^2}\right)^2}\,. \tag{A.29}$$

From the solution of the Schrödinger equation we know that

$$E_n = -\frac{e^2}{4\pi\varepsilon_0}\frac{Z^2}{2a_0 n^2} \tag{A.30}$$

with

$$a_0 = \frac{4\pi\varepsilon_0\hbar^2}{m_e e^2}\,. \tag{A.31}$$

For hydrogen in the ground state ($Z = 1$, $n = 1$ and so $I_\mathrm{p} = -E_1$) follows

$$\frac{\hbar}{a_0} = \sqrt{2I_\mathrm{p} m_e} \tag{A.32}$$

and thus

$$\langle \boldsymbol{p}|\Psi_0\rangle = 2^{3/2}(2I_\mathrm{p} m_\mathrm{e})^{5/4}\frac{1}{\pi\left(p^2 + 2I_\mathrm{p} m_\mathrm{e}\right)^2}\,. \tag{A.33}$$

Hence

$$\langle \boldsymbol{k}|\hat{\boldsymbol{r}}\cdot\boldsymbol{E}(t)|\Psi_0\rangle = -\mathrm{i}2^{7/2}(2I_\mathrm{p})^{5/4}\frac{\boldsymbol{k}\cdot\boldsymbol{E}(t)}{\pi(k^2 + 2I_\mathrm{p})^3}\,. \tag{A.34}$$

A.3. Saddle-Point Approximation

The problem considered here is an integral of the form

$$M = \int_{x_a}^{x_b} \mathrm{d}x\, f(x) \mathrm{e}^{\lambda S(x)} \tag{A.35}$$

which needs to be approximated. This shall be briefly sketched here for the case of real variables where this approximation is known as Laplace's method. For contour integrals with complex variables the mathematical details are more involved, however, the basic idea is similar, which is the reason for presenting the following derivation. Details can be found in [17], the standard reference is [74].

Here we assume that $\lambda S(x)$ is a function that has a maximum at $S'(x_s) = 0$, $S''(x_s) < 0$. The case of a single maximum is discussed, the extension towards multiple maxima is straightforward. We expand the exponent $\lambda S(x)$ around the maximum x_s,

$$\lambda S(x) = \lambda S(x_s) + \frac{\partial}{\partial x} \lambda S(x) \bigg|_{x=x(s)} (x - x_s) + \frac{1}{2} \frac{\partial^2}{\partial x^2} \lambda S(x) \bigg|_{x=x(s)} (x - x_s)^2 + \dots \tag{A.36}$$

$$= \lambda S(x_s) + \frac{1}{2} \lambda S''(x_s)(x - x_s)^2 + \dots \tag{A.37}$$

where the second term vanishes due to $S'(x_s) = 0$. The exponential term can thus be written as

$$\mathrm{e}^{\lambda S(x)} \approx \mathrm{e}^{\lambda S(x_s)} \mathrm{e}^{\frac{1}{2} \lambda S''(x_s)(x - x_s)^2} \tag{A.38}$$

and assuming that $f(x)$ changes slowly with x, we can expand the whole integrand as

$$f(x) \mathrm{e}^{\lambda S(x)} \approx f(x_s) \mathrm{e}^{\lambda S(x_s)} \mathrm{e}^{\frac{1}{2} \lambda S''(x_s)(x - x_s)^2} \,. \tag{A.39}$$

Plugging this into the integral above we find

$$M \approx f(x_s) \mathrm{e}^{\lambda S(x_s)} \int_{x_a}^{x_b} \mathrm{d}x\, \mathrm{e}^{\frac{1}{2} \lambda S''(x_s)(x - x_s)^2} \,. \tag{A.40}$$

The limits of the integral can be extended towards $\pm\infty$ as the exponent in the integrand $\frac{1}{2} \lambda S''(x_s)(x - x_s)^2$ decreases rapidly for increasing $|x - x_s|$ due to $S''(x_s) < 0$. This yields a Gaussian integral which can be solved analytically,

$$M \approx f(x_s) \mathrm{e}^{\lambda S(x_s)} \int_{-\infty}^{\infty} \mathrm{d}x\, \mathrm{e}^{\frac{1}{2} \lambda S''(x_s)(x - x_s)^2} \tag{A.41}$$

$$\approx f(x_s) \mathrm{e}^{\lambda S(x_s)} \sqrt{\frac{2\pi}{-\lambda S''(x_s)}} \,. \tag{A.42}$$

For complex variables the simple one-dimensional integral becomes a contour integral and the maxima x_s are replaced by saddle points. In the special case of the strong field approximation (SFA) (section 2.3) the prefactor $f(x)$ vanishes at $x = x_s$ which calls for special treatment as well. This is discussed in detail in [17], the results obtained there are used in section 2.3.

A.4. Complex Coulomb Correction in First Order

There are different possibilities how to include corrections for external potentials (e.g. the Coulomb potential) into the strong field approximation (SFA). One basically ad-hoc method is the trajectory-based Coulomb-corrected strong field approximation (TCSFA) demonstrated in chapter 3 where the tunneling step is separated from the real-time propagation while only the latter is modified to include an external potential. Here we want to give a derivation for a perturbative Coulomb correction of the plain SFA trajectories in first order of the ion charge Z. It is based on section 6.2.1 of [18] but comes to slightly different conclusions. The basic ideas applied here are already used in the derivation of the Coulomb-corrected PPT rate [21].

We start with the action as used in equation (4.11),

$$S_0 = \int_{t_s}^{t_d} \mathrm{d}t \left(\frac{1}{2} [\boldsymbol{p} + \boldsymbol{A}(t)]^2 + I_\mathrm{p} \right) \tag{A.43}$$

$$= \int_{t_s}^{t_d} \mathrm{d}t \left(\frac{1}{2} \boldsymbol{v}_0^2(t) + I_\mathrm{p} \right) \tag{A.44}$$

where $\boldsymbol{v}_0(t)$ denotes the uncorrected trajectory and S_0 the uncorrected action. This now shall be modified to include the Coulomb potential. To do this consistently we need to have a look at the related method of path integrals. There the action is always an integral over a Lagrangian function L which in our case reads

$$L_0 = \frac{1}{2} \boldsymbol{v}_0^2 - \boldsymbol{E} \cdot \boldsymbol{r}_0 \tag{A.45}$$

where the time dependencies have been dropped for brevity. $\boldsymbol{E} = -\frac{\mathrm{d}}{\mathrm{d}t} \boldsymbol{A}$ is the electric field of the laser.

One should note that the same formalism as used below can also be applied to the Hamiltonian function. However, due to differences in the approximations made, the result is different and, at least in our case, not useful at all as it only predicts a field- and momentum-independent shift of the ionization probability. This is discussed in detail in appendix B of [18].

Here the Lagrangian function can be identified in above equation for the action by some identical transformations,

$$S_0 = \int_{t_s}^{t_d} \mathrm{d}t \left(\frac{1}{2} \boldsymbol{v}_0^2(t) + I_\mathrm{p} \right) \tag{A.46}$$

$$= \boldsymbol{r}_0 \cdot \boldsymbol{v}_0 \Big|_{t_s}^{t_d} - \int_{t_s}^{t_d} \mathrm{d}t \left(\frac{1}{2} \boldsymbol{v}_0^2(t) + \dot{\boldsymbol{v}}_0 \cdot \boldsymbol{r}_0 - I_\mathrm{p} \right) \tag{A.47}$$

where for the uncorrected trajectory $\dot{\boldsymbol{v}}_0 = -\boldsymbol{E}$ holds,

$$= \boldsymbol{r}_0 \cdot \boldsymbol{v}_0\Big|_{t_s}^{t_d} - \int_{t_s}^{t_d} \mathrm{d}t \left(\frac{1}{2}\boldsymbol{v}_0^2(t) - \boldsymbol{E}\cdot\boldsymbol{r}_0 - I_\mathrm{p}\right) \tag{A.48}$$

$$= \boldsymbol{r}_0 \cdot \boldsymbol{v}_0\Big|_{t_s}^{t_d} - \int_{t_s}^{t_d} \mathrm{d}t \left(L_0 - I_\mathrm{p}\right) . \tag{A.49}$$

Now we obtain the full action including the Coulomb potential by replacing the uncorrected trajectory $\boldsymbol{r}_0$, $\boldsymbol{v}_0$ by the corrected trajectory $\boldsymbol{r}$, $\boldsymbol{v}$ and the uncorrected Lagrangian $L_0 = T_0 - V_0$ by its full counterpart $L = T - V$ where T is the kinetic energy and V the potential. This results in the full action

$$S = \boldsymbol{r}\cdot\boldsymbol{v}\Big|_{t_s'}^{t_d} - \int_{t_s'}^{t_d} \mathrm{d}t \left(\frac{1}{2}\boldsymbol{v}^2 - \boldsymbol{E}\cdot\boldsymbol{r} + \frac{Z}{\sqrt{\boldsymbol{r}^2}} - I_\mathrm{p}\right) \tag{A.50}$$

which cannot be evaluated directly as the full trajectory $\boldsymbol{r}$, $\boldsymbol{v}$ is unknown. Instead we do a first order expansion in Z by expanding the full trajectory as

$$\boldsymbol{r} = \boldsymbol{r}_0' + \boldsymbol{r}_1 \tag{A.51}$$

$$\boldsymbol{v} = \boldsymbol{v}_0' + \boldsymbol{v}_1 . \tag{A.52}$$

Here the notation is as in chapters 3 and 4, i.e., $\boldsymbol{p}$ denotes the canonical or drift momentum and $\boldsymbol{v}$ the velocity or kinetic momentum. The final canonical momentum $\boldsymbol{p}$ (which is time-independent) of $\boldsymbol{r}$, $\boldsymbol{v}$ is by definition the same as the canonical momentum corresponding to $\boldsymbol{r}_0$. Note that $\boldsymbol{r}_0 \neq \boldsymbol{r}_0'$ and accordingly the canonical momentum $\boldsymbol{p}'$ and ionization time t_s' corresponding to $\boldsymbol{r}_0'$ are different. This is necessary as the term $\boldsymbol{v}_1$ does not vanish at detection time t_d and thus leads to a change in final momentum which can be written as

$$\boldsymbol{p} = \boldsymbol{p}' + \boldsymbol{v}_1(t_d) = \boldsymbol{v}(t_d) . \tag{A.53}$$

$\boldsymbol{r}_0'$, $\boldsymbol{v}_0'$ is termed the zeroth order corrected trajectory and $\boldsymbol{r}_1$, $\boldsymbol{v}_1$ the first order correction. We assume that the latter are proportional to the ion charge, $\boldsymbol{r}_1 \propto Z$,

$\boldsymbol{v}_1 \propto Z$ and $t_s - t_s' \propto Z$. The expanded action reads

$$\begin{aligned} S &= (\boldsymbol{r}_0' + \boldsymbol{r}_1) \cdot (\boldsymbol{v}_0' + \boldsymbol{v}_1)\Big|_{t_s'}^{t_d} \\ &\quad - \int_{t_s'}^{t_d} \mathrm{d}t \left(\frac{1}{2}(\boldsymbol{v}_0' + \boldsymbol{v}_1)^2 - \boldsymbol{E} \cdot (\boldsymbol{r}_0' + \boldsymbol{r}_1) + \frac{Z}{\sqrt{(\boldsymbol{r}_0' + \boldsymbol{r}_1)^2}} - I_\mathrm{p} \right) \qquad \text{(A.54)} \\ &= \boldsymbol{r}_0' \cdot \boldsymbol{v}_0'\Big|_{t_s'}^{t_d} + \boldsymbol{r}_0' \cdot \boldsymbol{v}_1\Big|_{t_s'}^{t_d} + \boldsymbol{r}_1 \cdot \boldsymbol{v}_0'\Big|_{t_s'}^{t_d} \\ &\quad - \int_{t_s'}^{t_d} \mathrm{d}t \left(\frac{1}{2}\boldsymbol{v}_0'^2 + \boldsymbol{v}_0' \cdot \boldsymbol{v}_1 - \boldsymbol{E} \cdot \boldsymbol{r}_0' - \boldsymbol{E} \cdot \boldsymbol{r}_1 + \frac{Z}{\sqrt{(\boldsymbol{r}_0' + \boldsymbol{r}_1)^2}} - I_\mathrm{p} \right) \qquad \text{(A.55)} \\ &= S_0' + \boldsymbol{r}_0' \cdot \boldsymbol{v}_1\Big|_{t_s'}^{t_d} + \boldsymbol{r}_1 \cdot \boldsymbol{v}_0'\Big|_{t_s'}^{t_d} - \int_{t_s'}^{t_d} \mathrm{d}t \left(\boldsymbol{v}_0' \cdot \boldsymbol{v}_1 - \boldsymbol{E} \cdot \boldsymbol{r}_1 + \frac{Z}{\sqrt{(\boldsymbol{r}_0' + \boldsymbol{r}_1)^2}} \right) \qquad \text{(A.56)} \end{aligned}$$

where we neglected terms of quadratic or higher order in Z. S_0' denotes the zeroth order action (A.48) evaluated along the zeroth order corrected trajectory $\boldsymbol{r}_0'$. The term $\boldsymbol{v}_0' \cdot \boldsymbol{v}_1$ under the integral can be integrated by parts, yielding

$$\begin{aligned} \int_{t_s'}^{t_d} \mathrm{d}t\, \boldsymbol{v}_0' \cdot \boldsymbol{v}_1 &= \boldsymbol{v}_0' \cdot \boldsymbol{r}_1\Big|_{t_s'}^{t_d} - \int_{t_s'}^{t_d} \mathrm{d}t\, \dot{\boldsymbol{v}}_0' \cdot \boldsymbol{r}_1 \qquad \text{(A.57)} \\ &= \boldsymbol{v}_0' \cdot \boldsymbol{r}_1\Big|_{t_s'}^{t_d} + \int_{t_s'}^{t_d} \mathrm{d}t\, \boldsymbol{E} \cdot \boldsymbol{r}_1 \qquad \text{(A.58)} \end{aligned}$$

which can be plugged into the action (A.56). Thus we have

$$S = S_0' + \boldsymbol{r}_0' \cdot \boldsymbol{v}_1\Big|_{t_s'}^{t_d} - \int_{t_s'}^{t_d} \mathrm{d}t\, \frac{Z}{\sqrt{(\boldsymbol{r}_0' + \boldsymbol{r}_1)^2}}\,. \qquad \text{(A.59)}$$

The Coulomb integral can be simplified when expanding the integrand,

$$\frac{Z}{\sqrt{(\boldsymbol{r}_0' + \boldsymbol{r}_1)^2}} = \frac{Z}{\sqrt{\boldsymbol{r}_0'^2}} - \frac{Z\boldsymbol{r}_0'}{\boldsymbol{r}_0'^{3/2}} \cdot \boldsymbol{r}_1 + \mathcal{O}\left(Z^3\right) \qquad \text{(A.60)}$$

where we need to keep only the first term as already the second term is quadratic in Z. Additionally we want to evaluate this integral along $\boldsymbol{r}_0$ instead of $\boldsymbol{r}_0'$. To that

end we write

$$\begin{aligned}
\boldsymbol{r}_0'(t) &= \int_{t_s'}^{t} \mathrm{d}\tau\, [\boldsymbol{p}' + \boldsymbol{A}(\tau)] \\
&= \boldsymbol{p}'(t - t_s') + \int_{t_s'}^{t} \mathrm{d}\tau\, \boldsymbol{A}(\tau) \\
&= \boldsymbol{p}(t - t_s') - (\boldsymbol{p} - \boldsymbol{p}')(t - t_s') + \int_{t_s}^{t} \mathrm{d}\tau\, \boldsymbol{A}(\tau) + \int_{t_s'}^{t_s} \mathrm{d}\tau\, \boldsymbol{A}(\tau) \\
&= \boldsymbol{p}(t - t_s) + \boldsymbol{p}(t_s - t_s') - (\boldsymbol{p} - \boldsymbol{p}')(t - t_s') + \int_{t_s}^{t} \mathrm{d}\tau\, \boldsymbol{A}(\tau) + \int_{t_s'}^{t_s} \mathrm{d}\tau\, \boldsymbol{A}(\tau) \\
&= \boldsymbol{r}_0(t) + \boldsymbol{p}(t_s - t_s') - (\boldsymbol{p} - \boldsymbol{p}')(t - t_s') + \int_{t_s'}^{t_s} \mathrm{d}\tau\, \boldsymbol{A}(\tau) \\
&= \boldsymbol{r}_0(t) + \mathcal{O}(Z)
\end{aligned} \tag{A.61}$$

where we also used that

$$\int_{t_s'}^{t_s} \mathrm{d}\tau \approx t_s - t_s' \propto Z\,. \tag{A.62}$$

Following this argumentation we can write the action (A.59) as

$$S = S_0' + \boldsymbol{r}_0' \cdot \boldsymbol{v}_1\Big|_{t_s'}^{t_d} - \int_{t_s}^{t_d} \mathrm{d}t\, \frac{Z}{\sqrt{\boldsymbol{r}_0^2}}\,. \tag{A.63}$$

For the sake of completeness one has to take care of the boundary conditions. As we set $\boldsymbol{r}_0(t_s) = \boldsymbol{r}_0'(t_s') = 0$, replacing the lower limit of the time integrals is nontrivial due to the occurring divergence. However, since this divergence at the lower boundary is lifted using a matching procedure (see appendix A.5), it is simply neglected here. To remove the dependence of S_0' on the zeroth order corrected trajectory we expand $S_0' = S_0(\boldsymbol{p}', t_s')$ around $\boldsymbol{p}$ and t_s,

$$S_0(\boldsymbol{p}', t_s') \approx S_0(\boldsymbol{p}, t_s) + \frac{\partial S_0}{\partial t_s}\bigg|_{\boldsymbol{p},t_s} (t_s' - t_s) + \frac{\partial S_0}{\partial \boldsymbol{p}}\bigg|_{\boldsymbol{p},t_s} (\boldsymbol{p}' - \boldsymbol{p})\,. \tag{A.64}$$

The time derivative of S_0 vanishes at $\boldsymbol{p}$ and t_s by definition of the saddle-point time t_s via the saddle-point equation (SPE) (2.44). The momentum derivative reads

$$\frac{\partial S_0}{\partial \boldsymbol{p}}\bigg|_{\boldsymbol{p},t_s} (\boldsymbol{p}' - \boldsymbol{p}) = (\boldsymbol{p}' - \boldsymbol{p}) \cdot \int_{t_s}^{t_d} \mathrm{d}t\, [\boldsymbol{p} + \boldsymbol{A}(t)] \tag{A.65}$$

$$= -\boldsymbol{v}_1(t_d) \cdot \boldsymbol{r}_0(t_d) \tag{A.66}$$

where the initial condition $\boldsymbol{r}_0(t_s) = 0$ was used. Plugging this into the action (A.63)

yields

$$S = S_0 - \int_{t_s}^{t_d} \mathrm{d}t \, \frac{Z}{\sqrt{\boldsymbol{r}_0^2}} + \boldsymbol{r}_0' \cdot \boldsymbol{v}_1 \Big|_{t_s'}^{t_d} - \boldsymbol{v}_1(t_d) \cdot \boldsymbol{r}_0(t_d) \tag{A.67}$$

$$= S_0 - \int_{t_s}^{t_d} \mathrm{d}t \, \frac{Z}{\sqrt{\boldsymbol{r}_0^2}} + \boldsymbol{r}_0'(t_d) \cdot \boldsymbol{v}_1(t_d) - \boldsymbol{r}_0'(t_s') \cdot \boldsymbol{v}_1(t_s') - \boldsymbol{v}_1(t_d) \cdot \boldsymbol{r}_0(t_d) \tag{A.68}$$

where the two boundary terms at t_d are equal and thus vanish due to equation (A.61) and $\boldsymbol{v}_1 \propto Z$. The remaining term $\boldsymbol{r}_0'(t_s') \cdot \boldsymbol{v}_1(t_s')$ is more complex to evaluate as $\boldsymbol{r}_0'(t_s') = 0$ and $\boldsymbol{v}_1(t_s')$ exhibits a divergence due to its definition as the integral over the Coulomb force,

$$\boldsymbol{v}_1(t) = -\int_{t_s'}^{t} \mathrm{d}\tau \, \frac{Z\boldsymbol{r}_0'}{\left(\boldsymbol{r}_0'^2\right)^{3/2}} \,. \tag{A.69}$$

Thus we take the limit

$$\lim_{t \to t_s'} \boldsymbol{r}_0'(t) \cdot \boldsymbol{v}_1(t) = \lim_{t \to t_s'} \boldsymbol{r}_0'(t) \cdot \left(-\int_{t_s'}^{t} \mathrm{d}\tau \, \frac{Z\boldsymbol{r}_0'(\tau)}{\left(\boldsymbol{r}_0'^2(\tau)\right)^{3/2}} \right) \tag{A.70}$$

which can be simplified using the expansion

$$\boldsymbol{r}_0'(t \to t_s') = \int_{t_s'}^{t} \mathrm{d}\tau \, [\boldsymbol{p}' + \boldsymbol{A}(\tau)] \tag{A.71}$$

$$\approx [\boldsymbol{p}' + \boldsymbol{A}(t_s')](t - t_s') \,. \tag{A.72}$$

The integral over the Coulomb force can be approximated as well due to the limit $t \to t_s'$, leading to

$$\lim_{t \to t_s'} \boldsymbol{r}_0'(t) \cdot \boldsymbol{v}_1(t) \approx \lim_{t \to t_s'} \boldsymbol{r}_0'(t) \cdot \left(-\frac{Z\boldsymbol{r}_0'(t)}{\left(\boldsymbol{r}_0'^2(t)\right)^{3/2}} (t - t_s') \right) \tag{A.73}$$

$$\approx \lim_{t \to t_s'} [\boldsymbol{p}' + \boldsymbol{A}(t_s')](t - t_s') \cdot \left(-\frac{Z[\boldsymbol{p}' + \boldsymbol{A}(t_s')](t - t_s')}{([\boldsymbol{p}' + \boldsymbol{A}(t_s')]^2 (t - t_s')^2)^{3/2}} (t - t_s') \right) \tag{A.74}$$

$$= \lim_{t \to t_s'} \left(-\frac{Z}{\sqrt{[\boldsymbol{p}' + \boldsymbol{A}(t_s')]^2}} \right) \tag{A.75}$$

$$= \pm \mathrm{i} \frac{Z}{\sqrt{2I_\mathrm{p}}} \tag{A.76}$$

where in the last step again the SPE (2.44) was used. The final expression for the

action thus reads

$$S = S_0 - \int_{t_s}^{t_d} \mathrm{d}t \, \frac{Z}{\sqrt{\boldsymbol{r}_0^2}} \pm \mathrm{i}\frac{Z}{\sqrt{2I_\mathrm{p}}} \,. \tag{A.77}$$

The last term only shifts the yield of the whole spectrum by a momentum-independent factor and thus can be dropped when doing only qualitative analysis. The only remaining term in first order is the time integral over the Coulomb potential along the uncorrected zeroth order trajectory. This is quite convenient as the latter is known analytically. How this is evaluated in practice and which numerical problems have to be considered is discussed in chapter 4. The divergence of the Coulomb term at the lower boundary which occurs when using the initial condition $\boldsymbol{r}_0(t_s) = 0$ (as already used above) can be circumvented by a matching procedure as discussed in appendix A.5.

A.5. Matching Procedure

The Coulomb integral

$$S_{\mathrm{C}} = -\int_{t_s}^{T} \mathrm{d}t\, \frac{Z}{\sqrt{\boldsymbol{r}_0^2(t)}} \tag{A.78}$$

from equation (A.77) diverges at the lower boundary due to the initial condition $\boldsymbol{r}_0(t_s) = 0$ and needs to be regularized. This can be done by matching to the asymptotic phase of the atomic wave function as described in [18], an ansatz already used in the derivation of the Coulomb-corrected PPT rate [21]. It shall be presented here in a more detailed fashion.

We start by expanding the trajectory $\boldsymbol{r}_0(t)$ around the initial time t_s,

$$\boldsymbol{r}_0(t \to t_s) = \int_{t_s}^{t} \mathrm{d}t' \left[\boldsymbol{p} + \boldsymbol{A}(t')\right] \tag{A.79}$$

$$\approx [\boldsymbol{p} + \boldsymbol{A}(t_s)](t - t_s) \tag{A.80}$$

$$r_0(t \to t_s) = \sqrt{\boldsymbol{r}_0^2(t \to t_s)} \approx \mathrm{i}\sqrt{2I_{\mathrm{p}}}(t - t_s) = \mathrm{i}\kappa(t - t_s) \tag{A.81}$$

where we used the saddle-point equation (SPE) (2.44) and defined $\kappa = \sqrt{2I_{\mathrm{p}}}$. Now we choose some matching time t_* under the condition that the electron is far from the atom, i.e., that the Coulomb force is small compared to the laser field, but the time passed since t_s is still much less than one optical cycle. This is realized by the relation

$$\frac{1}{K_0} \ll \omega\,|t_* - t_s| \ll 1 \tag{A.82}$$

from [63] with the multiquantum parameter $K_0 = I_{\mathrm{p}}/\omega$. More detailed discussions of this condition can be found in [18, 21] where the electron position is compared to the width of the tunneling barrier. We now evaluate the Coulomb integral at its lower boundary where we replace t_s by t_* and plug in the expansion for $r_0(t)$ to find

$$S_{\mathrm{C}}^{*} = -\int_{t_*} \mathrm{d}t\, \frac{Z}{r_0(t)} \tag{A.83}$$

$$\begin{aligned}
&\approx -\int_{t_*} \mathrm{d}t\, \frac{Z}{\mathrm{i}\kappa(t - t_s)} \\
&= \mathrm{i}n_* \int_{t_*} \mathrm{d}t\, \frac{1}{(t - t_s)} \\
&= -\mathrm{i}n_* \ln(t_* - t_s) \\
&= -\mathrm{i}n_* \ln\left(\frac{1}{\mathrm{i}\kappa} r(t_*)\right) \\
&= \mathrm{i}n_* \ln(\mathrm{i}\kappa^2) - \mathrm{i}n_* \ln(\kappa r(t_*))\,.
\end{aligned} \tag{A.84}$$

Here we defined an effective quantum number $n_* = Z/\sqrt{2I_\mathrm{p}}$. This result now needs to be matched with the asymptotic phase of the atomic wave function. We assume that the asymptotic behavior of the radial ground state wave function is [21]

$$\Phi_\mathrm{at}(r) \sim (\kappa r)^{n_*} \mathrm{e}^{-\kappa r} \tag{A.85}$$
$$= \mathrm{e}^{-\kappa r + n_* \ln(\kappa r)} \tag{A.86}$$
$$= \mathrm{e}^{\mathrm{i}S_\mathrm{at}} \tag{A.87}$$

from which we infer the action of the atomic wave function

$$S_\mathrm{at} = \mathrm{i}\kappa r - \mathrm{i}n_* \ln(\kappa r)\,. \tag{A.88}$$

Note that the second term matches the divergent part of the Coulomb integral at its lower boundary. Thus we can subtract this term from the full Coulomb integral to obtain a finite result,

$$S_\mathrm{C}^{(\mathrm{R})} = -\int_{t_*}^{T} \mathrm{d}t\, \frac{Z}{r_0(t)} + \mathrm{i}n_* \ln(\kappa r(t_*))\,. \tag{A.89}$$

For the numerical evaluation it is useful to rewrite this using the calculations from above,

$$\mathrm{i}n_* \ln(\kappa r(t_*)) = \mathrm{i}n_* \ln(\mathrm{i}\kappa^2) - \mathrm{i}n_* \int_{t_*} \mathrm{d}t\, \frac{1}{t - t_s} \tag{A.90}$$
$$= \mathrm{i}n_* \ln(\mathrm{i}\kappa^2) - \mathrm{i}n_* \int_{t_*}^{T} \mathrm{d}t\, \frac{1}{t - t_s} + \mathrm{i}n_* \int^{T} \mathrm{d}t\, \frac{1}{t - t_s} \tag{A.91}$$
$$= \mathrm{i}n_* \ln(\mathrm{i}\kappa^2) - \mathrm{i}n_* \int_{t_*}^{T} \mathrm{d}t\, \frac{1}{t - t_s} + \mathrm{i}n_* \ln(T - t_s) \tag{A.92}$$
$$= -\mathrm{i}n_* \int_{t_*}^{T} \mathrm{d}t\, \frac{1}{t - t_s} + \mathrm{i}n_* \ln(\mathrm{i}\kappa^2 (T - t_s)) \tag{A.93}$$

so that the regularized Coulomb integral can be written as

$$S_\mathrm{C}^{(\mathrm{R})} = \mathrm{i}n_* \ln(\mathrm{i}\kappa^2 (T - t_s)) - \int_{t_*}^{T} \mathrm{d}t\, \left[\frac{Z}{r_0(t)} + \frac{\mathrm{i}n_*}{t - t_s}\right] \tag{A.94}$$

with $r_0(t) = \sqrt{\boldsymbol{r}_0^2(t)}$. The matching time t_* needs to be chosen numerically, but since the integrand in equation (A.94) approaches 0 as $t_* \to t_s$, this choice has negligible impact on the result as long as $|t_* - t_s|$ is small. In the present implementation we use $|t_* - t_s| = 10^{-5}\frac{1}{\omega}$ which is bound to the upper limit of condition (A.82). This condition proved to be sufficient as the results did not change even under significant variations.

B. Technical Details

B.1. Applying Kepler's Laws to Find the Asymptotic Momentum

The initial conditions are that an electron trajectory $\boldsymbol{r}(t)$, $\boldsymbol{v}(t)$ has been propagated to some finite time t_d at which Kepler's laws shall be used to calculate the final velocity $\boldsymbol{v}_{\text{fin}} = \boldsymbol{v}(t \to \infty)$. This happens under the assumption that the only force influencing the electron is a conservative central force $\boldsymbol{F}(r) = -\boldsymbol{\nabla} V(\boldsymbol{r})$ with $r = \sqrt{\boldsymbol{r}^2}$ like gravity or, as in this case, the Coulomb force. For convenience we introduce the short forms $\boldsymbol{r}(t_d) = \boldsymbol{r}$ and $\boldsymbol{v}(t_d) = \boldsymbol{v}$. The laser pulse is assumed to be off/far away at time t_d, thus kinetic and canonical momentum are equal here.

First we calculate the total energy of the electron to know whether its trajectory is bound ($E_{\text{fin}} \leq 0$) or free ($E_{\text{fin}} > 0$),

$$E_{\text{fin}} = \frac{\boldsymbol{v}^2}{2} - \frac{Z}{\sqrt{\boldsymbol{r}^2}}\,. \tag{B.1}$$

Bound trajectories are not considered as they will not reach the detector and thus can not contribute to the spectrum, they are simply discarded. Free trajectories are treated using Kepler's laws.

First we define the mass equivalent

$$\mu = Z\,. \tag{B.2}$$

The electron velocity is split into a radial and a tangential part,

$$v_{\text{radial}} \equiv v_{\text{r}} = \frac{\boldsymbol{r}}{r} \cdot \boldsymbol{v} \tag{B.3}$$

$$v_{\text{tangential}} \equiv v_{\text{t}} = \sqrt{\left(\boldsymbol{v} - v_{\text{r}} \frac{\boldsymbol{r}}{r}\right)^2}\,. \tag{B.4}$$

For the Kepler formulas we need some specific quantities,

$$a = \frac{\mu}{2E_{\text{fin}}} \quad \text{(semi-major axis)} \tag{B.5}$$

$$p = \frac{r^2 v_{\text{t}}^2}{\mu} \quad \text{(semi-latus rectum)} \tag{B.6}$$

$$\varepsilon = \sqrt{1 + \frac{p}{a}} = \sqrt{1 + \frac{r^2 v_{\text{t}}^2 2E_{\text{fin}}}{\mu^2}} \quad \text{(eccentricity)}\,. \tag{B.7}$$

Another quantity is the angle of the position $\boldsymbol{r}$ in polar coordinates,

$$\gamma = \arctan2(r_y, r_z)\,, \tag{B.8}$$

the function with two parameters is used to obtain the solution in the correct quadrant. Here we assume that the motion takes place in the y-z-plane and the centers of

the Coulomb field and the coordinate system coincide. ϑ is now the running variable in a Kepler orbit, it describes the angle w.r.t. the point of closest approach and is negative when approaching and positive when leaving (the so-called true anomaly),

$$\vartheta = \pm \arccos \frac{p-r}{\varepsilon r} \,. \tag{B.9}$$

The sign of ϑ depends on the radial velocity and the angular momentum,

$$\boldsymbol{l} = \boldsymbol{r} \times \boldsymbol{v}, \quad l_x = \boldsymbol{l} \cdot \boldsymbol{e}_x \,. \tag{B.10}$$

Using this we arrive at

$$\vartheta = \operatorname{sgn}(v_\mathrm{r} l_x) \arccos \left(\frac{1}{\varepsilon} \left(\frac{p}{r} - 1 \right) \right) \tag{B.11}$$

$$= \operatorname{sgn}(v_\mathrm{r} l_x) \arccos \left(\frac{1}{\varepsilon} \left(\frac{r v_\mathrm{t}^2}{\mu} - 1 \right) \right) \tag{B.12}$$

where we defined the sign function as

$$\operatorname{sgn}(x) = \begin{cases} 1 & x > 0 \\ 0 & x = 0 \\ -1 & x < 0 \end{cases} . \tag{B.13}$$

We need the final true anomaly at infinite distance as well,

$$\vartheta_\mathrm{fin} = \operatorname{sgn}(l_x) \arccos \left(-\frac{1}{\varepsilon} \right) \,. \tag{B.14}$$

Finally we want to know the angle of the final momentum in polar coordinates which is found from geometric arguments to be

$$\theta = -\vartheta_\mathrm{fin} + \vartheta + \gamma \,. \tag{B.15}$$

The magnitude of the final momentum is known,

$$v_\mathrm{fin} = \sqrt{2E_\mathrm{fin}} \,. \tag{B.16}$$

These two quantities now define the final velocity vector in polar coordinates which are easily converted into a Cartesian vector.

Action The action associated with the propagation to infinity must be determined as well. We know that once the laser is off/far away the action integral simply condenses to

$$S_{\text{off}}(t_1, t_2) = \int_{t_1}^{t_2} \left(\frac{\boldsymbol{p}^2(t)}{2} - V(\boldsymbol{r}) \right) \mathrm{d}t \tag{B.17}$$

$$= \int_{t_1}^{t_2} E \mathrm{d}t \tag{B.18}$$

$$= E(t_2 - t_1) \tag{B.19}$$

where the ionization potential has been left out. The additional action thus reads

$$S^*_{\text{Kep}} = S_{\text{off}}(t_d, \infty) \tag{B.20}$$

$$= E_{\text{fin}}(\infty - t_d)\,. \tag{B.21}$$

The first term is infinite but only amounts to a phase factor which vanishes when calculating the probability $w_{\boldsymbol{p}} = |M(\boldsymbol{p})|^2$ from the corresponding matrix element. Accordingly the final result for the additional action according to Kepler's laws can be written as

$$S_{\text{Kep}} = -E_{\text{fin}} t_d\,. \tag{B.22}$$

B.2. Binning on the Final Momentum Grid

The evaluation of equation (3.28) is numerically much more challenging than the plain strong field approximation (SFA) in saddle-point approximation as represented by equation (2.46). This is due to the unknown (and sometimes chaotic) relation between the initial momentum $\boldsymbol{p}$ and the final momentum $\boldsymbol{p}_\infty$. To calculate a one-dimensional photoelectron momentum spectrum in a momentum range $p_{z,\infty} = [-p_{\max}, p_{\max}]$ we need to consider initial momenta from the larger range $p_z = [-d\,p_{\max}, d\,p_{\max}]$ where $d \geq 1$ accounts for possible long-range interactions with the potential $V(\boldsymbol{r}, t)$. This needs to be tuned by hand for the specific situation. Furthermore for every final momentum several different initial momenta can contribute. Thus the evaluation of (3.28) becomes a problem of statistics. To achieve good resolution in the final spectrum (both in momentum space and in the yield) we need to ensure that every final momentum is represented by many trajectories. It is not unusual to take 100 to 1000 times more trajectories than desired final momenta for the spectrum.

Every trajectory can be represented by the initial momentum $\boldsymbol{p}$, the emission time t_s, the final momentum $\boldsymbol{p}_\infty$ and the individual transition matrix element $M_{\boldsymbol{p}}(t_s)$ from (3.28). It should be noted that for one initial momentum $\boldsymbol{p}$ usually many solutions t_s of the saddle-point equation (2.44) exist, depending on the laser pulse represented by the vector potential. Here it is useful to select only the most relevant solutions as described in section 2.3 to reduce the numerical effort.

For plotting the individual trajectory contributions need to be gathered on a final momentum grid. The quality of the resulting spectrum is surprisingly sensitive on how this binning is performed.

Simple binning method There is a very simple way to do the binning. Let us for now restrict the problem to one dimension, the extension to higher dimensions is straightforward. Define a final momentum grid $p_n^{(\mathrm{bin})}$ with $n = [0, n_{\max}]$, $p_0^{(\mathrm{bin})} = -p_{\max}$ and $p_{n_{\max}}^{(\mathrm{bin})} = p_{\max}$, the grid constant is

$$\delta p^{(\mathrm{bin})} = \frac{p_{n_{\max}}^{(\mathrm{bin})} - p_0^{(\mathrm{bin})}}{n_{\max}}\,. \tag{B.23}$$

The resulting spectrum is represented by the coherent sum of all individual transition matrix elements, $M(p_n^{(\mathrm{bin})})$. For some final momentum p_∞ the bin i is selected via

$$i = \left\lfloor n_{\max} \frac{p_\infty - p_0^{(\mathrm{bin})}}{p_{n_{\max}}^{(\mathrm{bin})} - p_0^{(\mathrm{bin})}} + \frac{1}{2} \right\rfloor \tag{B.24}$$

$$= \left\lfloor \frac{p_\infty - p_0^{(\mathrm{bin})}}{\Delta p^{(\mathrm{bin})}} + \frac{1}{2} \right\rfloor \tag{B.25}$$

which just locates the closest bin momentum $p_i^{(\mathrm{bin})}$. The individual transition matrix $M_{p_\infty}(t_s)$ is added to the spectrum at the selected momentum bin,

$$M(p_i^{(\mathrm{bin})}) = M(p_i^{(\mathrm{bin})}) + M_{p_\infty}(t_s)\,. \tag{B.26}$$

This is repeated for all trajectories.

Smooth binning method The method described above neglects the difference between p_∞ and $p_i^{(\mathrm{bin})}$. This can be improved by splitting the contribution $M_{p_\infty}(t_s)$ between the two neighboring momentum bins. The momentum grid is the same as above. The nearest neighbors i and $i+1$ are then found from

$$i = \left\lfloor \frac{p_\infty - p_0^{(\mathrm{bin})}}{\Delta p^{(\mathrm{bin})}} \right\rfloor \tag{B.27}$$

without the shift by $\frac{1}{2}$. The splitting factor f_i is calculated as

$$f_i = 1 - \frac{p_\infty - p_i^{(\mathrm{bin})}}{\Delta p^{(\mathrm{bin})}} \tag{B.28}$$

which denotes the fraction of the contribution to grid point i. The contribution to $i+1$ is $f_{i+1} = 1 - f_i$. The individual transition matrix $M_{p_\infty}(t_s)$ is then split up between i and $i+1$ as

$$M(p_i^{(\mathrm{bin})}) = M(p_i^{(\mathrm{bin})}) + \sqrt{f_i} M_{p_\infty}(t_s) \tag{B.29a}$$

$$M(p_{i+1}^{(\mathrm{bin})}) = M(p_{i+1}^{(\mathrm{bin})}) + \sqrt{1-f_i} M_{p_\infty}(t_s)\,. \tag{B.29b}$$

From our experience this method significantly increases the contrast in the spectra and thus reduces the number of trajectories that have to be calculated, i.e., the numerical effort. However, this becomes relevant only when calculating spectra in two dimensions as there the number of trajectories to be calculated reaches 10^7 or even 10^8 when considering large momentum ranges.

Final Spectrum The final result is a momentum-resolved photoelectron spectrum, i.e. the probability $w_{\boldsymbol{p}_n^{(\mathrm{bin})}} \equiv w_{\boldsymbol{p}}$ to find an electron within the momentum bin represented by $\boldsymbol{p}_n^{(\mathrm{bin})} \equiv \boldsymbol{p}$. This is described by the transition matrix element $M(\boldsymbol{p}_n^{(\mathrm{bin})}) \equiv M(\boldsymbol{p})$ calculated above via

$$w_{\boldsymbol{p}}\,\mathrm{d}^3p = |M(\boldsymbol{p})|^2\,\mathrm{d}^3p \tag{B.30}$$

so that $w_{\boldsymbol{p}} = |M(\boldsymbol{p})|^2$. However, this depends on the coordinates used. When considering a two-dimensional cut through a three-dimensional Cartesian coordinate system the probability stays the same as above. When calculating spectra for

linearly polarized laser fields it is often useful to convert to cylindrical coordinates ($p_\parallel$ parallel to the polarization direction and $p_\perp$ in perpendicular direction) where due to cylindrical symmetry one can integrate over the angle φ. In that case the probability is different,

$$\begin{aligned} w(p_\parallel, p_\perp)\,\mathrm{d}p_\parallel\,\mathrm{d}p_\perp &= |M(\boldsymbol{p})|^2\ \mathrm{d}^3p = |M(\boldsymbol{p})|^2\ p_\perp \mathrm{d}p_\perp\,\mathrm{d}p_\parallel\,\mathrm{d}\varphi \\ &= |M(\boldsymbol{p})|^2\ 2\pi\, p_\perp \mathrm{d}p_\parallel\,\mathrm{d}p_\perp\,, \end{aligned} \tag{B.31}$$

so that $w(p_\parallel, p_\perp) = 2\pi\, p_\perp\, |M(\boldsymbol{p})|^2$. Another important case is the energy-resolved photoelectron spectrum in spherical coordinates where $w(\mathcal{E}_{\boldsymbol{p}}, \Omega_{\boldsymbol{p}})$ is the probability to find an electron with energy $\mathcal{E}_{\boldsymbol{p}} = \frac{1}{2}\boldsymbol{p}^2$ at a certain emission direction which corresponds to the solid angle element $\mathrm{d}\Omega_{\boldsymbol{p}}$. Here the relation is as follows ([17], or [32], section 7.3.5):

$$w(\mathcal{E}_{\boldsymbol{p}}, \Omega_{\boldsymbol{p}})\,\mathrm{d}\mathcal{E}_{\boldsymbol{p}}\,\mathrm{d}\Omega_{\boldsymbol{p}} = |M(\boldsymbol{p})|^2\ \mathrm{d}p^3 = |M(\boldsymbol{p})|^2\ p^2 \mathrm{d}p\,\mathrm{d}\Omega_{\boldsymbol{p}} = |M(\boldsymbol{p})|^2\ p \underbrace{\mathrm{d}\mathcal{E}_{\boldsymbol{p}}}_{=p\mathrm{d}p}\ \mathrm{d}\Omega_{\boldsymbol{p}}\,, \tag{B.32}$$

leading to $w(\mathcal{E}_{\boldsymbol{p}}, \Omega_{\boldsymbol{p}}) = p\,|M(\boldsymbol{p})|^2$.

Bibliography

[1] C. I. Blaga, F. Catoire, P. Colosimo, G. G. Paulus, H. G. Muller, P. Agostini, and L. F. DiMauro, "Strong-field photoionization revisited", Nat. Phys. **5**, 335–338 (2009) 10.1038/nphys1228 (cit. on pp. 1, 35, 59).

[2] F. H. M. Faisal, "Strong-field physics: ionization surprise", Nat. Phys. **5**, 319–320 (2009) 10.1038/nphys1264 (cit. on pp. 1, 35).

[3] A. Kästner, U. Saalmann, and J. M. Rost, "Electron-energy bunching in laser-driven soft recollisions", Phys. Rev. Lett. **108**, 033201 (2012) 10.1103/PhysRevLett.108.033201 (cit. on pp. 1, 35).

[4] W. Quan, Z. Lin, M. Wu, H. Kang, H. Liu, X. Liu, J. Chen, J. Liu, X. T. He, S. G. Chen, H. Xiong, L. Guo, H. Xu, Y. Fu, Y. Cheng, and Z. Z. Xu, "Classical aspects in above-threshold ionization with a midinfrared strong laser field", Phys. Rev. Lett. **103**, 093001 (2009) 10.1103/PhysRevLett.103.093001 (cit. on pp. 1, 35, 59).

[5] C. Y. Wu, Y. D. Yang, Y. Q. Liu, Q. H. Gong, M. Wu, X. Liu, X. L. Hao, W. D. Li, X. T. He, and J. Chen, "Characteristic spectrum of very low-energy photoelectron from above-threshold ionization in the tunneling regime", Phys. Rev. Lett. **109**, 043001 (2012) 10.1103/PhysRevLett.109.043001 (cit. on pp. 1, 35).

[6] J. Dura, N. Camus, A. Thai, A. Britz, M. Hemmer, M. Baudisch, A. Senftleben, C. D. Schröter, J. Ullrich, R. Moshammer, and J. Biegert, "Ionization with low-frequency fields in the tunneling regime", Sci. Rep. **3**, Article (2013) 10.1038/srep02675 (cit. on pp. 1, 35).

[7] B. Wolter, M. G. Pullen, M. Baudisch, M. Sclafani, M. Hemmer, A. Senftleben, C. D. Schröter, J. Ullrich, R. Moshammer, and J. Biegert, "Strong-field physics with mid-IR fields", Phys. Rev. X **5**, 021034 (2015) 10.1103/PhysRevX.5.021034 (cit. on pp. 1, 35).

[8] C. T. L. Smeenk, L. Arissian, B. Zhou, A. Mysyrowicz, D. M. Villeneuve, A. Staudte, and P. B. Corkum, "Partitioning of the linear photon momentum in multiphoton ionization", Phys. Rev. Lett. **106**, 193002 (2011) 10.1103/PhysRevLett.106.193002 (cit. on pp. 1, 53, 69).

[9] A. Ludwig, J. Maurer, B. W. Mayer, C. R. Phillips, L. Gallmann, and U. Keller, "Breakdown of the dipole approximation in strong-field ionization", Phys. Rev. Lett. **113**, 243001 (2014) 10.1103/PhysRevLett.113.243001 (cit. on pp. 1, 53, 58–60, 69).

[10] H. R. Reiss, "Absorption of light by light", Journal of Mathematical Physics **3**, 59–67 (1962) 10.1063/1.1703787 (cit. on p. 1).

[11] L. Keldysh, Zh. Eksp. Teor. Fiz. **47**, 1945 (1964); "Ionization in the field of a strong electromagnetic wave", Sov. Phys. JETP **20**, 1307 (1965), cit. on pp. 1, 35, 38.

[12] F. H. M. Faisal, "Multiple absorption of laser photons by atoms", J. Phys. B: At. Mol. Phys. **6**, L89 (1973) 10.1088/0022-3700/6/4/011 (cit. on pp. 1, 35).

[13] H. R. Reiss, "Effect of an intense electromagnetic field on a weakly bound system", Phys. Rev. A **22**, 1786–1813 (1980) 10.1103/PhysRevA.22.1786 (cit. on pp. 1, 8, 35, 38).

[14] A. Lohr, M. Kleber, R. Kopold, and W. Becker, "Above-threshold ionization in the tunneling regime", Phys. Rev. A **55**, R4003–R4006 (1997) 10.1103/PhysRevA.55.R4003 (cit. on pp. 1, 7, 10).

[15] D. B. Milošević and F. Ehlotzky, "Coulomb and rescattering effects in above-threshold ionization", Phys. Rev. A **58**, 3124–3127 (1998) 10.1103/PhysRevA.58.3124 (cit. on p. 1).

[16] V. S. Popov, "Tunnel and multiphoton ionization of atoms and ions in a strong laser field (Keldysh theory)", Phys. Usp. **47**, 855 (2004) 10.1070/PU2004v047n09ABEH001812 (cit. on pp. 1, 15, 36).

[17] D. B. Milošević, G. G. Paulus, D. Bauer, and W. Becker, "Above-threshold ionization by few-cycle pulses", J. Phys. B: At., Mol. Opt. Phys. **39**, R203 (2006) 10.1088/0953-4075/39/14/R01 (cit. on pp. 1, 9, 12, 13, 19, 35, 79, 80, 95).

[18] S. V. Popruzhenko, "Keldysh theory of strong field ionization: history, applications, difficulties and perspectives", J. Phys. B: At., Mol. Opt. Phys. **47**, 204001 (2014) 10.1088/0953-4075/47/20/204001 (cit. on pp. 1, 2, 24, 35, 42, 47, 81, 87).

[19] A. Perelomov, V. Popov, and M. Terent'ev, Zh. Eksp. Teor. Fiz. **50**, 1393 (1966); "Ionization of atoms in an alternating electrical field.", Sov. Phys. JETP **23**, 924 (1966), cit. on pp. 2, 41.

[20] A. Perelomov, V. Popov, and M. Terent'ev, Zh. Eksp. Teor. Fiz. **51**, 309 (1967); "Ionization of atoms in an alternating electrical field. II", Sov. Phys. JETP **24**, 207 (1967), cit. on pp. 2, 41.

[21] A. Perelomov and V. Popov, Zh. Eksp. Teor. Fiz. **52**, 514 (1966); "Ionization of atoms in an alternating electrical field. III", Sov. Phys. JETP **25**, 336 (1967), cit. on pp. 2, 41, 42, 48, 81, 87, 88.

[22] S. Popruzhenko and D. Bauer, "Strong field approximation for systems with Coulomb interaction", J. Mod. Opt. **55**, 2573–2589 (2008) 10.1080/09500340802161881 (cit. on pp. 2, 24, 36).

[23] S. V. Popruzhenko, V. D. Mur, V. S. Popov, and D. Bauer, "Strong field ionization rate for arbitrary laser frequencies", Phys. Rev. Lett. **101**, 193003 (2008) 10.1103/PhysRevLett.101.193003 (cit. on pp. 2, 24, 36).

[24] T.-M. Yan, S. V. Popruzhenko, M. J. J. Vrakking, and D. Bauer, "Low-energy structures in strong field ionization revealed by quantum orbits", Phys. Rev. Lett. **105**, 253002 (2010) 10.1103/PhysRevLett.105.253002 (cit. on pp. 2, 24, 25, 33, 34, 36, 51, 61).

[25] T.-M. Yan, S. Popruzhenko, and D. Bauer, "Trajectory-based Coulomb-corrected strong field approximation", English, in *Progress in ultrafast intense laser science*, Vol. 104, edited by K. Yamanouchi and K. Midorikawa, Springer Series in Chemical Physics (Springer Berlin Heidelberg, 2013), pp. 1–16, 10.1007/978-3-642-35052-8_1 (cit. on pp. 2, 24, 25, 34, 36).

[26] T.-M. Yan, "Trajectory-based Coulomb-corrected strong field approximation", PhD thesis (Universität Rostock, Jan. 2013) (cit. on p. 2).

[27] L. Torlina and O. Smirnova, "Time-dependent analytical R-matrix approach for strong-field dynamics. I. one-electron systems", Phys. Rev. A **86**, 043408 (2012) 10.1103/PhysRevA.86.043408 (cit. on p. 2).

[28] L. Torlina, M. Ivanov, Z. B. Walters, and O. Smirnova, "Time-dependent analytical R-matrix approach for strong-field dynamics. II. many-electron systems", Phys. Rev. A **86**, 043409 (2012) 10.1103/PhysRevA.86.043409 (cit. on p. 2).

[29] E. Pisanty and M. Ivanov, "Slalom in complex time: emergence of low-energy structures in tunnel ionization via complex-time contours", Phys. Rev. A **93**, 043408 (2016) 10.1103/PhysRevA.93.043408, arXiv:1507.00011 [quant-ph] (cit. on pp. 2, 44–46, 48).

[30] E. Pisanty Alatorre, "Electron dynamics in complex time and complex space", PhD thesis (Imperial College London, Sept. 2016) (cit. on pp. 2, 44, 48).

[31] O. Smirnova, M. Spanner, and M. Ivanov, "Analytical solutions for strong field-driven atomic and molecular one- and two-electron continua and applications to strong-field problems", Phys. Rev. A **77**, 033407 (2008) 10.1103/PhysRevA.77.033407 (cit. on p. 2).

[32] P. Mulser and D. Bauer, *High power laser-matter interaction*, Vol. 238, Springer Tracts in Modern Physics (Springer-Verlag Berlin Heidelberg, 2010), 10.1007/978-3-540-46065-7 (cit. on pp. 5, 7, 9, 10, 17, 19, 95).

[33] W. Gordon, "Der Comptoneffekt nach der Schrödingerschen Theorie", Z. Phys. **40**, 117–133 (1926) 10.1007/BF01390840 (cit. on p. 6).

[34] D. M. Wolkow, "Über eine Klasse von Lösungen der Diracschen Gleichung", Z. Phys. **94**, 250–260 (1935) 10.1007/BF01331022 (cit. on p. 6).

[35] D. Bauer, D. B. Milošević, and W. Becker, "Strong-field approximation for intense-laser–atom processes: the choice of gauge", Phys. Rev. A **72**, 023415 (2005) 10.1103/PhysRevA.72.023415 (cit. on p. 7).

[36] D. G. Arbó, K. L. Ishikawa, K. Schiessl, E. Persson, and J. Burgdörfer, "Intracycle and intercycle interferences in above-threshold ionization: the time grating", Phys. Rev. A **81**, 021403 (2010) 10.1103/PhysRevA.81.021403 (cit. on pp. 11, 17).

[37] P. B. Corkum, N. H. Burnett, and F. Brunel, "Above-threshold ionization in the long-wavelength limit", Phys. Rev. Lett. **62**, 1259–1262 (1989) 10.1103/PhysRevLett.62.1259 (cit. on p. 15).

[38] T. Fennel, T. Döppner, J. Passig, C. Schaal, J. Tiggesbäumker, and K.-H. Meiwes-Broer, "Plasmon-enhanced electron acceleration in intense laser metal-cluster interactions", Phys. Rev. Lett. **98**, 143401 (2007) 10.1103/PhysRevLett.98.143401 (cit. on pp. 19, 29).

[39] T. Keil and D. Bauer, "Collective-field-corrected strong field approximation for laser-irradiated metal clusters", J. Phys. B: At., Mol. Opt. Phys. **47**, 124029 (2014) 10.1088/0953-4075/47/12/124029 (cit. on pp. 19, 36, 74).

[40] P. B. Parks, T. E. Cowan, R. B. Stephens, and E. M. Campbell, "Model of neutron-production rates from femtosecond-laser-cluster interactions", Phys. Rev. A **63**, 063203 (2001) 10.1103/PhysRevA.63.063203 (cit. on p. 20).

[41] S. V. Fomichev, S. V. Popruzhenko, D. F. Zaretsky, and W. Becker, "Laser-induced nonlinear excitation of collective electron motion in a cluster", J. Phys. B: At., Mol. Opt. Phys. **36**, 3817 (2003) 10.1088/0953-4075/36/18/310 (cit. on p. 20).

[42] S. V. Fomichev, D. F. Zaretsky, and W. Becker, "Classical modelling of the nonlinear properties of clusters in strong low-frequency laser fields", J. Phys. B: At., Mol. Opt. Phys. **37**, L175 (2004) 10.1088/0953-4075/37/8/105 (cit. on p. 20).

[43] P. Mulser and M. Kanapathipillai, "Collisionless absorption in clusters out of linear resonance", Phys. Rev. A **71**, 063201 (2005) 10.1103/PhysRevA.71.063201 (cit. on p. 20).

[44] G. Y. Panasyuk, J. C. Schotland, and V. A. Markel, "Classical theory of optical nonlinearity in conducting nanoparticles", Phys. Rev. Lett. **100**, 047402 (2008) 10.1103/PhysRevLett.100.047402 (cit. on p. 20).

[45] W. Kohn, "Nobel lecture: electronic structure of matter-wave functions and density functionals", Rev. Mod. Phys. **71**, 1253–1266 (1999) 10.1103/RevModPhys.71.1253 (cit. on p. 22).

[46] E. Runge and E. K. U. Gross, "Density-functional theory for time-dependent systems", Phys. Rev. Lett. **52**, 997–1000 (1984) 10.1103/PhysRevLett.52.997 (cit. on p. 22).

[47] D. Bauer and P. Koval, "Qprop: a Schrödinger-solver for intense laser-atom interaction", Comput. Phys. Commun. **174**, 396–421 (2006) 10.1016/j.cpc.2005.11.001 (cit. on pp. 22, 36, 38).

[48] D. Bauer, ed., *Computational strong-field quantum dynamics - intense light-matter interactions*, De Gruyter Textbook (De Gruyter, Berlin, Boston, 2017) (cit. on pp. 22, 36, 38).

[49] F. Reimann, "Study of the existence and decay of multiply charged cluster anions using time-dependent density functional theory", M.Sc. thesis (Universität Rostock, 2013) (cit. on p. 22).

[50] T.-M. Yan and D. Bauer, "Sub-barrier Coulomb effects on the interference pattern in tunneling-ionization photoelectron spectra", Phys. Rev. A **86**, 053403 (2012) 10.1103/PhysRevA.86.053403 (cit. on p. 25).

[51] J. R. Dormand and P. J. Prince, "A family of embedded Runge-Kutta formulae", J. Comput. Appl. Math. **6**, 19–26 (1980) 10.1016/0771-050X(80)90013-3 (cit. on p. 28).

[52] H. Bach, *ACM TOMS 365 - complex root finding*, http://people.sc.fsu.edu/~jburkardt/f77_src/toms365/toms365.html, [Online; accessed 03-May-2017] (cit. on p. 28).

[53] M. M. Kappes, M. Schär, U. Röthlisberger, C. Yeretzian, and E. Schumacher, "Sodium cluster ionisation potentials revisited: higher-resolution measurements for Na_x ($x < 23$) and their relation to bonding models", Chem. Phys. Lett. **143**, 251–258 (1988) 10.1016/0009-2614(88)87376-7 (cit. on p. 29).

[54] Y. Huismans, A. Rouzée, A. Gijsbertsen, J. H. Jungmann, A. S. Smolkowska, P. S. W. M. Logman, F. Lépine, C. Cauchy, S. Zamith, T. Marchenko, J. M. Bakker, G. Berden, B. Redlich, A. F. G. van der Meer, H. G. Muller, W. Vermin, K. J. Schafer, M. Spanner, M. Y. Ivanov, O. Smirnova, D. Bauer, S. V. Popruzhenko, and M. J. J. Vrakking, "Time-resolved holography with photoelectrons", Science **331**, 61–64 (2011) 10.1126/science.1198450 (cit. on pp. 34–36).

[55] C. I. Blaga, J. Xu, A. D. DiChiara, E. Sistrunk, K. Zhang, P. Agostini, T. A. Miller, L. F. DiMauro, and C. D. Lin, "Imaging ultrafast molecular dynamics with laser-induced electron diffraction", Nature **483**, 194–197 (2012) 10.1038/nature10820 (cit. on pp. 34, 72).

[56] R. Kopold, W. Becker, and M. Kleber, "Quantum path analysis of high-order above-threshold ionization", Opt. Commun. **179**, 39–50 (2000) 10.1016/S0030-4018(99)00521-0 (cit. on p. 35).

[57] P. Salières, B. Carré, L. Le Déroff, F. Grasbon, G. G. Paulus, H. Walther, R. Kopold, W. Becker, D. B. Milošević, A. Sanpera, and M. Lewenstein, "Feynman's path-integral approach for intense-laser-atom interactions", Science **292**, 902–905 (2001) 10.1126/science.108836 (cit. on p. 35).

[58] C. Liu and K. Z. Hatsagortsyan, "Origin of unexpected low energy structure in photoelectron spectra induced by midinfrared strong laser fields", Phys. Rev. Lett. **105**, 113003 (2010) 10.1103/PhysRevLett.105.113003 (cit. on p. 35).

[59] M. Möller, F. Meyer, A. M. Sayler, G. G. Paulus, M. F. Kling, B. E. Schmidt, W. Becker, and D. B. Milošević, "Off-axis low-energy structures in above-threshold ionization", Phys. Rev. A **90**, 023412 (2014) 10.1103/PhysRevA.90.023412 (cit. on p. 35).

[60] D. B. Milošević, "Low-frequency approximation for above-threshold ionization by a laser pulse: low-energy forward rescattering", Phys. Rev. A **90**, 063423 (2014) 10.1103/PhysRevA.90.063423 (cit. on p. 35).

[61] V. Mosert and D. Bauer, "Photoelectron spectra with Qprop and t-SURFF", Comput. Phys. Commun. **207**, 452–463 (2016) 10.1016/j.cpc.2016.06.015 (cit. on pp. 36, 38).

[62] T. Keil, S. V. Popruzhenko, and D. Bauer, "Laser-driven recollisions under the Coulomb barrier", Phys. Rev. Lett. **117**, 243003 (2016) 10.1103/PhysRevLett.117.243003 (cit. on p. 37).

[63] S. Popruzhenko, "Invariant form of Coulomb corrections in the theory of nonlinear ionization of atoms by intense laser radiation", English, J. Exp. Theor. Phys. **118**, 580–586 (2014) 10.1134/S1063776114040062 (cit. on pp. 41, 44–46, 87).

[64] J. Liu, Q. Z. Xia, J. F. Tao, and L. B. Fu, "Coulomb effects in photon-momentum partitioning during atomic ionization by intense linearly polarized light", Phys. Rev. A **87**, 041403 (2013) 10.1103/PhysRevA.87.041403 (cit. on p. 53).

[65] A. S. Titi and G. W. F. Drake, "Quantum theory of longitudinal momentum transfer in above-threshold ionization", Phys. Rev. A **85**, 041404 (2012) 10.1103/PhysRevA.85.041404 (cit. on p. 53).

[66] H. R. Reiss, "Relativistic effects in nonrelativistic ionization", Phys. Rev. A **87**, 033421 (2013) 10.1103/PhysRevA.87.033421 (cit. on p. 53).

[67] P.-L. He, D. Lao, and F. He, "Strong field theories beyond dipole approximations in nonrelativistic regimes", Phys. Rev. Lett. **118**, 163203 (2017) 10.1103/PhysRevLett.118.163203 (cit. on p. 53).

[68] S. Chelkowski, A. D. Bandrauk, and P. B. Corkum, "Photon-momentum transfer in multiphoton ionization and in time-resolved holography with photoelectrons", Phys. Rev. A **92**, 051401 (2015) 10.1103/PhysRevA.92.051401 (cit. on pp. 53, 60).

[69] I. A. Ivanov, "Relativistic calculation of the electron-momentum shift in tunneling ionization", Phys. Rev. A **91**, 043410 (2015) 10.1103/PhysRevA.91.043410 (cit. on p. 53).

[70] T. Keil and D. Bauer, "Coulomb-corrected strong-field quantum trajectories beyond dipole approximation", J. Phys. B: At., Mol. Opt. Phys. (2017) 10.1088/1361-6455/aa8ab1 (cit. on p. 54).

[71] M. Klaiber, E. Yakaboylu, H. Bauke, K. Z. Hatsagortsyan, and C. H. Keitel, "Under-the-barrier dynamics in laser-induced relativistic tunneling", Phys. Rev. Lett. **110**, 153004 (2013) 10.1103/PhysRevLett.110.153004 (cit. on p. 56).

[72] K. Zhang, Y. H. Lai, E. Diesen, B. E. Schmidt, C. I. Blaga, J. Xu, T. T. Gorman, F. Légaré, U. Saalmann, P. Agostini, J. M. Rost, and L. F. DiMauro, "Universal pulse dependence of the low-energy structure in strong-field ionization", Phys. Rev. A **93**, 021403 (2016) 10.1103/PhysRevA.93.021403 (cit. on pp. 59, 61).

[73] S. Skruszewicz, J. Tiggesbäumker, K.-H. Meiwes-Broer, M. Arbeiter, T. Fennel, and D. Bauer, "Two-color strong-field photoelectron spectroscopy and the phase of the phase", Phys. Rev. Lett. **115**, 043001 (2015) 10.1103/PhysRevLett.115.043001 (cit. on p. 72).

[74] N. Bleistein and R. A. Handelsman, *Asymptotic expansions of integrals* (Dover Publications, New York, 1986) (cit. on p. 79).